

---

# Gravitational-wave astronomy with compact binary coalescences: from blip glitches to the black hole area increase law

---

Von der Fakultät für Mathematik und Physik  
der Gottfried Wilhelm Leibniz Universität Hannover  
zur Erlangung des akademischen Grades

Doktorin der Naturwissenschaften  
– Dr. rer. nat. –

genehmigte Dissertation von

**M. Sc. Miriam A. Cabero Müller**

geboren am 4. März 1988 in Santa Margalida, Spanien

2018

*Referent:*

Prof. Dr. Bernd Brügmann  
Friedrich-Schiller-Universität Jena

*Korreferenten:*

Prof. Dr. Duncan Brown  
Syracuse University

Assoc. Prof. Dr. Joshua R. Smith  
California State University, Fullerton

*Tag der Promotion:*

28. Februar 2018

# Abstract

The beginning of gravitational-wave astronomy dates from the 14th of September 2015, when the Laser Interferometer Gravitational-wave Observatories (LIGO) measured a gravitational wave for the first time. This signal originated from a pair of merging black holes, providing direct confirmation of the existence of binary systems formed by two black holes. To date, a total of five confirmed and one candidate gravitational-wave signals from binary black holes have been announced. Furthermore, a gravitational-wave signal from a neutron star binary has been observed jointly with electromagnetic radiation. These observations entail a breakthrough in the astronomy of compact binaries and provide insight into highly relativistic systems.

In this work we cover several areas from the gravitational-wave astronomy of compact binary coalescences. We begin by introducing data analysis techniques used during the second generation of ground-based gravitational-wave observatories. Using real results from astrophysical signals, we explain the procedures to estimate the statistical significance of gravitational-wave signals. We observe a specific type of short noise transients in the data, commonly known as blip glitches, that is particularly harmful for transient gravitational-wave searches. Here we introduce a method to identify occurrences of blip glitches. With the results obtained, we investigate the origin of these noise transients and present here the current state of these investigations.

Astrophysical gravitational-wave signals allow for tests of general relativity that would otherwise not be possible. For instance, the ringdown phase of a compact binary coalescence is characteristic of the nature of a Kerr black hole. With Bayesian inference and using only this ringdown signature, we develop a method to estimate the parameters of the remnant black hole after a binary coalescence. This method lays the foundations to perform tests of the no-hair theorem and of the black hole area increase law. In this work we focus on the latter, for which we also need to use the inspiral signature of the coalescence. We devise a well-defined condition for the end of the inspiral stage by combining information from post-Newtonian theory with the exact Kerr test-mass limit. Our result is called the hybrid MECO (Minimum Energy Circular Orbit). We develop a method to test the area increase law in which this hybrid MECO is used to separate the inspiral part of the signal and measure the initial parameters of the binary. Comparing the inspiral measurements with the ringdown parameters on a simulated signal, we find that the area theorem could be confirmed to  $\sim 74.6\%$  confidence with current sensitivity. This result can improve to  $\sim 99.9\%$  confidence using future design sensitivities.

**Key words:** PyCBC, blip glitches, ringdown, hybrid MECO, area theorem.



# Kurzzusammenfassung

Der Beginn der Gravitationswellenastronomie geht auf den 14. September 2015 zurück, als die Laser Interferometer Gravitationswellen Observatorien (LIGO) erstmals eine Gravitationswelle aufzeichneten. Das Signal stammte von einem Paar verschmelzender Schwarzer Löcher und lieferte eine direkte Bestätigung der Existenz von binären Systemen, die durch zwei Schwarze Löcher gebildet werden. Bis heute wurden insgesamt fünf Gravitationswellensignale von binären Schwarzen Löchern bestätigt und ein Kandidat identifiziert. Weiterhin wurde ein Gravitationswellensignal von einem binären Neutronenstern zusammen mit elektromagnetischer Strahlung beobachtet. Diese Beobachtungen führten zu einem Durchbruch in der Astronomie von kompakten Binärsystemen und geben Einblick in hochrelativistische Systeme.

In der hier vorliegenden Arbeit beschäftigen wir uns mit einigen Gebieten der Gravitationswellenastronomie verschmelzender, kompakter Binärsystemen. Wir beginnen mit der Einführung von Techniken der Datenanalyse, die während der zweiten Generation von erdbasierten Gravitationswellendetektoren verwendet wurden. Anhand von realen Ergebnissen aus astrophysikalischen Signalen erklären wir die Verfahren zur Schätzung der statistischen Signifikanz von Gravitationswellensignalen. Wir beobachten eine besondere Art von kurzen Rauschsignalen in den Daten, die allgemein als “blip glitches” bekannt sind und besonders schädlich für transiente Gravitationswellen-Suchvorgänge sind. Hier stellen wir eine Methode vor, um das Auftreten von blip glitches zu identifizieren. Anhand der erhaltenen Ergebnisse untersuchen wir die Entstehung dieser Störungstransienten und präsentieren hier den aktuellen Stand dieser Untersuchungen.

Astrophysikalische Gravitationswellensignale ermöglichen Tests der Allgemeinen Relativitätstheorie, die sonst nicht möglich wären. Zum Beispiel ist die “Ringdown” Phase einer kompakten Binärverschmelzung charakteristisch für die Natur eines Kerr Schwarzen Lochs. Mit der Bayes’schen Inferenz und dieser Ringdown Signatur entwickeln wir eine Methode, um die Parameter des verbleibenden Schwarzen Lochs nach einer binären Verschmelzung abzuschätzen. Diese Methode legt die Grundlagen für die Durchführung von Tests des Keine-Haare-Theorems und des Flächenvergrößerungsgesetzes Schwarzer Löcher. In dieser Arbeit konzentrieren wir uns auf Letzteres, wofür wir auch die einspiralende Signatur der Verschmelzung verwenden müssen. Wir entwickeln eine wohldefinierte Bedingung für das Ende der Einspiralphase, indem wir Informationen aus der Post-Newtonschen Theorie mit der exakten Kerr Lösung kombinieren. Unser Ergebnis heißt Hybrid MECO (Minimum Energy Circular Orbit). Wir entwickeln eine Methode, um das Flächenvergrößerungsgesetz zu testen, bei dem dieser Hybrid MECO verwendet wird, um den einspiralenenden Teil des Signals zu trennen und die Anfangsparameter des Binärsignals zu messen. Vergleicht man die Messungen der Einspiralphase mit den Ringdown Parametern eines simulierten Signals, so kann man den Flächensatz mit  $\sim 74.6\%$  Sicherheit bei der aktuellen Empfindlichkeit bestätigen. Dieses Ergebnis kann unter Verwendung zukünftiger Messempfindlichkeiten auf  $\sim 99.9\%$  Sicherheit verbessert werden.



# Contents

<b>1</b>	<b>Introduction</b>	<b>1</b>
1.1	Gravitational waves . . . . .	3
1.2	Compact binary coalescences . . . . .	5
1.2.1	Inspiral . . . . .	6
1.2.2	Merger and ringdown . . . . .	7
1.3	Interferometric gravitational-wave detectors . . . . .	8
1.4	Astrophysical gravitational-wave signals . . . . .	11
1.5	Outline . . . . .	12
<b>2</b>	<b>Searches for gravitational waves with PyCBC</b>	<b>13</b>
2.1	Single detector data analysis . . . . .	14
2.2	Coincidence between detectors . . . . .	17
2.3	Offline searches . . . . .	20
2.4	Closed box results . . . . .	21
2.4.1	Summary page . . . . .	21
2.4.2	Single triggers . . . . .	24
2.4.3	Injections . . . . .	27
2.5	Open box results . . . . .	28
2.5.1	LVT151012 . . . . .	29
2.5.2	GW170814 and GW170817 . . . . .	30
2.6	Conclusions . . . . .	31
<b>3</b>	<b>Identifying short noise transients in Advanced LIGO data</b>	<b>33</b>
3.1	Description of a blip glitch . . . . .	35
3.2	Finding blip glitches . . . . .	36
3.3	Effect of blip glitches on PyCBC searches . . . . .	38
3.4	Investigating the origin of blip glitches . . . . .	40
3.4.1	Correlation with humidity . . . . .	40
3.4.2	Laser blips . . . . .	41
3.4.3	Computer error blips . . . . .	42
3.5	Conclusions . . . . .	44

<b>4 Parameter estimation of the black-hole ringdown</b>	<b>47</b>
4.1 Bayesian inference . . . . .	48
4.2 Ringdown model . . . . .	49
4.3 Single-mode parameter estimation on GW150914 . . . . .	50
4.4 Multi-mode parameter estimation on simulated signals . . . . .	53
4.5 Conclusions . . . . .	55
<b>5 The end of the inspiral in the post-Newtonian approximation</b>	<b>57</b>
5.1 Behaviour of the MECO at different post-Newtonian orders . . . . .	60
5.2 PN expansions of the test-mass limit . . . . .	62
5.3 Stabilisation of the MECO . . . . .	63
5.4 Relative SNR between inspiral templates . . . . .	66
5.5 Application to post-Newtonian approximants . . . . .	69
5.6 Including additional physical effects to the hybrid energy . . . . .	70
5.7 Conclusions . . . . .	72
<b>6 Observational tests of the area increase law with gravitational waves</b>	<b>73</b>
6.1 Preliminaries . . . . .	75
6.1.1 Testing the assumptions . . . . .	75
6.1.2 Estimating the parameters . . . . .	77
6.2 Method . . . . .	78
6.2.1 The effect of sky location . . . . .	79
6.2.2 The inspiral analysis . . . . .	80
6.2.3 The ringdown analysis . . . . .	83
6.3 Combined results . . . . .	84
6.4 Simulating violations of the area theorem . . . . .	88
6.5 Conclusions . . . . .	89
<b>7 Conclusions</b>	<b>91</b>
<b>Appendix A Detector Characterisation tools</b>	<b>1</b>
<b>Appendix B Relations between parameters</b>	<b>3</b>
<b>Appendix C Post-Newtonian approximation</b>	<b>5</b>
<b>Bibliography</b>	
<b>Acknowledgements</b>	

## List of Figures

1.1	Effect of the gravitational wave's polarisations on a ring of test particles.	4
1.2	Principal noise terms for the design sensitivity of Advanced LIGO detectors.	10
2.1	Organisation of the results pages from the PyCBC offline analysis.	21
2.2	Amplitude spectral density and range for one of the O1 searches.	22
2.3	Histograms of the re-weighted SNR of background events for one of the O1 searches.	22
2.4	Missed and found injections for one of the O1 searches.	23
2.5	Sensitivity of the PyCBC analysis for one of the O1 searches.	23
2.6	Single detector triggers of the PyCBC analysis for one of the O1 searches.	24
2.7	Follow up of single detector triggers for one of the O1 searches.	25
2.8	Time-frequency representation of the loudest single detector trigger in the PyCBC analysis for one of the O1 searches.	26
2.9	PyCBC open box results for the analysis containing LVT151012.	29
2.10	PyCBC open box results for the analysis containing the GW170814 and GW170817 signals.	30
3.1	Optical configuration of the Advanced LIGO detectors.	34
3.2	Time-frequency representation of a blip glitch.	35
3.3	Similitude between blip glitches and CBC waveforms.	36
3.4	Blip glitches found during the first and second observing runs of Advanced LIGO.	37
3.5	Single detector triggers in the PyCBC offline search with and without blip glitches.	39
3.6	Sensitivity reported by the PyCBC offline search with and without blip glitches.	39
3.7	Correlation between blip glitches and low inside relative humidity.	41
3.8	Optical configuration of the Advanced LIGO pre-stabilised laser.	42
3.9	Follow up of a PSL blip glitch throughout the interferometer.	43
3.10	Time-frequency representation of the computer blip glitches observed during the second observing run of Advanced LIGO.	44

4.1	Frequency and damping time posterior distribution for GW150914 . . . . .	51
4.2	Mass and spin posterior distribution for GW150914 . . . . .	52
4.3	Ringdown waveform with two quasi-normal modes . . . . .	53
4.4	Mass and spin posterior distribution for a simulated two-mode ringdown .	54
5.1	Post-Newtonian energy per unit mass at the 4PN order. . . . .	61
5.2	Different inspiral-cutoffs for neutron-star black-hole binaries and black-hole binaries. . . . .	62
5.3	Minimum Energy Circular Orbit for a test mass orbiting a Kerr black hole. .	64
5.4	Minimum Energy Circular Orbit of the hybrid energy introduced in this work. . . . .	65
5.5	Relative difference between the hybrid MECO and the exact Kerr MECO. .	66
5.6	Relative SNR between inspiral signals terminating at the hybrid MECO and terminating at the Schwarzschild Innermost Stable Circular Orbit. .	68
5.7	Hybrid MECO and the integrands cutoffs at the 3.5PN order. . . . .	69
5.8	Change on the hybrid MECO due to tidal effects. . . . .	71
6.1	Posterior distribution for the sky location obtained from the full simulated signal. . . . .	80
6.2	Posterior distributions of the inspiral results and Jensen-Shannon divergence between different posterior distributions. . . . .	82
6.3	Posterior distributions of the ringdown results and Jensen-Shannon divergence between different posterior distributions. . . . .	84
6.4	Whitened strain in each detector with the maximum posterior (MAP) waveform from the inspiral and ringdown analyses. . . . .	85
6.5	Posterior distribution on the area change. . . . .	86
6.6	Jensen-Shannon divergence between consecutive grid times of the inspiral and ringdown analyses using the ZDHP PSD. . . . .	86
6.7	Posterior distribution on the energy radiated during the coalescence. . .	87
6.8	Lines of constant area as function of the final mass and spin. . . . .	87
6.9	Posterior distribution on the area change for violations of the area increase law. . . . .	89

# Chapter 1

## Introduction

When gravitational wave detection becomes part of astronomy [...], gravity will no longer be silent. It will tell us its story directly. Gravity will speak to us.

---

*Gravity from the ground up*  
B. SCHUTZ

The end relics of stars after they have burned through their nuclear fuel is a compact object: a white dwarf, a neutron star, or a black hole. The particular outcome depends mainly on the mass, composition, and angular momentum of the original star. Smaller, lighter stars end their lives as white dwarfs, but more massive stars end their lives potentially through a supernova explosion resulting in a neutron star or a black hole. It is believed that the heaviest stellar-mass black holes are formed from direct collapse of the progenitor star, without production of a visible supernova. Studying compact objects is an important aspect to understand the lifecycle of stars in the universe and how they may impact galaxies and cosmology.

The lightest observed compact objects are white dwarfs. The Chandrasekhar limit [1, 2] establishes that the maximum mass of a stable white dwarf is  $\simeq 1.4M_{\odot}$ , where  $M_{\odot}$  is the mass of our sun. White dwarfs were first discovered in the triple star system 40 Eridani. This system contains a main sequence star in a distant orbit with a binary system containing a white dwarf. Although the binary in 40 Eridani was first observed in 1783 by William Herschel [3], it was not until the beginning of the 20th century that the star 40 Eridani B was classified as a white dwarf. As of 2012, about 20,000 white dwarfs had been classified using spectroscopic techniques [4].

Remnants with larger masses form neutron stars. Gravitational collapse compresses the core past the white dwarf density, making neutron stars the smallest and densest stars known to exist [5]. From the Tolman-Oppenheimer-Volkoff limit [6, 7], the maximum mass of a stable neutron star is  $\simeq 3M_{\odot}$ . Neutron-star observations date from the 1960s. In 1967, Iosif Shklovsky inferred from X-ray and optical measurements of Scorpius X-1 that the emission was from an accreting neutron star [8]. In that same

year, Jocelyn Bell and Antony Hewish detected the first radio pulsar [9], later identified as an isolated, rotating neutron star. At present more than 2,600 neutron stars are known from electromagnetic astronomy [10][11].

The heaviest compact objects are known as black holes: the star succumbs to gravitational collapse, an event horizon forms and, according to the Penrose singularity theorem [12], all the matter falls into a singularity. The Schwarzschild metric, published in 1916 [13], laid the mathematical groundwork to study black holes in General Relativity. However, it took several decades before the physical implications of the Schwarzschild spacetime in vacuum were fully understood. The event horizon is described as “*the boundary of the region from which particles or photons can escape to infinity in the future direction*” [14]. Matter or light that falls into the event horizon can therefore never come out, and isolated black holes do not emit any radiation (except for the hypothetical Hawking radiation). Interactions of black holes with matter provided the first black-hole candidate in 1972: Cygnus-X1. The X-ray source Cygnus-X1 is believed to originate from a binary system formed by a black hole accreting matter from its star companion. Currently, just over 100 black-hole candidates have been observed through electromagnetic radiation.

Compact objects are not necessarily isolated, but often forming binary systems. The first binary pulsar, PSR 1913+16, was discovered in 1974 by Russell A. Hulse and Joseph H. Taylor. The radio emission of the Hulse-Taylor binary pulsar, and the consequent studies of the binary’s orbit [15],[16], provided the first evidence for gravitational-wave emission from a compact binary as predicted by General Relativity. This effect was observed later in other binary pulsars as well [17]. The coalescence of binary systems formed by two compact objects<sup>1</sup>, known as *compact binaries*, are amongst the strongest sources of gravitational radiation detectable with current gravitational-wave detectors. The direct measurement of gravitational waves has been elusive for decades. In the year 2015, 100 years after the publication of General Relativity and 41 years after the discovery of the Hulse-Taylor binary pulsar, the first gravitational wave from a compact binary coalescence was detected with ground-based gravitational-wave observatories [18].

Here, we briefly review the topic of gravitational-wave astronomy. A simplified derivation of gravitational radiation from the linearised Einstein’s equations is presented in Sec. [1.1]. Throughout this work, we use geometrical units ( $G = c = 1$ ). Section [1.2] focuses on the characteristics of gravitational waves from compact binary coalescences, which are the main subject of this work. Section [1.3] introduces ground-based interferometric gravitational-wave detectors on Earth. Finally, Sec. [1.4] summarises the gravitational-wave detections thus far. An outline of the research presented in this work is given in Sec. [1.5].

---

<sup>1</sup>Henceforth, we will use the term *compact objects* to refer to neutron stars and black holes, excluding white dwarfs.

## 1.1 Gravitational waves

In Einstein's theory of General Relativity, astronomical systems with changing gravitational field emit gravitational waves. In fact, gravitational waves are a characteristic of any relativistic theory of gravity [19]. Here, we briefly summarise gravitational radiation obtained from Einstein's equations. Detailed derivation can be found in the literature [20–25].

Einstein's equation in geometrical units ( $G = c = 1$ ) with cosmological constant  $\Lambda = 0$  is given by:

$$R_{\mu\nu} - \frac{1}{2}Rg_{\mu\nu} = 8\pi T_{\mu\nu}, \quad (1.1)$$

where  $R_{\mu\nu}$  is the Ricci curvature tensor,  $R$  is the Ricci scalar,  $g_{\mu\nu}$  is the spacetime metric tensor, and  $T_{\mu\nu}$  is the stress-energy tensor. The left hand side of this equation is called the Einstein curvature tensor,  $G_{\mu\nu} = R_{\mu\nu} - \frac{1}{2}Rg_{\mu\nu}$ . In its most general form, Einstein's equation is a set of complicated non-linear second-order differential equations.

Only a few physically meaningful analytical exact solutions of Einstein's equations are known. For instance, the Friedmann-Robertson-Walker solutions used in cosmology, or the Kerr solution describing a stationary axisymmetric rotating black hole [26]. In general, attempts to solve Einstein's equations require certain approximations. Perturbation theory provides a method to simplify the equations when the deviation from an exact solution is small. The spacetime metric is decomposed into a background metric  $g_{\mu\nu}^b$ , which is the known exact solution, plus a small<sup>2</sup> perturbation  $h_{\mu\nu}$ :

$$g_{\mu\nu} = g_{\mu\nu}^b + h_{\mu\nu}. \quad (1.2)$$

Because  $|h_{\mu\nu}| \ll 1$ , higher order terms in the Einstein's equations can be neglected and the equations are linearised in  $h_{\mu\nu}$ .

The simplest case of perturbation theory is where the background metric is the flat Minkowski metric  $g_{\mu\nu}^b = \eta_{\mu\nu}$ . This is the so called linearised theory of gravity: a weak-field approximation to General Relativity. It is useful to define the tensor field  $\bar{h}_{\mu\nu} = h_{\mu\nu} - \frac{1}{2}h\eta_{\mu\nu}$  and work in the Lorenz gauge,  $\bar{h}^{\mu\nu,\nu} = 0$ . With this choice, the linearised Einstein's equations are given by

$$\square\bar{h}_{\mu\nu} = -16\pi T_{\mu\nu}, \quad (1.3)$$

where  $\square = \delta_\mu\delta^\mu = -\delta_0^2 + \nabla^2$  is the d'Alembert operator in flat space and the perturbation  $\bar{h}_{\mu\nu}$  simplifies the equations without loss of information. For the rest of this section we use this specific approach.

Far away from the source of gravitational radiation (in vacuum), the stress-energy tensor vanishes,  $T_{\mu\nu} = 0$ . The simplest solution to the vacuum linearised Einstein's equations is a plane-wave solution: linearised gravitational waves with propagation velocity equal to the speed of light. The extra degrees of freedom in  $\bar{h}_{\mu\nu}$  are reduced to

---

<sup>2</sup>In this context, that a metric tensor is small means that its components are much smaller than 1 in some global inertial coordinate system of the background metric [22].

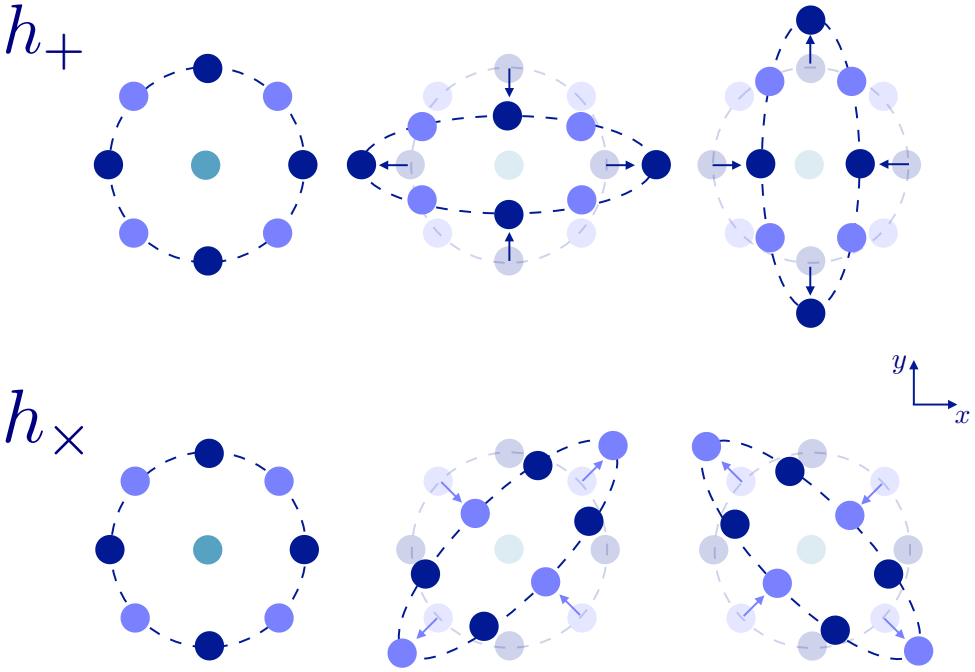


Figure 1.1: Effect of the gravitational wave's plus and cross polarisations on a ring of test particles. The lighter particles show the original position before the gravitational-wave perturbation. The wave is propagating in the  $z$ -direction.

two by means of the transverse-traceless (TT) gauge transformation. In this gauge the perturbation's trace vanishes, i.e.  $\bar{h}_{\mu\nu}^{TT} = h_{\mu\nu}^{TT}$ , and the waves are purely spatial, i.e. only the spatial components are non-zero ( $h_{\mu 0} = 0$ ). A plane, monochromatic wave in the TT gauge propagating in the  $z$ -direction is given by

$$h_{\mu\nu}^{TT}(t, z) = \begin{pmatrix} 0 & 0 & 0 & 0 \\ 0 & h_+(t-z) & h_\times(t-z) & 0 \\ 0 & h_\times(t-z) & -h_+(t-z) & 0 \\ 0 & 0 & 0 & 0 \end{pmatrix}. \quad (1.4)$$

The components  $h_+$  and  $h_\times$  are the two remaining physical degrees of freedom, called the *plus* and *cross* polarisations of the gravitational waveform. The effect of the two polarisations on a ring of test particles is shown in Fig. 1.1. In the TT gauge, the perturbation is always transverse to the direction of propagation. In the figure, waves are propagating in the  $z$ -direction and the perturbation affects only the  $x$ - $y$  plane.

The solutions to the linearised Einstein's equations in vacuum described above result in the propagation of gravitational waves. In general, to find how this gravitational radiation is generated by the source one has to solve Einstein's equations coupled to matter given in Eq. (1.3) (as we will see later, this is not the case for a perturbed Kerr

black hole for instance). For situations where the source's gravitational field is small (slow motion), solutions to the gravitational-wave perturbation can be expressed in terms of the source's lowest multipole moments. For electromagnetic radiation, the leading contribution comes from the second derivative of the electric dipole. However, there is no gravitational dipole radiation, because the second derivative of the gravitational mass and angular momentum dipoles both vanish. Therefore, the leading contribution to gravitational waves is given by the so called *quadrupole formula*:

$$h_{ij}^{TT} = \frac{2}{r} [\ddot{\mathcal{I}}_{ij}(t_r)]^{TT}, \quad (1.5)$$

where  $t_r = t - r$  is the retarded time, with  $r$  the distance from the observer to the centre of the source,  $\ddot{\mathcal{I}}_{ij}$  expresses the second time derivative of  $\mathcal{I}_{ij}$ , and  $\mathcal{I}_{ij}^{TT}$  is the transverse-traceless projection of the reduced quadrupole moment

$$\mathcal{I}_{ij}(t) = \int \rho(t) \left[ x^i x^j - \frac{1}{3} r^2 \delta_{ij} \right] d^3x. \quad (1.6)$$

Since the quadrupole is generally weaker than the dipole moment, gravitational waves are typically much weaker than electromagnetic waves. Higher multipoles contribute to the gravitational-wave emission through the so-called higher order modes. These modes are generally much weaker than the lowest order mode. However, there are certain situations for which the effect of these modes could become significant.

Spherically and axially symmetric situations do not emit gravitational waves. In principle, this includes core collapse of stars, supernova explosions or isolated compact objects. Sources of gravitational radiation are large, fast-rotating and asymmetric mass distributions. If supernova explosions occur asymmetrically, or rotating isolated neutron stars have asymmetries on their surface, they would be efficient radiators of gravitational waves. Meanwhile, coalescences of two compact objects are amongst the strongest sources of gravitational waves.

## 1.2 Compact binary coalescences

Two astrophysical bodies orbiting each other radiate energy in the form of gravitational waves. The energy loss of the system translates into the shrinkage of the orbital period, bringing the bodies closer together. The phase where the bodies are spiralling inwards is called the *inspiral*. In the absence of tidal disruption or magnetic fields, the two objects plunge into each other after the long inspiral to form a single object. This process is called the *merger* phase. The resulting object is initially highly perturbed, and emits gravitational radiation while settling down to equilibrium. In the case that the final object is a neutron star, there are different possible outcomes with different gravitational-wave imprint [27, 28]. However, if the final object is a black hole, the *ringdown* phase is the gravitational-wave emission by the black hole settling down to a stationary Kerr solution. In this section we review the gravitational-wave signature for the different phases of the coalescence.

### 1.2.1 Inspiral

During the early inspiral phase, the two compact objects are far apart and orbit in a non-relativistic Keplerian orbit. The gravitational radiation can be derived from modelling the binary as two point masses  $m_1$  and  $m_2$  in circular orbits [29]. To obtain the response of a gravitational-wave detector to the gravitational radiation from the inspiral, two coordinate systems are required: the source frame and the radiation frame. We use here the coordinate systems described in [30]. Solutions to the quadrupole approximation are given in this case by [30]:

$$h_+(t) = A(t) \frac{1 + \cos^2 \iota}{2} \cos \Phi(t), \quad (1.7)$$

$$h_\times(t) = A(t) \cos \iota \sin \Phi(t), \quad (1.8)$$

where  $\iota$  is the inclination angle of the source's orbital angular momentum to the line of sight toward the observer and  $\Phi(t)$  is the gravitational-wave phase, defined later. The gravitational-wave amplitude is given by

$$A(t) = \frac{4}{r} \mathcal{M}^{5/3} (\pi f_{\text{gw}})^{2/3}, \quad (1.9)$$

where  $r$  is the distance to the source, the gravitational-wave frequency  $f_{\text{gw}}$  equals twice the orbital frequency, and we have introduced the *chirp mass*

$$\mathcal{M} = \frac{(m_1 m_2)^{3/5}}{(m_1 + m_2)^{1/5}}. \quad (1.10)$$

Note that systems with larger chirp mass, i.e. larger masses or larger mass ratio ( $q = m_1/m_2$ ), result in larger amplitudes. For instance, binary black holes emit stronger gravitational radiation than binary neutron stars.

The orbital energy  $E$  and the energy flux  $\mathcal{F}$  (also referred to as radiated power  $P$  in the literature) provide an expression for the frequency  $f_{\text{gw}}$  as a function of time, and therefore for the phase  $\Phi(t)$ , through the energy-balance equation

$$\frac{d}{dt} E = -\mathcal{F}. \quad (1.11)$$

With the early inspiral approximations used above, this results in

$$f_{\text{gw}}(t) = \frac{\mathcal{M}^{-5/8}}{\pi} \left[ \frac{5}{256} \frac{1}{t_c - t} \right]^{3/8}, \quad (1.12)$$

$$\begin{aligned} \Phi(t) &= 2\pi \int f_{\text{gw}}(t) dt \\ &= -2 \left( \frac{t_c - t}{5\mathcal{M}} \right)^{5/8} + \phi_c, \end{aligned} \quad (1.13)$$

where  $t_c$  and  $\phi_c$  are the time and phase at coalescence (i.e., when the two objects touch each other). As  $t$  increases (while the orbit is decreasing due to the emission

of gravitational radiation), the gravitational-wave frequency (1.12) and therefore the amplitude (1.9) are gradually increasing. The gravitational-wave signal from a compact binary is therefore called a chirp. Here, we see that systems with larger chirp mass result in lower frequencies. Even though binary black holes are stronger sources of gravitational radiation, the gravitational-wave frequency at the coalescence is typically lower than for binary neutron stars. In the sensitive bandwidth of ground-based gravitational-wave detectors, the measurable gravitational wave from a black-hole coalescence is shorter than from a neutron-star merger.

Later in the orbit's evolution, the binary enters an early-relativistic regime. The inspiral picture is still valid qualitatively, but the previous approximations are no longer accurate. While the source is still slowly moving and weakly stressed, the post-Newtonian (PN) approximation provides the corrections to the late inspiral [31]. In the PN framework, the orbital energy and energy flux of the binary are given as a power series expansion in terms of the orbital velocity  $v$ . The energy-balance equation provides again expressions for the frequency and phase. The final result is a power series in  $v$ , from which (1.12) and (1.13) are the leading order terms. The intrinsic angular momenta of the compact objects (spins) modulate the gravitational waveform through spin-orbit and spin-spin couplings. These effects appear in the PN higher order terms, as can be seen from the full expressions of the energy  $E^{\text{PN}}(v)$  and energy flux  $\mathcal{F}^{\text{PN}}(v)$  given in Appendix C (up to the highest order currently known).

The post-Newtonian framework is applicable only during the inspiral phase, while the sources are still slowly moving. Despite its limitations, the PN approximation has proven to be an unexpectedly effective description even for nearly relativistic velocities [32]. The range of validity of the post-Newtonian framework is still a long lasting debate. In Chap. 5 we will discuss in more detail the end of the inspiral in the post-Newtonian approximation.

### 1.2.2 Merger and ringdown

The coalescence of two compact objects is a highly dynamical, highly relativistic phase that cannot rely on the approximations used for the inspiral. The late ringdown phase is known analytically from perturbation theory, as we will briefly see below. However, the gravitational-wave imprint of the merger and early post-merger phases remain unsolved analytically. The Numerical Relativity breakthrough in 2005 provided tools to solve Einstein's equations during a binary coalescence [33–35]. Nowadays, the full inspiral-merger-ringdown waveform for binary black holes is well known in many situations. Binary neutron stars involve complicated matter effects, but great progress has been made in numerical simulations of such systems as well [28].

For a rotating black hole, the generation of gravitational radiation during the ringdown phase is modelled through perturbation of the Kerr spacetime [36]. The background metric in Eq. (1.2) is that of the exact Kerr solution. The background symmetries allow to separate variables in the complicated perturbation equations, reducing the system to a set of linear ordinary differential equations. The Teukolsky equation [37–40] together with the appropriate boundary conditions provide solutions for perturbed black

holes. Namely, these boundary conditions are [36, 41]: (i) on the horizon, the wave must be physically ingoing in the frame of a physical observer, and (ii) at spatial infinity, the spacetime must be asymptotically flat. The characteristic oscillations of black holes are eigenmodes of this system of equations called quasi-normal modes. The late ringdown signal for a Kerr black hole consists of a superposition of these quasi-normal modes with the shape of exponentially damped sinusoids. The gravitational wave is commonly written in terms of spin-weighted spheroidal harmonics [42]  ${}_{-2}S_{lm}$ :

$$h_+ + ih_\times = \sum_{\ell,m,n} {}_{-2}S_{\ell m}(\iota, \varphi) A_{\ell mn} e^{i(\Omega_{\ell mn} t + \phi_{\ell mn})}, \quad (1.14)$$

The above sum is over the integer angular number  $\ell \geq 2$ , related to the eigenvalue of spheroidal harmonics, the integer azimuthal number  $m$ , with  $-\ell \leq m \leq \ell$ , and the integer overtones  $n \geq 0$ . The inclination angle  $\iota$  is the angle between the line-of-sight vector from the black hole to Earth and the spin of the black hole, and  $\varphi$  is the azimuth angle of the black hole with respect to the observer.  $A_{\ell mn}$  and  $\phi_{\ell mn}$  are the amplitudes and phases of each mode. These parameters depend on the configuration of the gravitational perturbation  $h_{\mu\nu}$  at the beginning of the ringdown phase, i.e. on the initial configuration of the binary. The complex frequencies  $\Omega_{\ell mn}$  are the quasi-normal frequencies determined from the Teukolsky equation. The real and imaginary parts of  $\Omega_{\ell mn}$  contain information about the oscillation frequency and the damping time of the damped sinusoid, respectively.

The frequency and damping time are characteristic of the black hole's mass and spin. It is therefore possible to estimate the intrinsic parameters of the remnant black hole by measuring particular quasi-normal modes from its ringdown. The fundamental  $(\ell, m, n) = (2, 2, 0)$  mode is the dominant mode, and higher order modes are typically much weaker. If two or more quasi-normal modes were to be observed, the additional modes would allow to test consistency with the Kerr solution [43], i.e. test the ‘no-hair’ theorem (stating that astrophysical black holes as solutions of General Relativity are completely characterised by their mass and angular momentum). In Chap. 4 we will lay the framework for parameter estimation of the ringdown's quasi-normal modes. However, higher order modes are not expected to be measurable within the next years. In Chap. 6 we will focus on the fundamental mode to develop a test of the black hole area increase law, which states that the horizon area of a black hole can only increase.

### 1.3 Interferometric gravitational-wave detectors

For decades, scientists believed that gravitational waves were too weak to ever be detected on Earth. The first proposals for interferometric gravitational-wave detectors appeared in the late 1950s. The main idea was to place free test masses in different locations and measure their separation with a laser interferometer. Current interferometric gravitational-wave detectors use two pairs of mirrors as test masses, positioned at the beginning and end of two right-angle arms. When a gravitational wave  $h(t)$  propagates through the interferometer, the relative positions of the test masses are slightly

perturbed in the way shown in Fig. 1.1. The variation in the optical path followed by the laser beam results into a variation in the interference pattern measured at the detector's output. Under the assumption that the signal's wavelength  $\lambda$  is much larger than the detector's arm length,  $\lambda \ll L$ , changes in the arm lengths  $L = L_x = L_y$  of the interferometer are given by

$$\delta L = h(t)L. \quad (1.15)$$

The wave amplitude  $h(t)$  physically represents a dimensionless strain. Because this amplitude is typically very small, interferometers with large arm length  $L$  are required to achieve a measurable  $\delta L$ . Changes in the arm lengths are measured through variations in the interference pattern at the photodetector: the relative phases of the light exiting the arm cavities are shifted when the gravitational wave changes the relative arm lengths. These phase fluctuations are given by [44, 45]

$$\Delta\phi(t) = 4\pi\nu_0 L h(t), \quad (1.16)$$

where  $\nu_0$  is the frequency of the light beam.

The gravitational wave produces an observable strain at the detector given by

$$h(t) = F_+(\theta, \phi, \Psi) h_+(t) + F_\times(\theta, \phi, \Psi) h_\times(t). \quad (1.17)$$

The altitude and azimuth angles  $(\theta, \phi)$ , which indicate the location of the source in the sky, are the spherical polar coordinates of the unit vector pointing towards the source with respect to the detector's cartesian coordinates [46]. The polarisation angle  $\Psi$  defines the relative orientation of the wave frame with the detector coordinate system. The functions  $F_{+,\times}$  are the detector antenna pattern functions, determined by the detector's geometry and the source's location. For interferometric detectors, these functions are [24]

$$F_+(\theta, \phi, \Psi) = \frac{1}{2}(1 + \cos^2 \theta) \cos 2\phi \cos 2\Psi - \cos \theta \sin 2\phi \sin 2\Psi, \quad (1.18)$$

$$F_\times(\theta, \phi, \Psi) = \frac{1}{2}(1 + \cos^2 \theta) \cos 2\phi \sin 2\Psi + \cos \theta \sin 2\phi \cos 2\Psi. \quad (1.19)$$

In general, the antenna pattern functions are time dependent because the angles  $(\theta, \phi, \Psi)$  are defined relative to the detector coordinate system and vary as the Earth rotates. However, the duration of a compact binary signal within the sensitive bandwidth of ground-based detectors is much shorter than the Earth rotation period. Therefore, the above expression is a good approximation for compact binary coalescences. We will see the techniques currently used to detect the strain induced by a gravitational-wave signal in Chap. 2.

The two Laser Interferometer Gravitational-wave Observatories (LIGO) were built in the late 1990s in the United States: one on the Hanford site in Washington state and one in Livingston, Louisiana. The first generation of ground-based gravitational-wave observatories consisted of a network of detectors distributed around the world: the two Initial LIGO detectors, Virgo in Italy, GEO600 in Germany, and TAMA300 in Japan. These detectors were intermittently collecting data during several observing runs

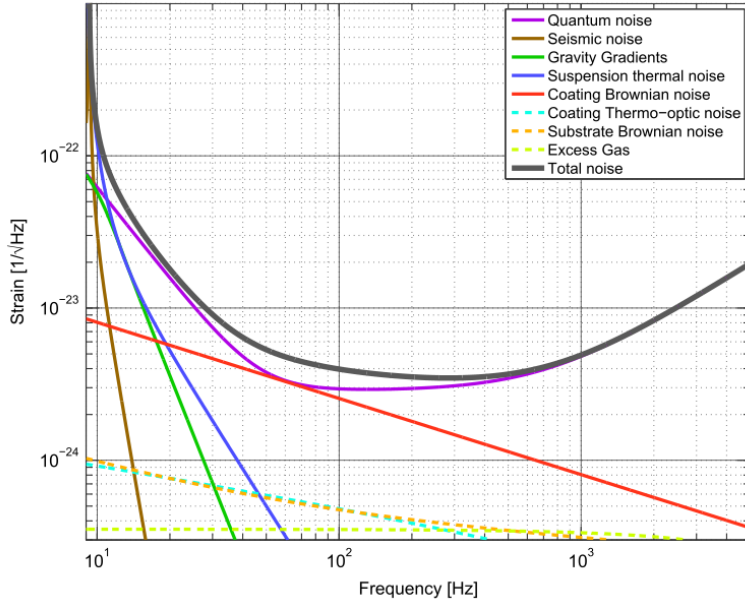


Figure 1.2: Amplitude spectral density as a function of frequency for the design sensitivity of Advanced LIGO detectors, shaped by the principal expected noise terms. Original image in [48].

between the years 2002-2011. Afterwards, the LIGO and Virgo detectors were switched off to undergo major upgrades aimed towards the second generation of ground-based gravitational-wave observatories. Advanced LIGO started its first observing run (O1) in September 2015, lasting for four months, and its second observing run (O2) in November 2016, lasting for ten months. Virgo joined the second generation network in August 2017. At the time of this writing, the Advanced LIGO and Virgo detectors are in the middle of a commissioning break, which means that efforts are underway to further improve their sensitivity before the next observing run by the end of 2018. Design sensitivity is expected to be achieved between the years 2019-2021 [47].

The noise floor of ground-based interferometric gravitational-wave detectors is mainly determined by the fundamental noise sources: thermal noise and quantum noise [48][49]. Thermal noise, which appears stronger at lower frequencies, arises from the test masses and their suspension systems. Quantum noise includes (i) shot noise at high frequencies, which originates from statistical fluctuations in the photon count at the photodiodes, and (ii) radiation pressure at low frequencies, due to momentum transfer to the test masses from high-laser power circulating in the arm cavities. Seismic noise is the main limiting factor at low frequencies and determines the lowest observable gravitational-wave frequencies. Other noise sources are classified as technical noises and are controllable by design. Figure 1.2 shows the principal noise terms for the design sensitivity of Advanced LIGO. In Chap. 3, we will give more details about the configuration of the Advanced LIGO detectors and about short noise transients present in the data.

## 1.4 Astrophysical gravitational-wave signals

The first gravitational wave observed by the LIGO detectors, GW150914, passed through the Earth on 14th of September 2015 [18]. This signal was not only the first direct detection of gravitational waves, but also the first observation of a stellar-mass binary black hole. Because black holes do not emit electromagnetic radiation, the existence of stellar-mass binary black holes prior to this discovery remained a theoretical prediction (galactic nuclei are likely candidates of supermassive binary black holes). Furthermore, the remnant black hole GW150914 is the stellar-mass black hole with the largest mass ever observed. At present, a total of five confirmed binary black holes and one candidate binary black hole have been announced [18, 50–54]. In addition, the second observing run of Advanced LIGO jointly with Virgo concluded with a very interesting discovery: GW170817, a gravitational-wave signal most likely from the coalescence of two neutron stars [55]. A short gamma-ray burst was observed independently, arriving within seconds of the gravitational-wave signal and consistent with the location of the binary neutron star. Further electromagnetic radiation from the source was detected within the following hours and days, consistent with the predicted kilonova emission in such type of coalescences [56]. Joint gravitational-wave and electromagnetic observations allowed localisation of the source to the NGC 4993 galaxy.

Some of the parameters reported in [51–55] for the detected gravitational-wave signals are given in Table 1.1. In the case of the binary neutron star, the coalescence happens

Table 1.1: Properties of the different astrophysical signals as reported in [51–55]. The parameters given here are the median values with 90% credible intervals that include statistical and systematic errors. The individual masses  $m_1$ ,  $m_2$  and the final mass  $M_f$  are given in the source frame; conversion to the detector frame follows from multiplying by  $(1+z)$ , with  $z$  the source redshift of the signal. The term  $\chi_{\text{eff}} = (\chi_1 m_1 + \chi_2 m_2) / (m_1 + m_2)$  gives a measurement of the individual spins.  $\chi_f$  is the dimensionless spin of the remnant black hole, and  $D_L$  the luminosity distance to the source. For the BNS GW170817, we report the chirp mass  $\mathcal{M}$  instead of the individual masses.

Event	$m_1 (M_\odot)$	$m_2 (M_\odot)$	$\chi_{\text{eff}}$	$M_f (M_\odot)$	$\chi_f$	$D_L (\text{Mpc})$
GW150914	$36.2^{+5.2}_{-3.8}$	$29.1^{+3.7}_{-4.4}$	$-0.06^{+0.14}_{-0.14}$	$62.3^{+3.7}_{-3.1}$	$0.68^{+0.05}_{-0.06}$	$420^{+150}_{-180}$
LVT151012	$23^{+18}_{-6}$	$13^{+4}_{-5}$	$0.0^{+0.3}_{-0.2}$	$35^{+14}_{-4}$	$0.66^{+0.09}_{-0.10}$	$1000^{+500}_{-500}$
GW151226	$14.2^{+8.3}_{-3.7}$	$7.5^{+2.3}_{-2.3}$	$0.21^{+0.20}_{-0.10}$	$20.8^{+6.1}_{-1.7}$	$0.74^{+0.06}_{-0.06}$	$440^{+180}_{-190}$
GW170104	$31.2^{+8.4}_{-6.0}$	$19.4^{+5.3}_{-5.9}$	$-0.12^{+0.21}_{-0.30}$	$48.7^{+5.7}_{-4.6}$	$0.64^{+0.09}_{-0.2}$	$880^{+450}_{-390}$
GW170608	$12^{+7}_{-2}$	$7^{+2}_{-2}$	$0.07^{+0.23}_{-0.09}$	$18.0^{+4.8}_{-0.9}$	$0.69^{+0.04}_{-0.05}$	$340^{+140}_{-140}$
GW170814	$30.5^{+5.7}_{-3.0}$	$25.3^{+2.8}_{-4.2}$	$0.06^{+0.12}_{-0.12}$	$53.2^{+3.2}_{-2.5}$	$0.70^{+0.07}_{-0.05}$	$540^{+130}_{-210}$
GW170817	$\mathcal{M} = 1.188^{+0.004}_{-0.002}$			Unknown	Unknown	$40^{+8}_{-14}$

at frequencies that are above the current sensitive bandwidth of the Advanced LIGO and Virgo detectors. The full inspiral-merger-ringdown signature for this type of event depends on the equation of state of the neutron stars, which is not known *a priori*. Without accurate models for the remnant of a neutron star coalescence, and with not enough sensitivity at the corresponding frequencies, the final object's parameters remain unknown. In the table, we show the chirp mass instead of the individual masses. This is due to the fact that the individual masses are highly affected by the degeneracy between mass ratio and spins. Constraints on the individual masses depending on the spin prior are given in [55].

## 1.5 Outline

This work concerns observations of compact binary coalescences, covering all the way through from detection techniques to properties of signals. The first chapters are related to the analysis of Advanced LIGO data. Chapter 2 introduces gravitational-wave searches for compact binaries in Advanced LIGO, explaining procedures showing real results. As we will see, there is a particular type of noise transients that affect the sensitivity of these searches. Chapter 3 describes such transients, developing techniques to find occurrences in the data and investigating their origin. The last chapters are related to source modelling and properties. Chapter 4 develops a method to infer the mass and angular momentum of the remnant black hole using parameter estimation techniques on the ringdown part of the signal. Chapter 5 introduces a method to model the end of the inspiral phase using the post-Newtonian approximation and the exact Kerr solution. Chapter 6 uses the tools described in the previous two chapters to develop a test of one of the most celebrated results in exact non-linear relativity: the second law of black hole thermodynamics. Finally, we conclude and summarise results in Chap. 7.

# Chapter 2

## Searches for gravitational waves with PyCBC

Gravitational-wave signals are buried in detector noise. Search pipelines are designed to identify astrophysical signals in the noise-dominated data. Furthermore, search pipelines compute the statistical significance of candidate signals. The sensitivity to different types of signals and the significance estimate depend on the method used by the search pipeline.

Different types of signals are identified using different search methods. For instance, rotating asymmetric neutron stars emit continuous low amplitude gravitational waves over long periods of time. Search pipelines for such signals require therefore long stretches of data and long integration times [57]. Short transient signals, also known as bursts, can be quickly identified in short segments of data. Burst searches detect times when the power of the time-frequency data is above the baseline detector noise [58]. This type of search requires minimal assumptions about the signal morphology. Gravitational waves from core collapse supernovae or exotic unknown events are most likely to be identified with burst searches.

Gravitational waves from binary black hole mergers are short transients also identifiable by burst searches. However, matched filtering is the optimal method to search for putative signals in stationary Gaussian noise. The full solution to the two-body problem has not been solved analytically in General Relativity. For certain realistic scenarios (such as circular orbits and similar masses), a combination of analytical and numerical methods provides relativistic models of the gravitational waveforms emitted by compact binaries [59, 60]. Therefore, modelled searches are the most sensitive to identify such compact binary signals, assuming that General Relativity is the correct description for these systems.

PyCBC [61, 62] is a modelled search pipeline for compact binary coalescences. This pipeline is a Python software package [63] to support a modern implementation of the FINDCHIRP algorithm [64]. The PyCBC search consists of two pipelines: the low-latency search, called PyCBC Live, and the high-latency search, also known as offline search. The low-latency search is aimed to identify candidate signals with a latency of tens of seconds to minutes after data acquisition. The high-latency search provides

the highest sensitivity on the most reliable data, aimed to detect events missed by the low-latency search and to estimate the statistical significance of candidate signals. This chapter describes the PyCBC offline searches.

The chapter is organised as follows. The PyCBC pipeline is described at the beginning of the chapter. The PyCBC software, developed for the second generation of ground-based gravitational-wave observatories, was chiefly authored by Alex Nitz, Ian Harry, Josh Willis, Duncan Brown and Tito Dal Canton. Section 2.1 describes the principles used to analyse data from one gravitational-wave detector. Section 2.2 explains the coincidence test and the statistical significance calculation. The rest of the chapter describes the procedure followed in the first observing runs of Advanced LIGO to run the offline searches. Section 2.3 explains offline searches and the difference between closed box and open box results. The author led the offline searches over several periods of data, and the following sections are based on that work: Sec. 2.4 presents and explains closed box results, showing real examples; Sec. 2.5 presents open box results, also showing real examples. All the results shown in these sections are from offline searches led by the author. Finally, the chapter is summarised in Sec. 2.6.

## 2.1 Single detector data analysis

The first step in the PyCBC compact binary search is to analyse the data from a single gravitational-wave detector<sup>1</sup>. The strain induced by a compact binary on a particular detector, given by Eq. (1.17), can be re-written as [46, 64, 65]

$$h(t) = A(t) \cos [\Phi(t) + \varphi] . \quad (2.1)$$

The response of the detector depends on the sky location  $(\theta, \phi)$ , the polarisation angle  $\Psi$ , and the inclination angle  $\iota$ . These angles (together with the coalescence time, coalescence phase, and distance to the source) are called the extrinsic parameters of the binary, because they only affect the overall amplitude, phase and time shift of the gravitational waveform. For simplicity, we neglect here higher order multipoles and post-Newtonian corrections. In Chap. 1, we saw an approximation of the amplitude for the early inspiral stage of a gravitational-wave signal. The amplitude depends on the distance  $r$  from the observer to the source. The strain amplitude at the gravitational-wave detector can be written in terms of the effective distance  $r_{\text{eff}}$ . The effective distance combines the extrinsic angle parameters and the physical distance to the source into one single parameter:

$$r_{\text{eff}} = r \left[ F_+^2(\theta, \phi, \Psi) \left( \frac{1 + \cos^2 \iota}{2} \right)^2 + F_\times^2(\theta, \phi, \Psi) \cos^2 \iota \right]^{-1/2} , \quad (2.2)$$

where the functions  $F_+(\theta, \phi, \Psi)$  and  $F_\times(\theta, \phi, \Psi)$  are the antenna pattern functions defined in Eqs. (1.18) and (1.19). The effective distance is typically greater than the true distance. When the binary's orbit is face-on ( $\iota = 0$ ) or face-off ( $\iota = \pi$ ), and the source's

---

<sup>1</sup>Alternatively, the coherent method first combines the data of multiple detectors.

location is directly above or below the detector, then  $r_{\text{eff}} = r$ . The phase  $\varphi$  in Eq. (2.1) is given by

$$\varphi = \frac{1}{2} \arctan \left( \frac{2 \cos \iota F_X(\theta, \phi, \Psi)}{(1 + \cos^2 \iota) F_+(\theta, \phi, \Psi)} \right). \quad (2.3)$$

The PyCBC pipeline is an all-sky search for unknown compact binary signals. This means that the phase, amplitude and arrival time, and therefore the extrinsic parameters, are maximised over in the search, as we will see below.

The underlying principle of modelled compact binary searches is matched filtering [66]. Waveform models predicted by General Relativity are correlated with detector data to obtain a measurement of the signal-to-noise ratio (SNR):

$$\rho^2(t) = \frac{|\langle s|h\rangle(t)|^2}{\langle h|h\rangle}, \quad (2.4)$$

with  $h(t)$  a waveform template dependent on the coalescence time (as seen in Chap. 1) and  $s(t)$  the detector data strain. Brackets  $\langle . | . \rangle$  denote the noise-weighted inner product

$$\langle s|h\rangle(t) = 4 \Re \left( \int_0^\infty \frac{\tilde{s}(f)\tilde{h}^*(f)}{S_n(f)} df \right), \quad (2.5)$$

where  $S_n(f)$  is the one-sided power spectral density (PSD) of the detector's noise,  $\tilde{h}(f)$  is the Fourier transform of  $h(t)$  and  $*$  indicates complex conjugation. In practice, the lower limit of the integral is chosen as the detector's effective low-frequency sensitivity limit, below which the detector is dominated by seismic noise. The upper limit of the integral is the minimum of the template's end frequency and the Nyquist frequency. The matched-filter SNR (2.4) is maximised over phase, amplitude and arrival time. Maximisation over amplitude arises from the normalisation  $\langle h|h\rangle$  in (2.4), and maximisation over the initial phase is computed analytically. Maximising the SNR over time can be done numerically by means of the Fourier transform [64].

Having maximised over the extrinsic parameters, the remaining unknown parameters shaping the waveform are the individual masses and the intrinsic angular momenta (spins) of the compact objects. These parameters are called the intrinsic parameters of the binary. To find unknown signals in the data, the matched filtering is performed using a discrete set of templates that covers a chosen region of the intrinsic parameter space. This set of templates is called the template bank. In the first observing run of Advanced LIGO (O1), the template bank included waveforms with a total mass larger than one solar mass and  $M = m_1 + m_2 \leq 100M_\odot$  [67], where  $m_i$  are the masses of the individual objects. In the second observing run of Advanced LIGO (O2), the template bank was extended to include masses  $M \leq 500M_\odot$ , with the condition that the waveform duration in the detector sensitivity band had to be greater than 150 ms [68]. In both cases, the individual spins of the objects were aligned with the orbital angular momentum, and the dimensionless magnitudes of the spins were  $\chi_i \leq 0.05$  for objects with  $m_i \leq 2M_\odot$  and  $\chi_i \lesssim 0.99$  otherwise.

While matched filtering is an efficient technique for stationary Gaussian noise, detector data contains non-stationary noise and non-Gaussian noise transients (also known as glitches) [69]. Data quality (DQ) investigations are performed to identify glitches and periods of poor detector performance. When there is a known issue in the detector’s behaviour and data are badly contaminated, the corresponding time period is flagged as a category 1 (CAT1) veto. CAT1 times are highly non-stationary and can affect noise estimations of neighbouring clean data. Therefore, CAT1 times are removed before estimating the PSD and performing the analysis [70]. This is the first step to fold the DQ information into the search pipeline. Further data quality investigations involving short noise transients are used in a second step after the matched filtering analysis, as we will see below.

The PyCBC pipeline implements a method called gating to remove loud, short glitches prior to the matched-filtering analysis. Gating consists of applying an inverse Tukey window at a specific time to eliminate the glitch. With this window function, data around the gated time is zeroed out and then smoothly rolled back to the surrounding noise level. Times of glitches, if known, can be passed to the pipeline through a gating file, such as was done for the binary neutron star GW170817 [55]. Unknown glitches can be identified by the pipeline itself in a process called auto-gating. The identification of glitches by the pipeline occurs by means of the whitened data strain: the input time series is Fourier transformed to the frequency domain, whitened using the amplitude spectral density (ASD) measured by the pipeline, and inverse Fourier transformed back to the time domain. Times where the amplitude of this whitened strain exceeds a certain threshold are identified as loud glitches and removed by gating.

The matched filtering is performed on data remaining after the CAT1 vetoes and the gating process. Times with a measured SNR greater than a predetermined threshold are called triggers. One event can generate many triggers, and real compact binary signals have a narrow peak in the SNR time series. The pipeline clusters triggers in predefined time windows, and for each waveform template only the trigger with the maximum SNR in a time window is stored. Despite noise removal prior to the matched filtering, many triggers originate from noise transients still present in the data. Therefore, the SNR defined in Eq. (2.4) is not a convenient detection statistic. The PyCBC pipeline performs the  $\chi^2$  signal-consistency test [71] to distinguish between signals and glitches.

The  $\chi^2$  statistic is a signal-consistency test used to establish if the power in the data is distributed consistently with the power in the matching template. The procedure consists of dividing the frequency domain data into  $p$  frequency bins. These bins are chosen such that the power expected from the template is the same in each bin [71]. The reduced  $\chi^2$  is defined by:

$$\chi_r^2 = \frac{p}{2p-2} \frac{1}{\langle h|h \rangle} \sum_{i=1}^p \left| \langle s|h_i \rangle - \frac{\langle s|h \rangle}{p} \right|^2, \quad (2.6)$$

where  $h_i$  is the part of the template corresponding to the  $i$ th frequency bin. The parameter  $p$  is chosen empirically: in Advanced LIGO searches, the number of bins is template dependent. Concretely, the gravitational-wave frequency at the template’s peak

amplitude determines the number of bins. If the trigger is a real signal embedded in Gaussian noise, the reduced  $\chi^2$  distribution takes values close to one, while larger values are an indication of non-Gaussian noise transients. Based on this statistic, the re-weighted SNR is defined as

$$\hat{\rho} = \begin{cases} \rho / [(1 + (\chi_r^2)^3)/2]^{1/6} & \text{if } \chi_r^2 > 1, \\ \rho & \text{if } \chi_r^2 \leq 1. \end{cases} \quad (2.7)$$

Only triggers with a re-weighted SNR greater than a specific value are stored as the final output of the single detector analysis.

The  $\chi^2$  test is less effective for short duration templates at distinguishing between noise transients and signals. As we will see later, some short duration noise transients are particularly resistant to the  $\chi^2$  statistic<sup>2</sup>. During the second run of Advanced LIGO (O2), a new ranking statistic was developed to down-rank a subset of these noise transients. This subset is characterised by an excess power at frequencies above the final frequency of the templates that best match the glitches. The new statistic places a series of sine-Gaussian tiles at the time of the trigger and at frequencies where the true astrophysical signal is not expected to contain any power. The new  $\chi^2$  is then given by [72]

$$\chi_{r,sg}^2 = \frac{1}{2N} \sum_{i=1}^N \rho_i^2, \quad (2.8)$$

where  $N$  is the number of sine-Gaussian tiles and  $\rho_i$  is the signal-to-noise ratio at each tile. Finally, the new ranking statistic is given by

$$\hat{\rho}_{sg} = \begin{cases} \hat{\rho} (\chi_{r,sg}^2 / 4)^{-1/2} & \text{if } \chi_{r,sg}^2 > 4, \\ \hat{\rho} & \text{if } \chi_{r,sg}^2 \leq 4. \end{cases} \quad (2.9)$$

This sine-Gaussian re-weighted SNR was introduced later in O2.

After the matched filtering analysis, the search pipeline performs the second step of the data quality: the category 2 (CAT2) vetoes. CAT2 times correspond to instrumental or environmental noise transients of identified origin that can generate loud triggers, but do not contaminate the surrounding data to affect the performance of the PSD estimation. At this point in the search pipeline, single detector triggers are discarded if they are in coincidence with times flagged as CAT2 vetoes. The remaining triggers are required to undergo the coincidence test.

## 2.2 Coincidence between detectors

In the single detector analysis, noise transients are removed through data quality vetoes and gating techniques. However, glitches of unknown origin cannot be safely vetoed.

---

<sup>2</sup>Later in this chapter we will mention this type of noise transient and call them ‘blip glitches’. A more detailed description of blip glitches will follow in the next chapter.

Therefore, even after folding in all the data quality information, triggers that survived the gating and the signal-consistency tests can still originate from detector noise (either from non-Gaussian glitches or from random fluctuations in Gaussian noise). Ensuring that a signal is consistently observed in two or more detectors, known as coincidence between detectors, is a required test in the PyCBC pipeline to support the astrophysical origin of a trigger. This test consists of two simple conditions: (i) the template associated to the trigger has to be the same in all detectors, and (ii) the time of the trigger must be consistent with the arrival time difference between detectors. For the case of the two LIGO detectors<sup>3</sup>, the maximum arrival time difference allowed to establish coincidence is 15 ms: 10 ms for the maximum travel time between the detectors plus 5 ms to account for timing uncertainties. Triggers that meet the two coincidence requirements are considered candidate events, also known as foreground events. The coincident ranking statistic, also called the detection statistic, is given by the quadrature sum of the re-weighted SNR in each detector (the combined SNR):

$$\hat{\rho}_c = \sqrt{\hat{\rho}_H^2 + \hat{\rho}_L^2}, \quad (2.10)$$

with  $\hat{\rho}_H$ ,  $\hat{\rho}_L$  the re-weighted SNR at the Hanford and Livingston detectors, respectively. This detection statistic was used during the first observing run of Advanced LIGO (O1). We will see below how the combined SNR was updated for the second observing run of Advanced LIGO (O2).

To obtain the statistical significance of a candidate event, the pipeline estimates the background distribution of the search. Because gravitational-wave detectors cannot be shielded from gravitational-wave signals, the pipeline measures the background distribution by repeatedly time shifting the data of each detector with respect to the other detectors. This time shift is larger than the coincidence time window to ensure that there are no astrophysical correlations between the shifted data sets. Triggers that meet the coincidence requirements in the time shifted data are called background triggers. The “false coincidences” from the background triggers are used to calculate the false-alarm rate of the search as a function of the detection statistic, as we will see later.

In practice, different templates yield different background distributions. A template’s duration is determined by the amount of time the template spends in the detector’s sensitivity band. Short templates result in a larger number of background triggers because short noise transients are frequent in detector data. This means that short binary black hole signals (we saw in Chap. 1 that larger chirp masses yield lower gravitational-wave frequencies) have a different false-alarm rate than long binary neutron star signals with the same value of the coincident ranking statistic. In the first observing run of Advanced LIGO, candidate and background events were divided into three search classes based on template length (or total mass). The significance of a particular candidate event was then determined by the background distribution of its own class. A trials factor in the significance, equal to the number of classes, would account for searching over multiple classes.

---

<sup>3</sup>From now onwards we restrict ourselves to the case of the two LIGO detectors.

For the second observing run of Advanced LIGO (O2), a new detection statistic has been defined to improve the sensitivity of the PyCBC search [73]. This new statistic introduces information from the arrival time difference between detectors,  $\delta t = t_H - t_L$ , the phase difference,  $\delta\phi = \phi_h - \phi_L$ , and the signal-to-noise ratios in each detector,  $\rho_H$  and  $\rho_L$ . Signal events have a specific distribution over  $(\rho_H, \rho_L, \delta t, \delta\phi)$ , determined by the source's sky location and orientation. Noise events, however, are uniformly distributed in  $(\delta t, \delta\phi)$ , provided that noise is uncorrelated between detectors. Furthermore, a better noise background model for the entire search space is achieved by accounting for the noise distribution of each individual template. Therefore, the masses and the spins of the candidate event are also folded into the new statistic. With this method, the search classes used in O1 are not necessary. Given the set of parameters mentioned above, which we call  $\vec{\vartheta}$ , the improved detection statistic is defined as

$$\varrho^2 = 2 \left[ \log p^S(\vec{\vartheta}) - \log p^N(\vec{\vartheta}) \right] + \text{constant}, \quad (2.11)$$

where  $p^S(\vec{\vartheta})$ ,  $p^N(\vec{\vartheta})$  are approximations to the signal distribution and the noise distribution, respectively. This detection statistic recovers the combined SNR defined in Eq. (2.10) when the noise is stationary and Gaussian.

Now we proceed to calculate the significance of a foreground event. Given a candidate event with detection statistic  $\varrho$  (or  $\hat{\rho}_c$  in the O1 searches), its  $p$ -value is the probability that one or more noise background events have a detection statistic equal to or greater than  $\varrho$ . Suppose that for an observation time  $T$  and background time from time shifts  $T_b$ , there are  $n_b(\varrho)$  noise background events with detection statistic above the candidate event's. The  $p$ -value is then given by

$$p(\geq 1 \text{ noise event above } \varrho | T, T_b) = 1 - \exp \left[ \frac{-T(1 + n_b(\varrho))}{T_b} \right]. \quad (2.12)$$

The false-alarm rate is defined by the quantity  $(1 + n_b(\varrho))/T_b$  and indicates the rate of false positive events more significant than a given candidate event.

Candidate events with a false-alarm rate smaller than 1 per 100 years are confident gravitational-wave signals and are labelled as GW by the LIGO and Virgo Collaborations. All the confident gravitational-wave signals observed to date have false-alarm rates much smaller than this threshold [18, 50, 52–55]. A candidate event that does not reach such a statistical significance but stands out from the background distribution, with a high probability of being of astrophysical origin, is labelled as LIGO-Virgo Trigger (LVT). This category is only granted if the candidate event is free from obvious instrumental artefacts. In the following sections, we are going to describe the process of running a search to assess the statistical significance of gravitational-wave candidates, and show a few examples from searches that were run by the author. This includes the search that found LVT151012, and the search that established the statistical significance of GW170814 and GW170817.

## 2.3 Offline searches

Identifying transient candidate signals in the data does not require long observation and background times. Low-latency searches use short segments of data to find candidate events within minutes of data acquisition and share the information with electromagnetic astronomical observing partners. If the source of gravitational waves also emits electromagnetic radiation, for instance the binary neutron star GW170817 [55], low latency is crucial to identify electromagnetic counterparts that require pointing narrow field of view telescopes. To assess the statistical significance of a candidate event and claim a confident detection, a certain amount of observation and background times are required. The significance estimate from low latency searches is very limited, with false-alarm rates no smaller than 1 per 100 years with PyCBC Live. In fact, most of the candidate events shared with electromagnetic partners do not result in significant events after further analysis.

The offline searches, with a latency of a few weeks, establish the statistical significance of a candidate event. Occasionally, the offline searches can also identify candidate events missed by the low-latency searches. In the Advanced LIGO observing runs, the offline analysis was performed on data segments of at least five days of coincident data between detectors. This means five days of data where both detectors were functioning in their undisturbed nominal configuration, also called observation state. The amount of background time is given by  $T_b = T^2/\delta$ , with  $T$  the amount of observed data and  $\delta$  the time shift interval used to estimate the background distribution [62]. For five days of observed data, and time shifts  $\delta = 0.1$  s, then  $T_b \simeq 5.9 \times 10^4$  yrs. This background time translates into a minimum measurable false-alarm rate of 1 in  $5.9 \times 10^4$  yrs, or equivalently a minimum measurable  $p$ -value of  $2.3 \times 10^{-7}$ . These values represent a sufficient statistical significance to claim a confident detection.

One important characteristic of the offline analysis is the distinction between *closed box* and *open box* results. In the closed box results, all foreground events have been removed from the background distribution measurement. Open box results, which are final results that include all foreground events, are temporarily hidden. This was originally intended for the data analysts to perform unbiased data quality and sanity checks. If the analysis and data quality leaders knew there is a gravitational-wave signal in the data, they would unconsciously try to increase the significance of the signal. Only after all inspections are performed in the closed box results and noise transients from known origin have been vetoed from the search, the analysis leader can proceed to make the open box results available.

With most of the gravitational-wave detections occurring in low-latency searches, the analysis leader unavoidably knows about the existence of high confidence signals in the data. However, the closed box method will still hide marginal candidate events not found in low latency. The candidate event LVT151012 [18, 51] found during the first observing run of Advanced LIGO (O1) is an example of an unexpected surprise in the open box results.

## 2.4 Closed box results

Results from the offline analysis are shown in HTML format and can be accessed online with LIGO or Virgo credentials. During the analysis of closed box results, the open box results are not accessible by anybody. Several sections in the results pages, shown in Fig. 2.1, help diagnose issues in the data and/or in the analysis. The analysis leader works closely with the Detector Characterisation (DetChar) group to identify data issues. In this section, we show closed box results for the analysis of data from the 8th to the 20th of October 2015 [74]. This analysis, with approximately 5.78 days of coincident data, contained the candidate event LVT151012 [18, 51].



Figure 2.1: Different sections in the results pages from the PyCBC offline analysis, destined to provide information that allow diagnosis of issues in the data and/or in the analysis.

### 2.4.1 Summary page

The summary page recapitulates the most important information from the analysis. Usually this is the main page presented to the broader working group before showing open box results. The analysis leader performs basic sanity checks such as corroborating the start and end times of the analysis and the amount of coincident data. Further information contained in the summary page is discussed below. This information offers a first glance to identify problematic noise transients or analysis issues.

A preliminary diagnosis of possible major issues in the data can be obtained from the amplitude spectral density and the inspiral range measured in the search, shown in Fig. 2.2. These are usually compared with previous analyses to ensure that the performance of the detectors is not significantly degrading. The summary page only shows the inspiral range for a binary neutron star merger with  $m_1 = m_2 = 1.4M_{\odot}$ . Inspiral ranges for other compact binary systems are found under “Detector sensitivity.” A time with major data issues degrades the detector sensitivity and often appears as an abrupt inspiral range drop.

Histograms of the background SNR and re-weighted SNR show if there is an excess of noise transients in the data. One of the main goals of the closed box results is to find noise transients that cause high re-weighted SNR triggers in the background distribution, and assess if they can be vetoed before the coincidence test. Therefore, the loudest background triggers are followed up individually, as we will see later. When times of known instrumental noise transients are identified, a data quality flag is assigned to those times indicating that they should be vetoed by the analysis. The search analysis is then repeated with the new DQ information.

Figure 2.3 shows the resulting background triggers after incorporating all DQ information available. As can be seen, there is a ‘tail’ of background triggers with greater

re-weighted SNR (in this specific case, the tail is more noticeable in the Livingston detector, but this could appear on any or both detectors). These triggers are usually due to a specific type of noise transients known as blip glitches. Blip glitches are amongst the most harmful noise transients in the transient searches because they survive the  $\chi^2$  signal-consistency test. The origin of blip glitches is unknown, therefore it is not possible to veto them from the search. We will discuss blip glitches in the next chapter.

The sensitivity of a PyCBC search is estimated with Monte Carlo methods. During the matched-filter analysis, a large number of simulated signals (injections) are added to the data. The fraction of injections that the pipeline is able to identify at a given false-alarm rate gives a measure of the sensitive volume [62]. The summary page shows the missed injections during the analysis (i.e. the injections that the pipeline could not

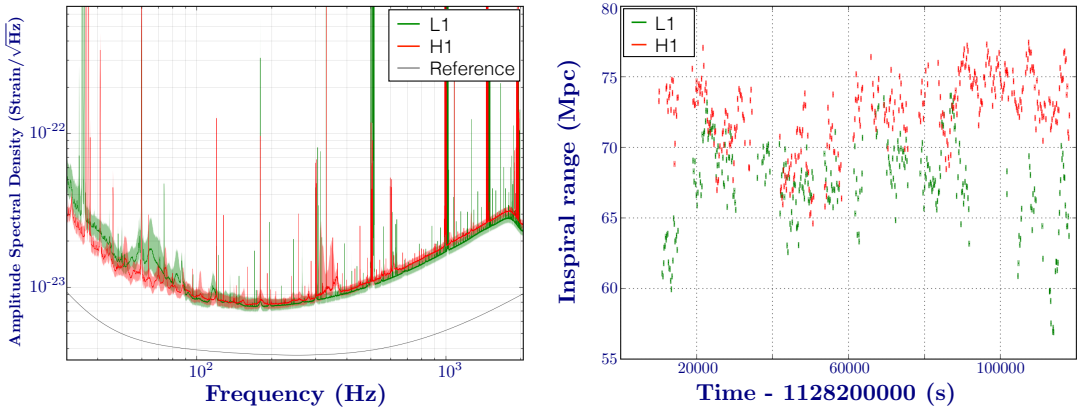


Figure 2.2: (Left) Amplitude spectral density as a function of frequency for the Hanford (H1) and Livingston (L1) detectors. The grey line labelled as “Reference” is the design sensitivity for the Advanced LIGO detectors. (Right) Inspiral range as a function of time for a binary neutron star with  $m_1 = m_2 = 1.4M_\odot$  at a single detector SNR  $\rho = 8$ .

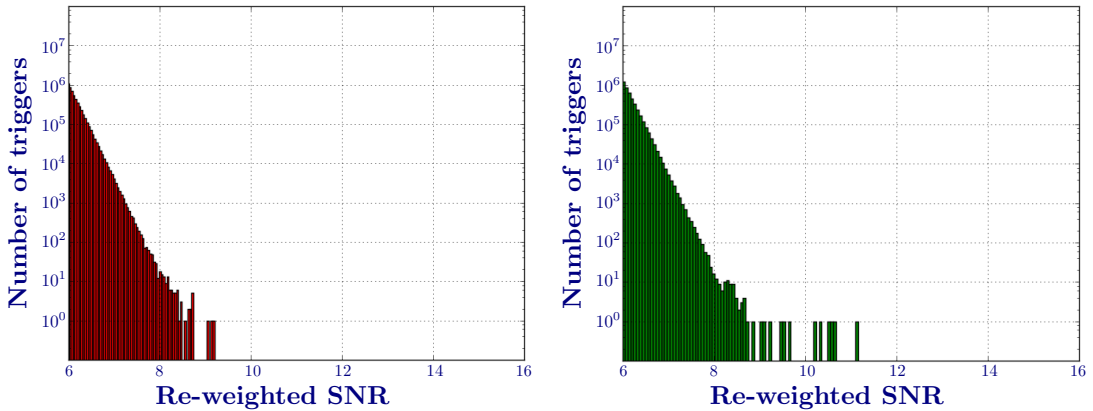


Figure 2.3: Histograms of the re-weighted SNR of the background events for the Hanford detector (left) and the Livingston detector (right). The ‘tail’ of louder background triggers is mainly due to blip glitches, which we will discuss in the next chapter.

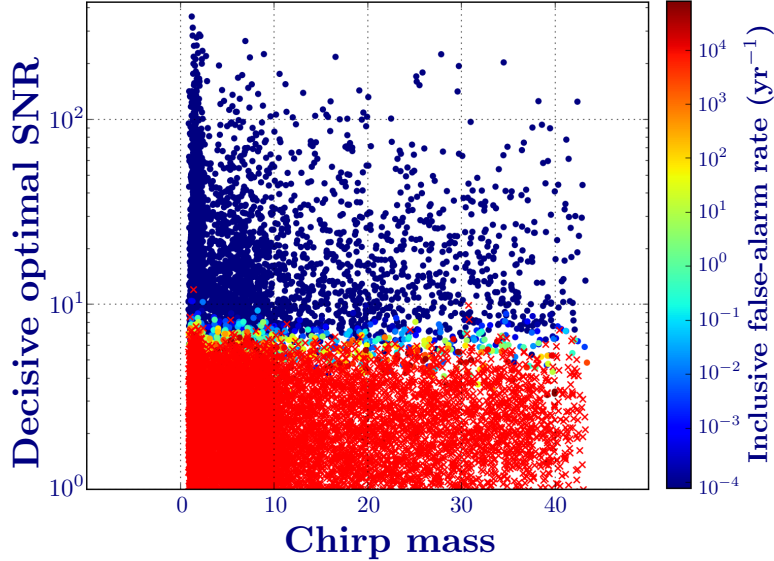


Figure 2.4: Missed (red crosses) and found (coloured circles) injections. The colour indicates the false-alarm rate estimated for the injections using the background estimated including the injection itself. The  $x$ -axis is the chirp mass defined in Eq. (1.10). The optimal SNR is a measure of the SNR of the waveform assuming no noise is present, i.e. the SNR of the waveform template with itself. The  $y$ -axis shows the decisive optimal SNR, which is the expected SNR in the second most sensitive instrument to that particular source.

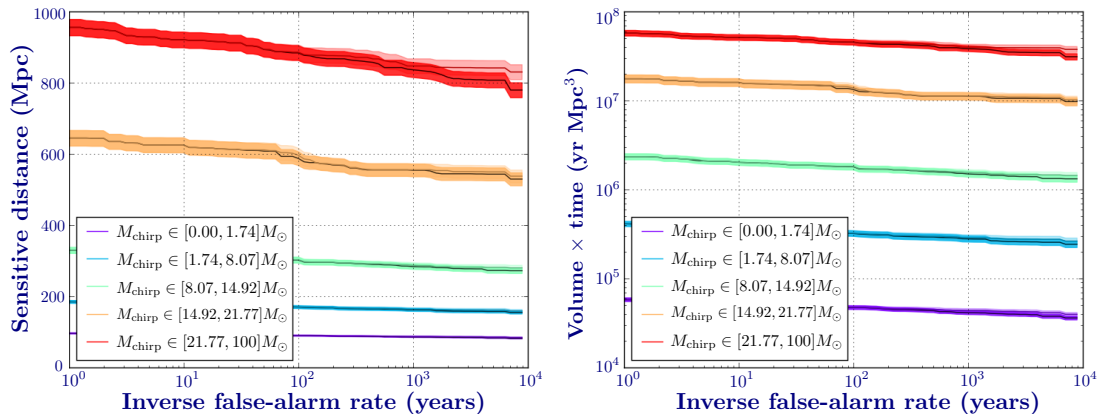


Figure 2.5: Sensitive distance (left) and sensitive volume  $\times$  time (right) of the PyCBC search as functions of the inverse false-alarm rate for each chirp-mass bin. The sensitivity is estimated from the missed and found injections added to the data. Darker lines represent the significance without including injections in their own background, while lighter lines include each injection individually in the background estimation for that signal.

identify as signals) and their false-alarm rate, as can be seen in Fig. 2.4. This serves as a useful diagnostic check: missed injections with a large SNR can be indicative of a noise transient, a gating artefact, or a problem with the analysis configuration, for instance (we will discuss in Sec. 2.4.3 all possible causes of missed injections). The analysis leader follows up the loudest missed injections to ensure there is not a problem with the configuration or to identify the corresponding noise transient.

Figure 2.5 shows final results for the sensitivity measured by the search. To account for the amount of time removed by data quality vetoes, the sensitive volume times the analysis time is also shown. Because the gravitational-wave amplitude scales with the chirp mass (given in Eq. (1.10)) the injections are grouped in chirp-mass bins and the sensitivity is computed for each bin. The summary page contains the sensitivity for all mass bins, and sensitivities for each type of system separately are found under ‘‘Search sensitivity’’.

After the initial diagnosis from the summary page, the analysis leader proceeds to investigate single detector noise triggers and missed injections in the corresponding sections. The individual follow up could indicate the necessity of a re-analysis. Therefore, this procedure takes place before open box results are made available.

#### 2.4.2 Single triggers

The follow up of the loudest background triggers from each detector is under ‘‘Single triggers’’. If noise transients of known origin are identified, new data quality vetoes are developed and incorporated to the analysis. The open box results are not made available until all data quality investigations, and therefore all necessary re-analyses of the data, are concluded. Figure 2.6 is an example of the information displayed in this section. Each individual point represents a trigger from the single detector analysis, and the colours indicate the density of triggers in a specific region. Continuous black lines

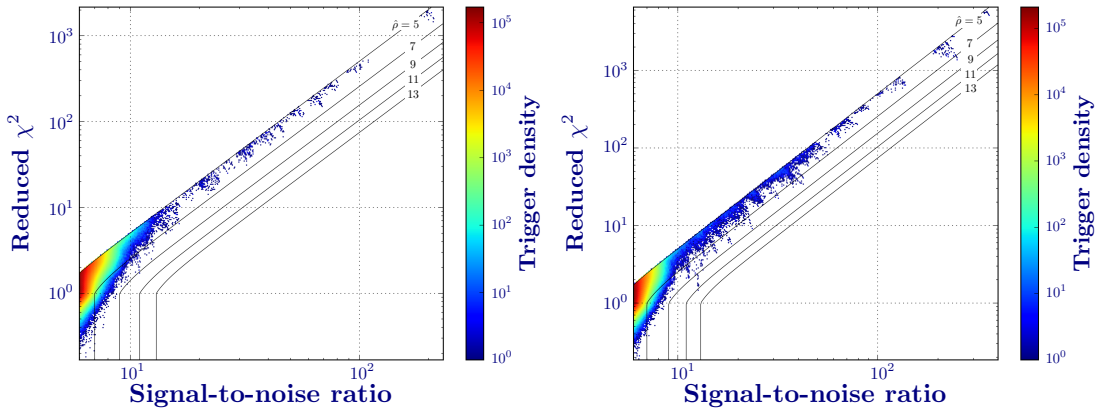


Figure 2.6: Distribution of SNR and reduced  $\chi^2$  for single detector triggers at the Hanford detector (*left*) and the Livingston detector (*right*). Continuous black lines are contours of constant re-weighted SNR. Colours indicate the density of triggers, which is usually higher at lower SNR values.

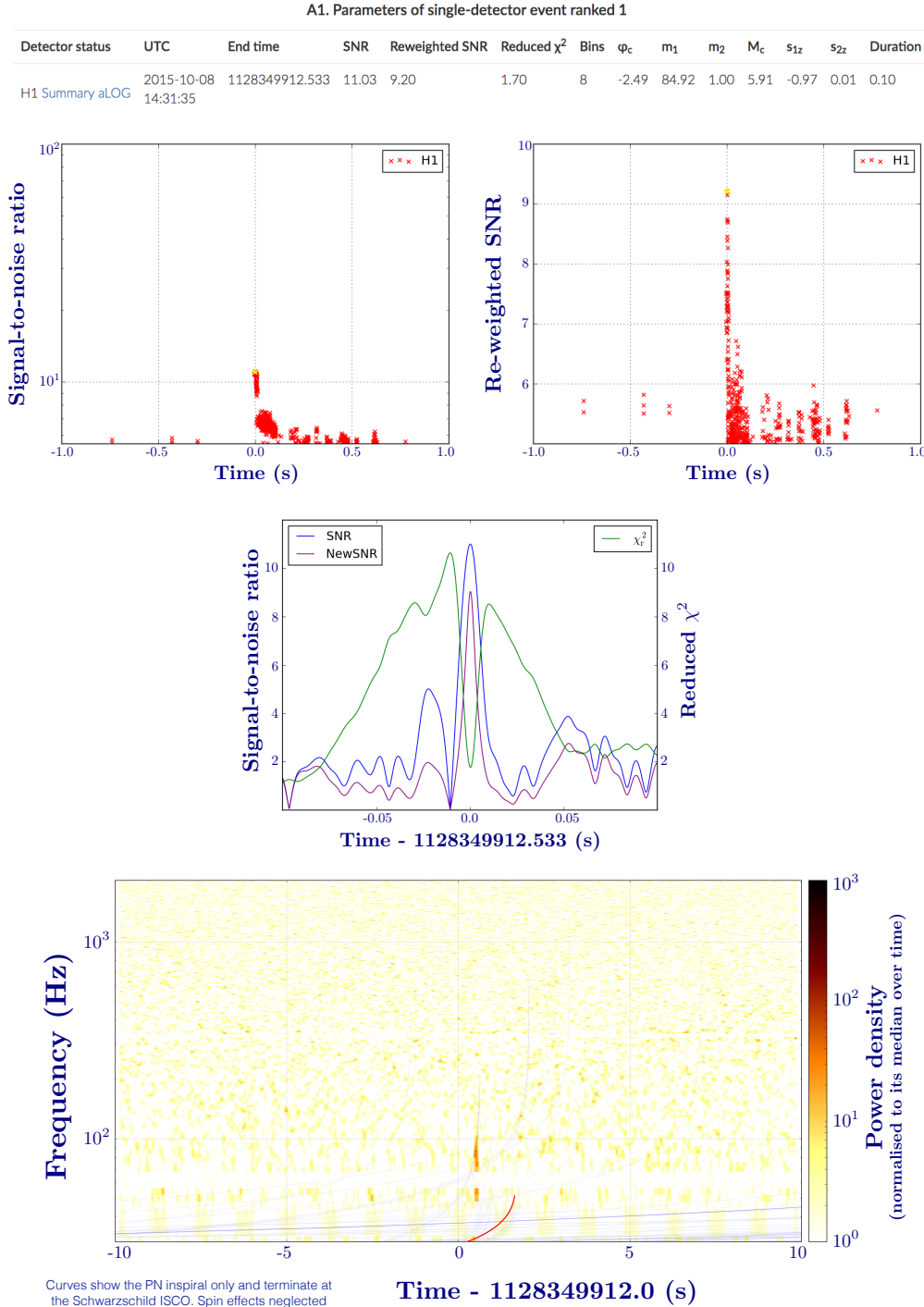


Figure 2.7: Information displayed for loudest triggers followup. (Top) Time of the trigger, ranking statistic, template associated with the trigger. (Second row) SNR and re-weighted SNR of all triggers around the time of the maxima. (Third row)  $\chi^2$  distribution and effect on SNR. (Bottom) Power spectrogram of the strain data. Curves are the loudest triggers, with the maximum shown by the red curve.

are contours of constant re-weighted SNR: here, one can see the correlation between SNR and re-weighted SNR of background triggers through the reduced  $\chi^2$ . Glitches that survive the  $\chi^2$  test usually appear as clouds of triggers that stick out from the rest of the background, reaching higher re-weighted SNR values.

In O1, the ten background triggers with loudest re-weighted SNR in each detector were displayed individually for follow up. The number of background triggers to follow up was increased to 40 in O2, organised based on the template duration. As an example of the information displayed for each trigger, Fig. 2.7 shows the loudest background trigger in the Hanford detector for the analysis presented in this section. First, the time of the trigger, the ranking statistic, and the parameters of the template associated with the trigger are shown. The duration of the template is an initial indication of the possible type of noise transient. The SNR and re-weighted SNR time-series of this particular background trigger show that the glitch is well above the background distribution. Furthermore, the narrow peak indicates that this trigger is due to a very short glitch. The reduced  $\chi^2$  time-series shows a behaviour typical of a real signal. The glitch is therefore able to survive the  $\chi^2$  test. All these clues point towards a blip glitch, and the power spectrogram shows a time-frequency shape consistent with this type of glitch.

Further examination of an individual trigger requires a time-frequency Q-scan (see Appendix A). The Q-scan of the Hanford loudest trigger in this analysis is shown in Fig. 2.8. As suspected, this particular trigger originates from a blip glitch. The origin of blip glitches is currently unknown, so they cannot be safely vetoed from the analysis. However, if the glitches are from known origin, triggers can be removed in the re-analysis.

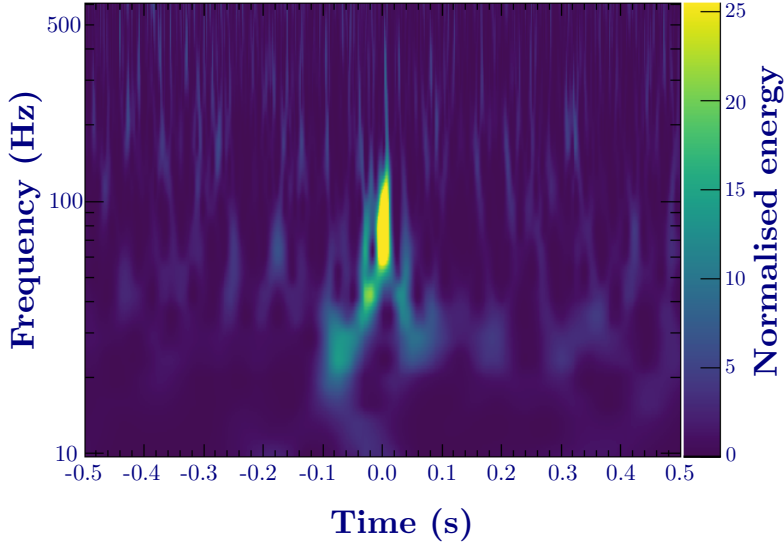


Figure 2.8: Time-frequency representation of the loudest trigger at the Hanford detector for this particular analysis. This noise transient is a blip glitch that cannot be vetoed from the search.

The analysis leader and members from the Detector Characterisation group are in close contact during the follow up process. If they identify the origin of the noise transients, corresponding times are flagged as “problematic”. The analysis is repeated and these times are vetoed before the coincidence test. Earthquakes or thunderstorms at the LIGO Livingston site are examples of situations that generate veto-able background triggers. In these cases, several noise triggers originate from the same period of time (minutes to hours). If the type of noise cannot immediately be identified from the Q-scan, the DetChar summary pages (see Appendix A) provide more information. More examples of identified and vetoed noise transients can be found in [69][70].

### 2.4.3 Injections

The follow up of the loudest missed injections, i.e. injections not identified as such by the search, is under “Injections”. There are several reasons why an injection could be missed by the search:

- An issue with the search pipeline. This happened mainly at the beginning of O1. For instance, a coding error with the optimised clustering algorithm caused some missed injections in the first runs, unexplainable by nearby glitches. The pipeline had been newly developed for the second generation of gravitational-wave detectors. The first searches with real data helped identify and solve code issues.
- A glitch occurred near the injection. Loud glitches corrupt the SNR and  $\chi^2$  time-series for a time much longer than the duration of the peak, which prevents the search from finding any SNR peaks associated with nearby injections. At the beginning of an observing run, different search tunings are tested. For instance, the size of the clustering window was reduced at the beginning of O1. With this reduction, the search could better identify an injection if the glitch was not right next to its coalescence time.
- The injection is near the beginning or the end of a lock<sup>4</sup>. The high-pass filtering and re-sampling performed by the search corrupt data at the beginning and end of a segment. Therefore, the search discards eight seconds of data near a lock transition. Injections within or near those eight seconds are missed by the search.
- The injection’s SNR is below the search threshold. Injections are ranked by optimal SNR. However, the search SNR is not necessarily equal to the optimal SNR. The noise realisation around the time of the injection can cause an injection’s SNR to drop below the search threshold.
- The spins of the individual objects are not aligned with the orbital angular momentum, i.e. the injection represents a precessing system. The template bank only includes waveforms with aligned spins. During O2, a subset of injections was

---

<sup>4</sup>Interferometric gravitational-wave detectors are enhanced by several resonant cavities. We say the interferometer is locked when all of these cavities are held on resonance [75][76].

performed with precessing spins. The search cannot recover these injections when the precession significantly modifies the waveform’s shape.

- The injection has a total mass above or a duration below the bank’s limit. During O2, a subset of injections was performed with  $M > 500M_{\odot}$  and with durations less than 150 ms. The search could not recover these injections.
- The injection is auto-gated by the search. High-mass injections are very short and easily confused with glitches. Excessively loud, high-mass injections are auto-gated by the search. We do not expect such loud, short signals in nature, therefore the auto-gating is not a hazard for real high-mass signals.

Identifying the cause of a missed injection is usually straight-forward. The most common cause for a missed injection is that its SNR is below threshold. In some cases, such as glitches or proximity to a lock, further investigations are required.

Missed injections are grouped by type of system and waveform model. For each group, the ten loudest missed injections are displayed in the results pages. In O1 the analysis leader had to follow up 60 injections. In O2, with the increase of the template bank and therefore the parameter space of the injections, 120 injections were displayed for followup. The information for each injection is similar to that of the single detector triggers shown in Fig. 2.7. Most of the causes described above can be inferred from the results pages. For instance, a gated injection would be indicated by a green shaded region in the power spectrogram. Other causes require further investigations. To establish times of beginning and end of locks, for instance, the DetChar summary pages (see Appendix A) need to be consulted.

The analysis presented in this chapter was the third analysis in the first observing run of Advanced LIGO. The PyCBC pipeline was being tuned to optimise the performance of the search. In this analysis we observed that the amount of found injections, and therefore the sensitivity of the search, was increased by reducing the trigger clustering window to one second. The previously used 4-second window would cause to miss injections in favour of nearby glitches, i.e. louder SNR peaks within the same time window. Furthermore, investigations on a missed injection in this analysis revealed an issue with the PyCBC auto-gating. After the data analysts are satisfied with the tunings chosen, code issues have been fixed, and data quality investigations are completed, the data analysis leader and the DetChar group sign off the review of the closed box results. Final open box results are shared when both agree that all possible data cleaning and analysis checks are complete.

## 2.5 Open box results

When the closed box results review is signed off, open box results are made available. The process called ‘opening the box’ consists of changing the viewing permissions of the final results. In this section we show open box results of two of the analyses led by the author during the two observing runs of Advanced LIGO.

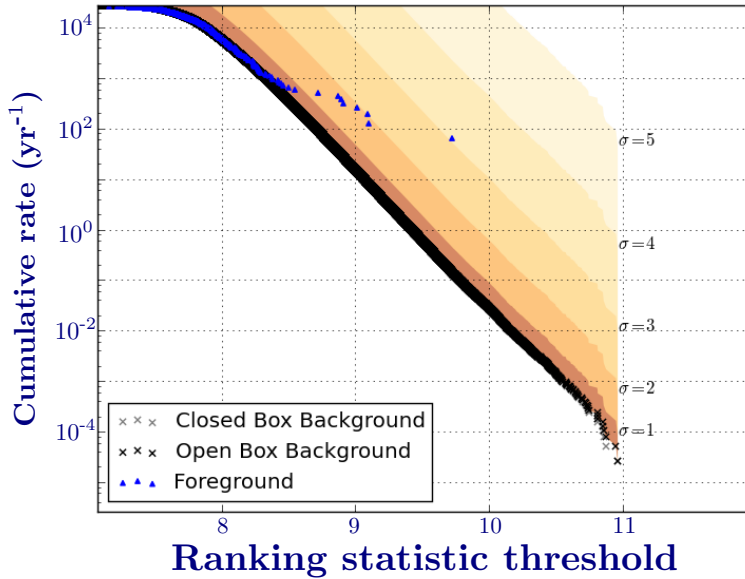


Figure 2.9: Open box results from the O2 analysis containing the binary black hole candidate LVT151012. The open (closed) box background is the background distribution estimated with (without) the foreground events. Each point is plotted at the statistic value of each trigger, and represents the total rate of triggers per analysis time with a ranking statistic at or above the  $x$ -axis value. The false-alarm rate of a foreground event is the rate of background events, so it can be read from the  $y$ -axis value of the background events at the same ranking statistic as the foreground event. The shading, only applicable to the loudest foreground event, is the significance that a single candidate event would have at that statistic value. The candidate event LVT151012 is the foreground trigger furthest to the right in this plot, with a significance of  $\simeq 3\sigma$ .

### 2.5.1 LVT151012

LVT151012 was contained in the O1 analysis for which we have shown a selection of closed box results in the previous section. The PyCBC search reported a combined SNR of 9.7 for this candidate event, recorded in the data on the 12th of October 2015 at 09:54:43 UTC. Due to its low SNR, this event was not found by low-latency burst searches. At the time, the low-latency modelled searches were not targeting high-mass systems and were not sensitive to LVT151012. Therefore, the closed box analysis was performed without knowing about the existence of an interesting candidate event.

The box was opened on the 2nd of November 2015, revealing the existence of a marginally significant candidate event with a false-alarm rate of 1 in 2.3 years. This estimate already includes the trials factor from the three search classes mentioned at the beginning of this chapter. Figure 2.9 shows the open box results for the search class containing LVT151012. This event was found with a template with component masses  $32.06M_{\odot}$  and  $14.61M_{\odot}$ <sup>5</sup>. Follow-up parameter estimation determined the best fit parameters reported in [51, 77], mentioned in Chap. 1.

<sup>5</sup>These values differ slightly from those in [67], where the search was performed over approximately 16 days of coincident data.

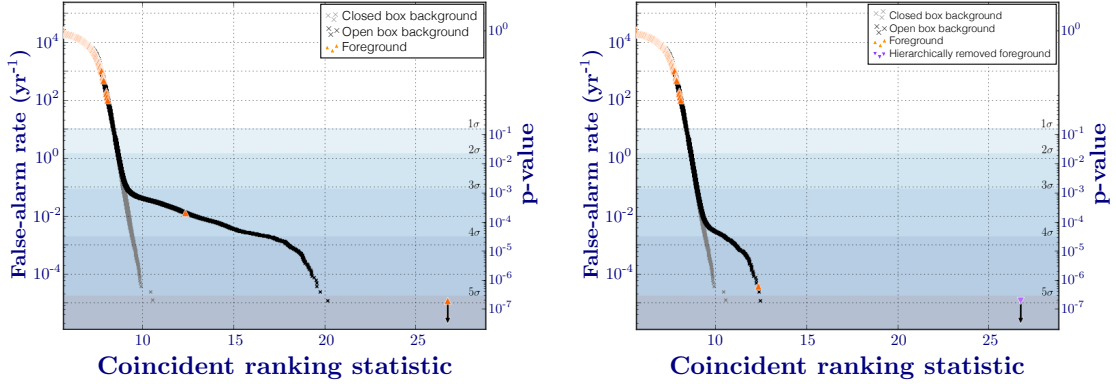


Figure 2.10: Open box results from the O2 analysis containing the binary black hole GW170814 and the binary neutron star GW170817. The closed box background is the background distribution estimated without the foreground events, as it appears in the closed box results. The open box background includes (left) all foreground events, and (right) all except the loudest foreground events, to estimate the significance of the second loudest candidate. The  $y$ -axis shows the false-alarm rate or the p-value of foreground triggers with a ranking statistic at the  $x$ -axis value.

### 2.5.2 GW170814 and GW170817

GW170814 [54] and GW170817 [55] were both contained in the O2 analysis from the 13th to the 21st of August 2017. This period included approximately 5.9 days of coincident data. Both candidate events had been found in the low-latency searches and were believed to be real signals. The box was opened on the 5th of September 2017, confirming that both candidates were highly significant. Figure 2.10 shows the open box results containing both events.

The binary neutron star GW170817 was the loudest signal in this period, with a detection ranking statistic of 26.7. Exceptional measures had to be taken for the offline analysis because of a glitch occurring in the Livingston detector shortly before the coalescence time of the binary neutron star [55]. Noise transients similar to this glitch are automatically identified roughly every few hours in the LIGO detectors and flagged as CAT2 vetoes. Therefore, triggers originating around the time of this event would have been removed after the single-detector analysis. Instead, the veto flag for this type of glitch was turned off, and the times of occurrences were given to the search pipeline through a gating file. With the glitch gated from the search, the pipeline could identify the triggers from the astrophysical signal. For the binary neutron star event, the search reported the minimum false-alarm rate given by the background time. This is interpreted as a lower bound on the false-alarm rate of the signal. Therefore, GW170817 had a false-alarm rate of less than 1 in 81,000 years. This event was found with a template with component masses  $1.46M_{\odot}$  and  $1.3M_{\odot}$ . Follow-up parameter estimation determined the best fit parameters reported in [55], mentioned in Chap. 1.

The binary black hole GW170814 was the second loudest signal in this analysis, with a detection ranking statistic of 12.4. To estimate the false-alarm rate of this signal

against the background, the louder signal was removed from the background estimation. The resulting background can be seen in the right panel of Fig. 2.10. For this event, the search reported a false-alarm rate of approximately 1 in 27,000 years. This event was found with a template with component masses  $48.67M_{\odot}$  and  $19.6M_{\odot}$ . Follow-up parameter estimation determined the best fit parameters reported in [54], mentioned in Chap. I.

## 2.6 Conclusions

This chapter laid out the main ingredients of the PyCBC search pipeline. We explained first how trigger events are identified in a single detector, followed by the coincident ranking statistics and significance estimation necessary to identify astrophysical gravitational-wave signals. After describing the functioning of the pipeline, we reported on the offline search procedure. Result examples from the offline searches included the candidate event LVT151012 and the gravitational-wave signals GW170814 and GW170817.

The second generation of gravitational-wave detectors has just begun. Upgrades are currently ongoing to improve the sensitivity on the detector side. The PyCBC search is fully capable of identifying astrophysical signals. However, this search is also undergoing improvements and developments. For instance, the capacity to fully incorporate a third detector is being developed for the next observing run of Advanced LIGO, when Virgo is likely to be fully operational as well.



# Chapter 3

## Identifying short noise transients in Advanced LIGO data

The basic design of the Advanced LIGO gravitational-wave detectors [48,75] is a Michelson interferometer with Fabry-Pérot resonant cavities in each of the 4-km long arms. A simplified sketch of the optical configuration of an Advanced LIGO interferometer is shown in Fig. 3.1. The input mode cleaner stabilises the laser frequency and suppresses higher order spatial modes before the light enters the interferometer [78]. Between the input mode cleaner and the beam splitter, the power recycling mirror is placed to increase the effective laser power. After the beam splitter, the input and end test masses form the Fabry-Pérot arms. These test masses are suspended by quadruple pendulum systems, mounted to actively stabilised in-vacuum optical tables, that provide seismic isolation from the environment. At the anti-symmetric output of the Michelson, the signal recycling mirror is used to maintain a broad frequency response of the detector. Finally, the output mode cleaner [79] filters out higher order spatial modes produced in the interferometer before the light enters the readout photodiodes. The signal measured by the photodetectors is digitised and calibrated to convert laser light power to mirror displacement [80]. This calibrated strain,  $s(t)$ <sup>1</sup>, is the data analysed by the search pipelines.

The noise floor of Advanced LIGO is mainly limited by the fundamental noise sources [48]. Technical noise sources, which are controllable by design, shape the detector's strain sensitivity. Several major upgrades were implemented between the Initial and Advanced LIGO generations to reduce these noise sources and improve the detectors' sensitivities. For instance, the signal recycling cavity and the new quadruple pendulum suspension mentioned above were first introduced in the Advanced LIGO era. Moreover, different materials were used in the suspensions and new test masses were built to reduce thermal noise. During the first observing run of Advanced LIGO, the detectors' strain noise was already between 4 and 30 times better than in the last observing run of Initial LIGO, depending on the frequency band [75]. Further improvements will be

<sup>1</sup>In the literature, the calibrated strain is usually referred to as  $h(t)$ . In this chapter, however, we use  $s(t)$  for consistency with the other chapters, where  $h(t)$  was used for gravitational waveforms.

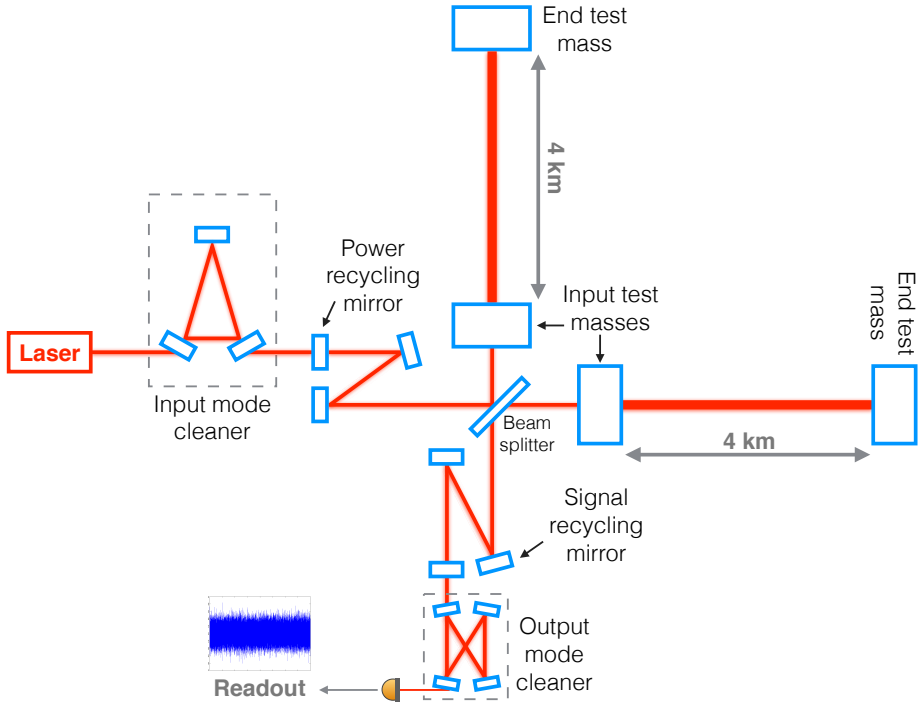


Figure 3.1: Simplified optical configuration of the Advanced LIGO detectors.

implemented in the coming years until Advanced LIGO’s design sensitivity is reached, such as the gradual increase of the laser power to reduce quantum noise.

Technical, or hardware, and environmental noise sources can produce non-Gaussian noise transients in the LIGO data. These ‘glitches’ are not rare in the data and can affect the sensitivity of the search pipelines. One of the main goals of the Detector Characterisation group is to study the characteristics of background noise events and to identify sources of glitches. Gravitational-wave detectors however are very intricate machines; identifying the source of a glitch can be very challenging. In addition to the main gravitational-wave channel, there are over 200,000 auxiliary channels in each detector. These channels monitor the environmental conditions and hardware behaviour at the interferometer [81]. Should a source for a certain type of glitch be identified, either the detector issue can be fixed at the source and such glitches disappear, or otherwise auxiliary channels can be used to identify times of occurrences and remove or veto the glitches in the search pipelines [69], as described in the previous chapter.

Many types of glitches observed in LIGO data are still of unknown origin and cannot be solved or safely vetoed. Here we focus on the yet unsolved type of short noise transients commonly known as ‘blip glitches’. As we saw in the previous chapter, blip glitches populate the background measured by the transient search pipelines, affecting the performance of the matched-filtering techniques. This chapter is organised as follows. Section 3.1 describes the morphology and characteristics of a blip glitch. In Sec. 3.2 we develop a method to identify times of blip glitches using PyCBC tools. With the blip

glitches identified by this method, we (i) explore the effect of removing blip glitches from the data in the PyCBC searches in Sec. 3.3, and (ii) perform investigations to identify the origin of blip glitches in Sec. 3.4. Finally, the chapter is summarised in Sec. 3.5. Except for the findings in Sec. 3.4.1, all the work presented in this chapter was performed by the author. Andrew Lundgren provided important discussions for remote investigations, Alex Nitz guided the author on the development of the low-latency blip-glitch finder for the second observing run, and the findings in Sec. 3.4.2 occurred together with Tom Dent. Mike Landry, Evan Goetz, Sheila Dwyer, Jenne Driggers, Jeff Kissel, Evan Hall and Dave Barker provided helpful advice and comments in the two occasions that the author visited the LIGO Hanford site.

### 3.1 Description of a blip glitch

A glitch is categorised as a blip glitch if it is a very short duration transient, no more than 100 ms, and has a large frequency bandwidth, from a few tens to a few hundreds Hz. A time-frequency Q-scan (see Appendix A) of a typical blip glitch is shown in Fig. 3.2. This type of glitch was first observed in Initial LIGO, and has persisted on into the Advanced LIGO generation. The absence of methods to identify blip glitches, and the fact that they do not show correlation between any auxiliary channels and the gravitational-wave channel, make it difficult to obtain meaningful statistics and to establish their origin.

Blip glitches are amongst the most harmful types of glitches triggering bursts and matched-filtering searches. High mass compact binaries with large mass ratio and anti-aligned spins have a gravitational-wave imprint similar to the characteristic time-domain shape of a blip glitch, as can be seen in Fig. 3.3. The  $\chi^2$  consistency test described in the previous chapter are not sufficient to reject all blip glitches and they populate the tail of the background distribution. Blip glitches are found in both LIGO detectors, although occurrences are independent between the interferometers. Therefore, blip glitches usually

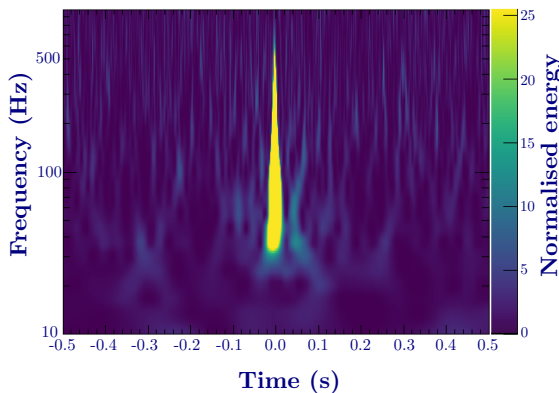


Figure 3.2: Time-frequency representation of a typical blip glitch, seen in Hanford data on August 21st 2017.

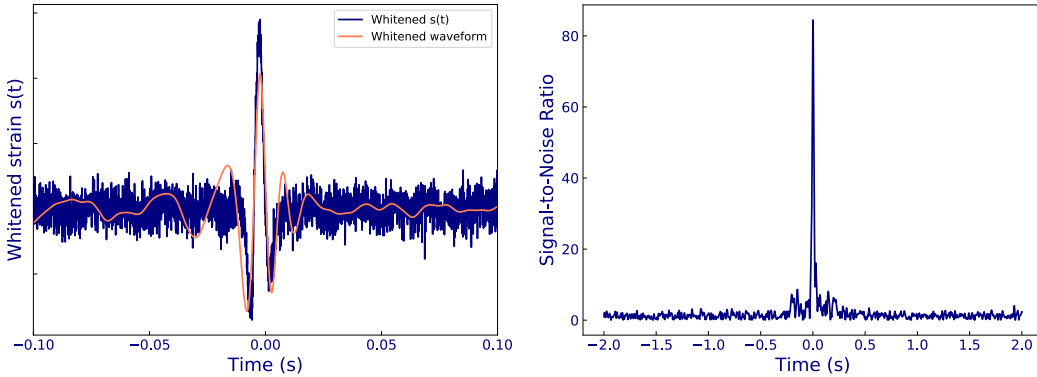


Figure 3.3: (Left) Whitened  $s(t)$  strain at the time of a blip glitch with a whitened compact binary waveform overlaid on top of it. The waveform corresponds to a system with a high total mass ( $M_t = 95.7M_\odot$ ) and a high mass ratio ( $q = m_1/m_2 \simeq 22$ ). (Right) Signal-to-noise ratio obtained by matched filtering the template and the data shown on the left plot.

do not survive the coincidence test described in Sec. 2.2. However, the high rate of blip glitches affects the sensitivity of the search pipelines by populating the search background and causing missed injections.

### 3.2 Finding blip glitches

During the first observing run of Advanced LIGO (O1), blip glitches always triggered the same waveform templates in the PyCBC offline searches described in the previous chapter. This suggested that one could use those templates together with PyCBC search techniques to find occurrences of blip glitches in the data. We constructed a reduced template bank using only 14 templates instead of the 250,000 used for gravitational-wave searches [67]. With this template bank, we performed the PyCBC matched filtering on single detector data for the entire O1 data set.

The blip search required a slightly different tuning than that of the gravitational-wave search. It was observed during the course of the run that most of the PyCBC background triggers with signal-to-noise ratio (SNR)  $\rho \simeq 5 - 7$  were due to random fluctuations of Gaussian data. Furthermore, triggers with SNR  $\rho > 150 - 200$  typically originated from very loud glitches that were not blips. Therefore, we used a threshold of  $7.5 \leq \rho \leq 150$  to optimise our blip-glitch finder. After the single detector matched filtering, we clustered triggers in time to identify individual glitches and manually removed glitches that did not match our definition of a blip glitch. The top row of Fig. 3.4 shows histograms with the resulting lists of blip glitches in each LIGO detector for the entirety of O1. The Hanford detector showed a higher rate of blip glitches per analysed time, especially in December and January. A total of 4009 blips was found in approximately 77 days of analysed Hanford data versus the 2138 found in about 67 days of analysed Livingston data.

During the second observing run of Advanced LIGO (O2), we created a low latency

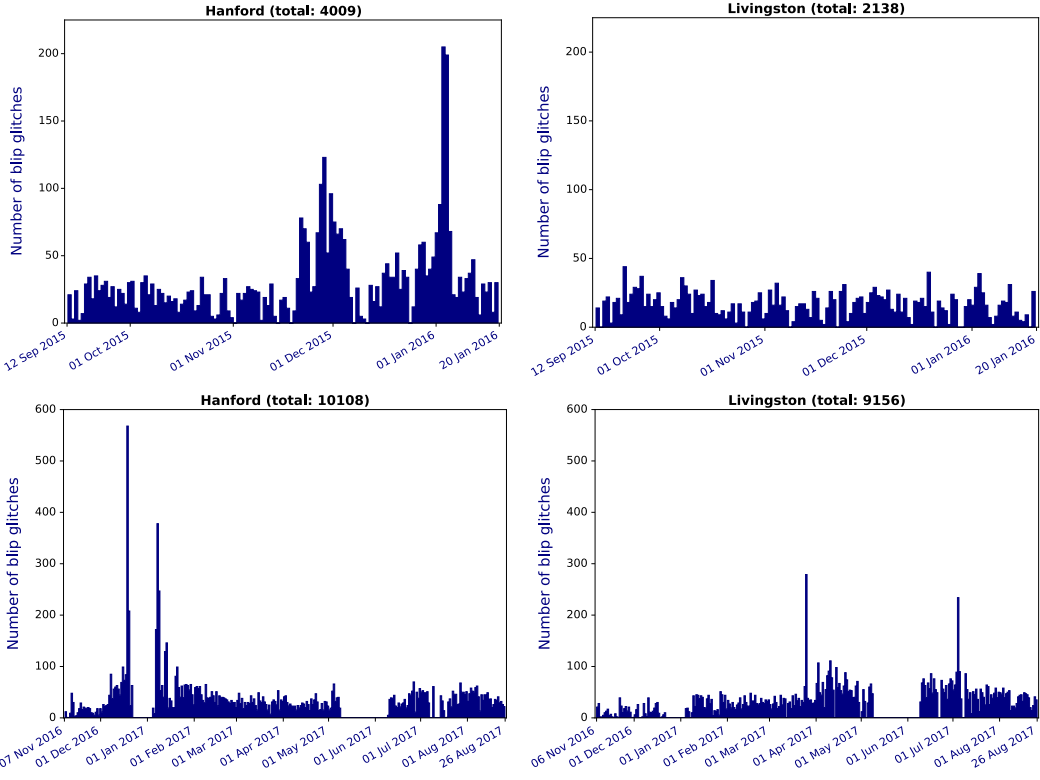


Figure 3.4: Blip glitches found using PyCBC tools during (*top row*) the four months of the first observing run (O1), and (*bottom row*) the ten months of the second observing run of Advanced LIGO (O2). The left column is the Hanford observatory and the right column is the Livingston observatory.

blip-glitch finder using the newly developed PyCBC Live (see Appendix A). The O2 template bank for compact binary searches had increased in total mass [68], and therefore a few more templates were identified as potential blip-glitch finders. With a reduced template bank of 30 templates, we started a low-latency PyCBC Live search optimised to find blip glitches rather than gravitational waves. We initiated the blip glitch summary pages using the same format as the detector summary pages developed by the Detector Characterisation group (see Appendix A). These pages were updated every five minutes but listed only the daily ten loudest glitches. Therefore, we generated daily lists with all the times of blip glitches. Both of these tools were designed to enable rapid investigations at the detector sites during the course of the run. At the end of the run, we applied the offline data-quality vetoes to our lists to remove glitches of known cause, and manually removed glitches that did not match our definition of a blip glitch. The bottom row of Fig. 3.4 shows histograms with the resulting lists of blip glitches in each LIGO detector for the entirety of O2. Again, the Hanford detector showed a slightly higher rate of blip glitches, with a total of 10108 blips in approximately 161 days of analysed data versus the 9156 found in about 155 days of Livingston data.

It is worth mentioning that, during the course of this work, a new citizen science project called Gravity Spy was created [82]. This project combines crowdsourcing with machine learning to categorise all types of glitches found in LIGO data. The first beta version was launched in April 2016, and the full Gravity Spy project on October 2016. This took place after we already had obtained lists of blip glitches for O1, and when we were already preparing the low-latency blip-glitch hunter for O2. Therefore, the investigations performed within the scope of this work only used the lists described in this section. However, Gravity Spy has a great potential for automatically obtaining faithful lists of blip glitches, and we do not discard using its results in forthcoming runs.

### 3.3 Effect of blip glitches on PyCBC searches

Having found an extensive number of blip glitches in the data, one can tentatively show the effect of blip transients on compact binary searches with PyCBC. For this purpose, we remove blip glitches from the analysed data using the gating technique described in the previous chapter (Sec. 2.1). It is important to note that the method we use here is not applicable for real gravitational-wave searches, because the blip glitches were found by means of the main calibrated gravitational-wave channel. Since the calibrated  $s(t)$  cannot distinguish between noise transients or real signals (especially for the case of blip glitches, where the similarity to real signals can be astonishing), noise transients have to be vetoed using auxiliary channels. Here, we use these lists only to show how blip glitches affect the sensitivity of compact binary searches, as a motivation to find sources of blip glitches and reduce their impact on the data.

We chose to analyse a stretch of O2 data that had the highest density of blip glitches: January 4th to January 22nd 2017. During that period, we recorded 1555 blip glitches in Hanford and 500 in Livingston. The blip glitches to be gated were passed to the PyCBC pipeline through a gating file. The original run only used the auto-gating performed by PyCBC, as described in the previous chapter (Sec. 2.1), while our run without blip glitches used both auto-gating and the gating file. The difference in the amount of gated time between both runs is approximately 51.7 minutes in Hanford and 16.3 minutes in Livingston. As a visualisation of the amount of background triggers removed, Fig. 3.5 shows the background distribution of the single detector triggers from the original analysis (left column) and from the re-analysis without blip glitches (right column). Continuous black lines show contours of constant re-weighted SNR (defined in Eq. (2.7)). Each dot is an individual trigger, and the colours indicate the density of triggers. The high density of triggers at low SNR originates from random fluctuations of Gaussian noise. Triggers at larger SNR values are typically due to noise transients. Blip glitches often have significant re-weighted SNR and appear as clouds of triggers sticking out from the background. By comparison between the left and right columns in the figure, one can see that the amount of triggers sticking out is considerably reduced in the re-analysis without blip glitches. Furthermore, the amount of individual triggers with  $\rho > 20$  is noticeably lower in the Livingston re-analysis.

The resulting change in sensitivity is shown in Fig. 3.6, where the left column corres-

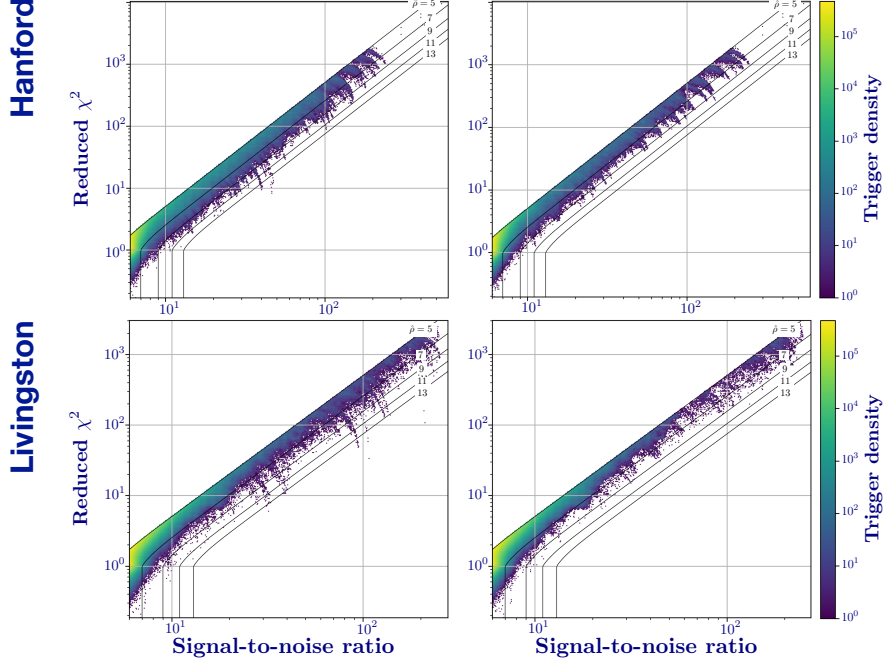


Figure 3.5: SNR vs reduced  $\chi^2$  of single detector triggers in the PyCBC offline search before (left) and after (right) removing the blip glitches present in the data. Continuous black lines show contours of constant re-weighted SNR.

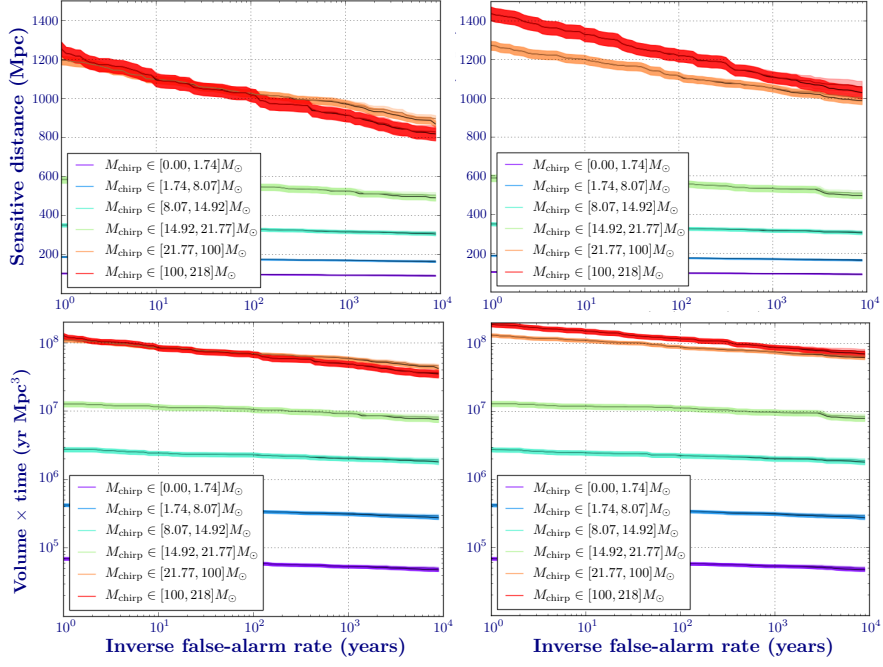


Figure 3.6: Sensitivity reported by the PyCBC offline search before (left) and after (right) removing the blip glitches present in the data. (Top row) Sensitive distance as a function of the inverse false alarm rate, divided in chirp mass bins. (Bottom row) Sensitive volume  $\times$  time as a function of the inverse false alarm rate, divided in chirp mass bins.

pounds to the original run and the right column corresponds to the re-analysis with the blip glitches removed. The top row shows the sensitivity distance. Because there was a small difference in the amount of time analysed it is sensible to show also the sensitive volume  $\times$  time (bottom row). It can be clearly seen that blip glitches do not have a significant effect on the sensitivity to longer gravitational-wave signals, i.e. lower mass templates (given in the figure in terms of the chirp mass defined in Eq. (1.10)). However, removing blip glitches significantly increased the sensitivity to shorter gravitational-wave signals, i.e. higher chirp mass templates. It is therefore crucial to solve the causes of blip glitches or identify means of vetoing such transients for searches of high mass systems.

### 3.4 Investigating the origin of blip glitches

Millisecond transients were not expected to happen a priori in gravitational-wave detectors. It is unlikely that blip glitches represent actual motion of the mirrors, because the big and heavy test-mass mirrors would not respond to such short impulses. Furthermore, the Fabry-Pérot cavities act like low-pass filters. However, the fact that blips are not coincident between detectors proves that they are of instrumental origin rather than of astrophysical origin. In addition, a quick check of the cosmic ray detector located at the Hanford site has shown that there is no unusual cosmic-ray activity at times of blip glitches [83]. Complete lists of blip glitches, like the ones obtained with the methods described in Sec. 3.2, provided, for the first time, meaningful statistics. It is possible now with these statistics to investigate the source of blip glitches and explore correlations between the rate of blip glitches and the status of the detectors. In this section we briefly explain some of the conclusions derived from investigating sources of blip glitches during the Advanced LIGO generation of detectors. As we will see, these investigations indicate that there is not one single source for all blip glitches. Instead, we found that there are different subsets of blips.

#### 3.4.1 Correlation with humidity

At the end of O1, a strong correlation between the rate of blip glitches and the outside temperature was found at the LIGO Hanford detector [84]. The outside temperature is well correlated with the inside relative humidity: during the winter, heating is required to maintain the inside temperature and the inside relative humidity decreases. As can be seen in Fig. 3.7, there was a significant increase in the rate of blip glitches during periods when the inside relative humidity dropped below 5% at the Hanford site. Even though the exact cause is still not clear, dry conditions might favour the discharge of static electricity or current leakage paths. Therefore, it might be possible that these blip glitches are due to electronic sparks, which could be fixed or reduced by maintaining the inside relative humidity above critical levels.

In [84], the population of blip glitches from times of low relative humidity was compared to the population from a relatively quiet time (marked as segments 1, 2 and 3 in Fig. 3.7, respectively). The low-humidity blip glitches (segments 1 and 2) matched well

with each other, but proved to be statistically different than those blips from the quiet time (segment 3). Therefore, “electronic” or low-humidity blip glitches are just one of probably many subsets of blip glitches.

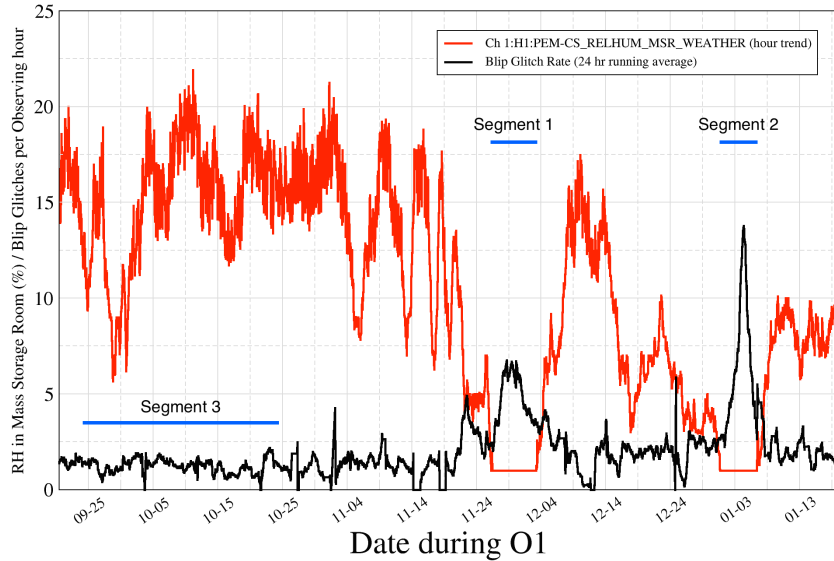


Figure 3.7: Correlation between blip glitches and low inside relative humidity at the Hanford detector (image from [84]). The  $x$ -axis shows the date in the format month-day. The  $y$ -axis shows (i) the relative humidity (RH) in one room of the detector’s corner station for the red curve, and (ii) the number of blip glitches per hour of data in observing mode for the black curve. The population of blip glitches in segments 1 (end of November) and 2 (beginning of January) could be different than that of quiet times such as segment 3 (September–October).

### 3.4.2 Laser blips

During the first half of O2, we found that a subset of blip glitches at Hanford originated from the pre-stabilised laser (PSL). These glitches showed a clear correlation between the main calibrated gravitational-wave channel and a PSL auxiliary channel. The auxiliary channel in question witnesses one of the photodiodes at the inner loop of the intensity stabilisation servo (ISS). The ISS is a feedback control system designed to stabilise the power of the PSL [85, 86].

A simplified sketch of the optical configuration of the PSL, including all stages of the ISS, is shown in Fig. 3.8. The ISS consists of three loops: the noise eater, the inner loop, and the outer loop. The noise eater is placed at the laser output to reduce the relaxation oscillation of the laser. The pre-mode cleaner (PMC) filters the laser beam at later stages, and passively suppresses power fluctuations above a specific frequency. The inner and outer loops are situated after the PMC to stabilise the power in the detection frequency band (10 Hz to 10 kHz). The inner loop measures power fluctuations through

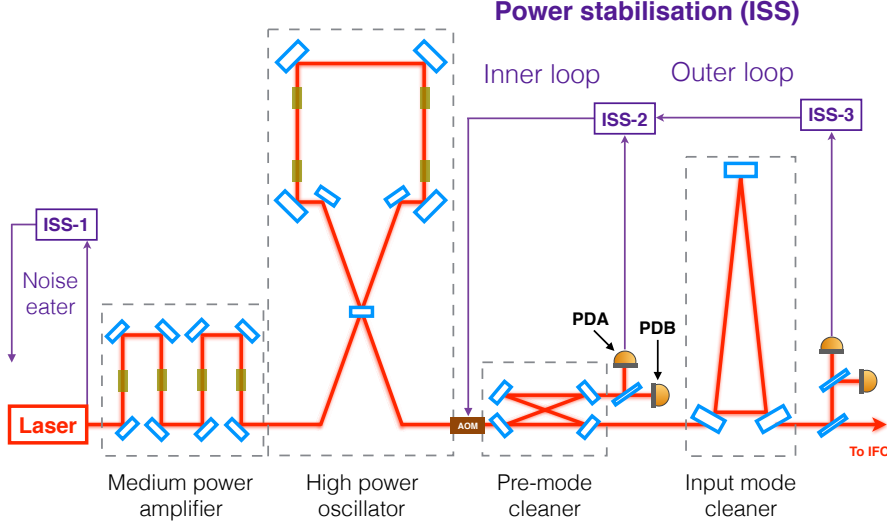


Figure 3.8: Simplified optical configuration of the pre-stabilised laser (PSL) at the Advanced LIGO detectors. The ISS is the intensity stabilisation servo designed to stabilise the power of the laser. The input-mode cleaner is not part of the PSL, but is closely related. AOM is the acousto-optic modulator used as the actuator [86].

the photodiode labelled PDA in Fig. 3.8. These fluctuations are stabilised through the feedback control loop and an acousto-optic modulator (AOM) is used as an actuator [86]. The outer loop is located after the input mode cleaner (IMC), which is not part of the PSL. This loop senses the light that enters in the interferometer and is implemented to achieve the required power stability at 10 Hz. The outer loop improves the power stability of the inner loop and compensates power noise that is not suppressed by the noise eater, PMC, inner loop or IMC.

The PSL blip glitches occurred from the beginning of the run (November 2016) until the end of February 2017. Figure 3.9 shows the trace of one PSL blip glitch throughout the detector, from the PSL auxiliary channel all the way to the main calibrated strain channel. Omicron triggers (see Appendix A) from the PSL auxiliary channel were used to incorporate data quality information into the search pipelines. With the procedures described in the previous chapter, these glitches were vetoed from the data after the matched-filtering search. The exact cause of the laser glitching remains unknown.

### 3.4.3 Computer error blips

The LIGO detectors have a very complex data transfer and acquisition architecture. Lots of subsystems and channels require real-time digital controls, and real-time analog data acquisition for analysis and archiving [48]. Interferometer signals flow between Analog-to-Digital and Digital-to-Analog Converters (ADC and DAC) through a customised computer infrastructure, located in rooms separate from the interferometer areas and connected via fibres. The Real-time Code Generator (RCG) is in charge of sub-

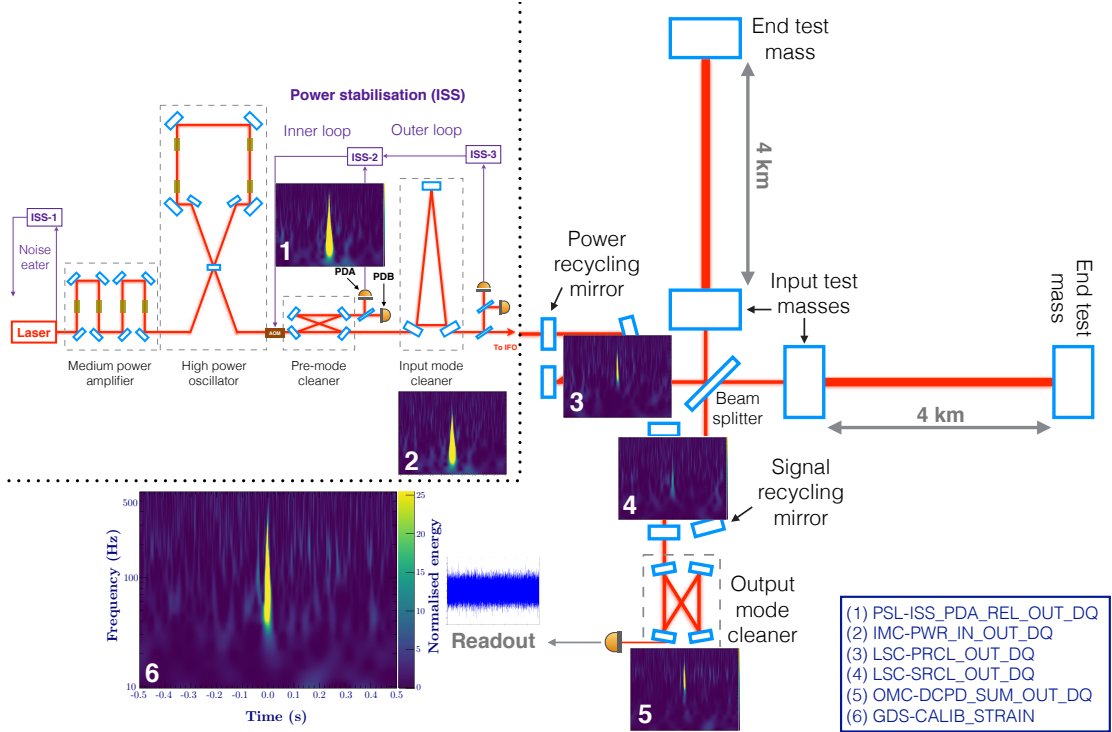


Figure 3.9: Follow up of a PSL blip glitch from the PSL auxiliary channel (1) to the main calibrated strain channel (6). Channel (2) measures the power entering (PWR.IN) the IMC from the PMC. Channels (3) and (4) are length sensing and control (LSC) channels for the power recycling cavity length (PRCL) and the signal recycling cavity length (SRCL), respectively. Channel (5) is the summation (SUM) of the four quadrants of the DC photodiode (DCPD) at the output-mode cleaner (OMC).

system data acquisition and controls the programs. Different RCG models describe the execution sequence for different code infrastructures.

Between O1 and O2, the suspension (SUS) models became too complicated for the standard front-end computers. Faster computers were installed at both LIGO sites to speed up both the SUS and the I/O Processor (IOP) models. The IOP is in charge of interfacing with the I/O hardware modules, and of synchronising with the interferometer timing system [48]. During the course of O2, we observed that there was a subset of blip glitches coincident with times of computer errors. There are several types of computer errors. We restrict ourselves here to the errors that were observed in coincidence with blip glitches during O2.

The IOP model reads the ADC signal at the beginning of each cycle and assigns it to the corresponding channel. If there is an ADC overrun error, there are two possibilities: (i) data are not arriving on time from the ADC modules, or (ii) the IOP misidentified the channels. The ADCs have channel identification, and can therefore re-synchronise themselves when the overrun error is associated to channel misidentification. In this case, the RCG discards the data from the corresponding corrupted cycle [87]. However,

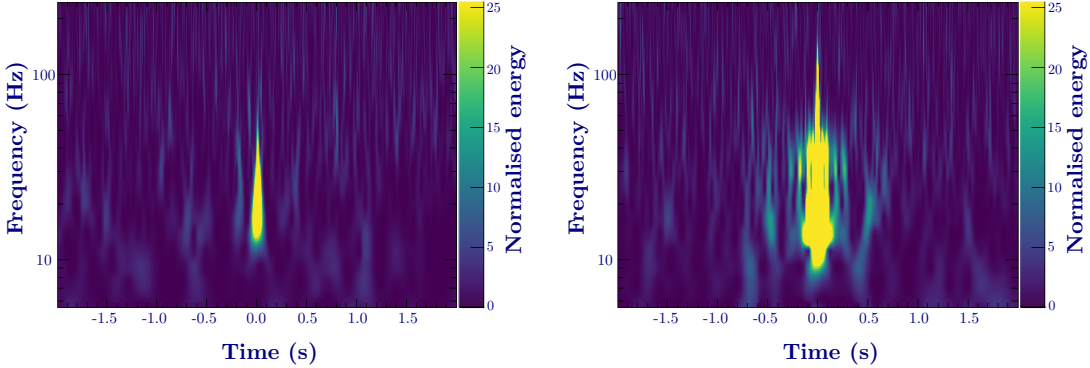


Figure 3.10: Time-frequency representation of two computer blip glitches observed during the second observing run of Advanced LIGO. The signal-to-noise ratio reported by Omicron for these glitches is (left)  $\rho \simeq 12$  and (right)  $\rho \simeq 80$ . The loudest computer glitches observed in O2 have SNR  $\rho \simeq 350$ .

if the ADC overrun is associated to a timing error, it can propagate through the inter-process communication (IPC) system to the downstream models. Furthermore, the IPC system can also experience an error on its own. Errors marked as IPC can indicate a fault in receiving IPC data via any IPC mechanism [88]. Finally, timing errors are due to code execution times greater than allowed, or times between code cycles outside of the assigned limits.

It is still uncertain how the computer errors can cause a glitch in the main calibrated strain channel. Computer errors seem to happen more frequently in Hanford than in Livingston, even though the two systems are identical. There are auxiliary channels for each model that record occurrences of computer errors. At the end of O2, we used some of these channels to find computer errors at the LIGO Hanford site. The model with the largest number of computer errors was the IOP-SUS model, with a total of 1778 errors on both end-X and end-Y models (832 and 946, respectively). The IOP-SUS is the first in the sequence from all the models we looked at. Therefore it is possible that many or all of the errors found in the downstream models propagated from the IOP-SUS model. Using HVeto (see Appendix A), we found that about 46% of the IOP-SUS front-end computer errors were in coincidence with triggers in the main calibrated  $s(t)$  strain channel, suspected to be blip glitches. Figure 3.10 shows the time-frequency representation of two computer blip glitches

### 3.5 Conclusions

In this chapter we introduced a method to identify blip glitches. During the first two observing runs of Advanced LIGO, thousands of blips were found in each LIGO detector. Blip occurrences were extracted from the data to show how the sensitivity of the PyCBC search pipeline is affected by such noise transients. Blip glitches have proven to be very harmful for searches of high-mass compact binaries. It is therefore important to identify

the origin of these noise events so they can be mitigated from the searches. Using the lists of blip glitches we obtained, we conducted several investigations. Many of those investigations resulted inconclusive. Here we presented the most interesting studies, namely the ones that identified the source of two subsets of blip glitches and provided information about a possible third subset.

Despite the importance of having identified the laser and the computer blip glitches, these were only two small subsets of the total number of blip glitches found. Search pipelines are evolving to new ranking statistics that veto some blip glitches from the searches, as we saw in the previous chapter. At the same time, investigations continue during commissioning time and will continue as well during future observing runs. Further investigations on the coupling between blip glitches and computer errors are still ongoing, even as the computer infrastructure at the LIGO sites is being upgraded. Now that binary black holes are known to exist, it becomes even more urgent to remove blip glitches from the data. Otherwise, we might never be able to distinguish between blip glitches and gravitational-wave signals from high mass systems.



# Chapter 4

## Parameter estimation of the black-hole ringdown

Search pipelines estimate the significance of a gravitational-wave signal, but are not designed to extract the parameters of the gravitational-wave source. The discrete nature of the template bank, optimised to match signals with less than a few percentage loss in signal-to-noise ratio, does not have the power to measure the properties of the signal. The triggering template in the search is the waveform that best matches the data, from the waveforms present in the template bank. However, the template with the source's parameters might not even be contained in the template bank. To obtain full information about the source it is necessary to confront the signal with a much larger set of templates covering the entire parameter space. This is the next step after the detection of a gravitational-wave signal.

Parameter estimation pipelines are designed to measure the physical parameters of the gravitational-wave source. The parameter-estimation framework for compact binary coalescences is Bayesian inference. This framework provides the posterior probability distribution of a set of unknown parameters given a specific model of the data. An extensive amount of model waveforms are correlated with the data at the time of the signal to calculate the posterior probability. The source parameters published for the astrophysical signals detected with Advanced LIGO were obtained using the LALInference pipeline [89]. The LALInference software consists of a C library and several Python post-processing tools. This pipeline utilises accurate models of compact binary waveforms describing the full inspiral-merger-ringdown dynamics [59, 60], or inspiral-only post-Newtonian waveforms [90] in the case of binary neutron stars.

In this chapter we develop a method to estimate the parameters of the remnant black hole using ringdown model waveforms. Here we use PyCBC tools and the recently developed PyCBC Inference, a new Python based inference framework. Our method is an extension of the work in [91], which was used for GW150914 in [92]. As we will see, the mass and the spin of the final Kerr black hole can be extracted from the ringdown signature of the source. This feature will be used in Chap. 6 to develop a test of the black hole area increase law. Furthermore, our ringdown model accepts an arbitrary number of quasi-normal modes. This feature can be used in the future to perform tests

of the no-hair theorem.

This chapter is organised as follows. The principles of Bayesian Inference are briefly explained in Sec. 4.1. The ringdown waveform model used in this work is described in Sec. 4.2. To test the performance of the new method developed here, in Sec. 4.3 we analyse the ringdown signature of GW150914 and compare our results with those published in [77, 92]. The ringdown analysis with higher order modes is performed on a simulated signal in Sec. 4.4. Finally, the chapter is summarised in Sec. 6.5. The PyCBC Inference algorithm was mainly developed by Chris Biwer and Collin Capano, and the ringdown infrastructure presented in this chapter was developed by the author.

## 4.1 Bayesian inference

The probability density  $p(\theta|H)$ , where  $\int p(\theta|H) d\theta = 1$ , describes the plausibility that an unknown parameter  $\theta$  is true given a model hypothesis  $H$ . Bayesian inference is based on Bayes' theorem, which uses  $p(\theta|H)$  as a prior probability to infer a posterior probability  $p(\theta|d, H)$  from the data  $d$ :

$$p(\theta|d, H) = p(\theta|H) \frac{p(d|\theta, H)}{p(d|H)} \quad (4.1)$$

where  $\mathcal{L}(d|\theta) = p(d|\theta, H)$  is called the likelihood function [89]. The denominator  $p(d|H)$  is called the evidence for the model  $H$  [93]. Because the evidence is independent of the parameter  $\theta$ , it just appears as a normalisation constant. Coalescing binaries are characterised by many parameters  $\theta_i$ , therefore we wish to obtain the joint probability distribution for the set of parameters  $\vec{\theta} = \{\theta_i\}$ . To isolate a specific parameter from the joint probability  $p(\vec{\theta}|d, H)$ , one can marginalise over the uninteresting parameters

$$p(\theta_1|d, H) = \int p(\vec{\theta}|d, H) d\theta_2 \dots d\theta_n. \quad (4.2)$$

This marginalised probability distribution is used to construct credible intervals for the parameter  $\theta_1$ .

In the particular case of gravitational-wave parameter estimation, we model our data as  $s(t) = n(t) + h(t)$ . Here,  $n(t)$  is the noise model and  $h(t)$  is the gravitational-wave signal present in the data. In general,  $n(t)$  is approximated as stationary, Gaussian noise. However, real noise is not always stationary and can contain non-Gaussian noise transients (glitches). For instance, we saw a particular type of glitch in the previous chapter that is very harmful for compact binary searches. Gravitational-wave searches use long stretches of data and have to account for these real noise characteristics. Parameter estimation, however, is performed on a short stretch of data where the signal is present. The parameter estimation formalism is derived under the assumption that noise is stationary and Gaussian, with zero mean and a known variance estimated from the power spectrum [89]. Typically this approximation is good enough in the neighbourhood of an astrophysical signal. Otherwise, glitch subtraction or data cleaning techniques can be

used prior to the Bayesian inference calculation, such as was done for the binary neutron star GW170817 [55]. With this noise model we have [91]

$$\mathcal{L}(s|\vec{\vartheta}) = p(s|\vec{\vartheta}, h) \propto \exp \left[ -\frac{1}{2} \langle s - h(\vec{\vartheta}) | s - h(\vec{\vartheta}) \rangle \right], \quad (4.3)$$

Given a network of  $N$  detectors, assuming that the noise is uncorrelated between detectors, the coherent network posterior distribution is given by [89, 94]

$$\begin{aligned} p(\vec{\vartheta}|s, h) &\propto p(\vec{\vartheta}|h) \prod_{a=1}^N \mathcal{L}_a(s|s_a) \\ &\propto p(\vec{\vartheta}|h) \exp \left[ -\frac{1}{2} \sum_{a=1}^N \langle s_a - h_a(\vec{\vartheta}) | s_a - h_a(\vec{\vartheta}) \rangle \right], \end{aligned} \quad (4.4)$$

where  $s_a$  is the data from the  $a$ -th detector and  $h_a$  is the template waveform as it would be observed in the  $a$ -th detector. Recall from Chap. 1 that the strain produced by the gravitational wave at the detector is

$$h(t) = F_+(\theta, \phi, \Psi) h_+(t) + F_\times(\theta, \phi, \Psi) h_\times(t), \quad (4.5)$$

with the antenna pattern functions  $F_{+,\times}$  defined in Eqs. (1.18) and (1.19). The noise-weighted inner product  $\langle x|y \rangle$  is defined as in Chap. 2

$$\langle x|y \rangle = 4 \Re \left( \int_0^\infty \frac{\tilde{x}(f)\tilde{y}^*(f)}{S_n(f)} df \right), \quad (4.6)$$

where  $S_n(f)$  is the single-sided power spectral density (PSD) of the detector noise.

To evaluate Eq. (4.4) over a large, multidimensional space of parameters  $\vec{\vartheta}$ , PyCBC Inference uses stochastic samplers based on Markov-Chain Monte Carlo (MCMC) techniques. The samplers construct an ensemble of Markov chains, also known as walkers, that randomly jump through the parameter space to draw samples from the distribution. For a proposed new sample, the product of the prior and the likelihood determines if the jump is accepted or rather the walker remains at the same point. The output of the parameter estimation algorithm is a set of samples from the posterior distribution  $p(\vec{\vartheta}|d, H)$ , which can then be used to estimate the median and the chosen credible intervals for each parameter  $\theta_i$ . In this chapter we use the MCMC samplers `kombine` [95] and `emcee` [96].

## 4.2 Ringdown model

To calculate the likelihood function for a given set of parameters  $\vec{\vartheta}$  we need a template model  $h(\vec{\vartheta})$ . Chapter 1 briefly described gravitational waveforms originating from the ringdown phase of a binary black hole coalescence. In this section we describe in more detail the ringdown template that is used throughout this chapter.

As we saw in Sec. 1.2, the late ringdown phase of a compact binary coalescence is described through perturbation theory. For a Kerr black hole, the ringdown signal consists of a superposition of exponentially damped sinusoids [36]. Assuming that the ringdown waveform begins at  $t = 0$ , i.e.  $h(t < 0) = 0$ , the two polarisations of the gravitational waveform are given by

$$\begin{aligned} h_+(t) &= \sum_{\ell,m,n} {}_{-2}Y_{\ell m}^+(\iota) A_{\ell mn} e^{-t/\tau_{\ell mn}} \cos(2\pi f_{\ell mn} t + \beta_{\ell mn}), \\ h_\times(t) &= \sum_{\ell,m,n} {}_{-2}Y_{\ell m}^\times(\iota) A_{\ell mn} e^{-t/\tau_{\ell mn}} \sin(2\pi f_{\ell mn} t + \beta_{\ell mn}). \end{aligned} \quad (4.7)$$

Instead of the complex frequency  $\Omega_{\ell mn}$  given in Eq. (1.14) we have used the damping time  $\tau_{\ell mn}$  and real frequency  $f_{\ell mn} = \omega_{\ell mn}/(2\pi)$  that define the damped sinusoid. We have also approximated the spin-weighted spheroidal harmonics  ${}_{-2}S_{\ell mn}$  by spin-weighted spherical harmonics  ${}_{-2}Y_{\ell mn}$  [97, 98], and we have defined [98]

$$\begin{aligned} {}_{-2}Y_{\ell m}^+(\iota) &= {}_{-2}Y_{\ell m}(\iota, 0) + (-1)^\ell {}_{-2}Y_{\ell-m}(\iota, 0), \\ {}_{-2}Y_{\ell m}^\times(\iota) &= {}_{-2}Y_{\ell m}(\iota, 0) - (-1)^\ell {}_{-2}Y_{\ell-m}(\iota, 0). \end{aligned} \quad (4.8)$$

The angle  $\beta_{\ell mn} = \phi_{\ell mn} + m\varphi$  in Eq. (4.7) combines the initial ringdown phase with the azimuthal part of the spherical harmonics. Recall from Sec. 1.2 that the angle  $\iota$  is the inclination angle between the line-of-sight vector from the black hole to Earth and the intrinsic angular momentum (spin) of the black hole.

It is common in gravitational-wave data analysis to work in the frequency domain. The Fourier transform of the time domain ringdown polarisations is readily computed analytically. If  $h(t)$  satisfies Eqs. (4.7) for  $t \geq 0$ ,  $h(t) = 0$  for  $t < 0$ , then the frequency domain polarisations are given by

$$\begin{aligned} \tilde{h}_+(f) &= \sum_{\ell,m,n} {}_{-2}Y_{\ell m}^+(\iota) A_{\ell mn} \tau_{\ell mn} \frac{(1 + i 2\pi f \tau_{\ell mn}) \cos(\beta_{\ell mn}) - 2\pi f_{\ell mn} \tau_{\ell mn} \sin(\beta_{\ell mn})}{1 - 4\pi^2(f^2 - f_{\ell mn}^2) \tau_{\ell mn}^2 + i 4\pi f \tau_{\ell mn}}, \\ \tilde{h}_\times(f) &= \sum_{\ell,m,n} {}_{-2}Y_{\ell m}^\times(\iota) A_{\ell mn} \tau_{\ell mn} \frac{(1 + i 2\pi f \tau_{\ell mn}) \sin(\beta_{\ell mn}) + 2\pi f_{\ell mn} \tau_{\ell mn} \cos(\beta_{\ell mn})}{1 - 4\pi^2(f^2 - f_{\ell mn}^2) \tau_{\ell mn}^2 + i 4\pi f \tau_{\ell mn}}. \end{aligned} \quad (4.9)$$

The measurability of higher order modes depends on the detector's sensitivity. With current gravitational-wave detectors, only the fundamental  $(\ell, m, n) = (2, 2, 0)$  mode is expected to be observable. Furthermore, GW150914 is the only binary black hole detected so far that has a ringdown signal loud enough for ringdown parameter estimation. In the next section we test our new framework on the ringdown signature of GW150914.

### 4.3 Single-mode parameter estimation on GW150914

With the Bayesian inference methods and the ringdown model described in the previous sections, we can estimate the ringdown parameters of the binary black hole GW150914.

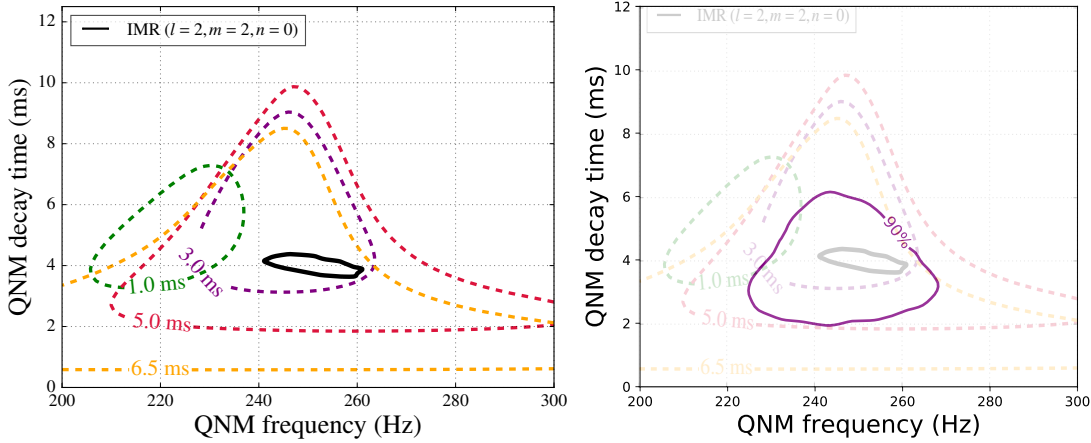


Figure 4.1: Combined posterior distribution for the frequency and the damping time of a single mode ringdown waveform. The contours show the 90% credible level. (Left) Results published in [92]. Four different analyses were performed, starting the ringdown at different times after the coalescence time. Dashed contours show the results of each analysis. The solid contour is the value predicted from Numerical Relativity. (Right) Results obtained with the method described here, using PyCBC Inference and `kombine`. This analysis was performed starting the ringdown at a time  $t = 3$  ms after the coalescence. The results published in [92] are overlaid on top for comparison.

The method described in [91], used on GW150914 in [92], did not fully incorporate the effects of the sky location. Instead, the LIGO Livingston data was time-shifted by 7 ms to account for the arrival time difference, and multiplied by  $(-1)$  to account for the inverse detector response. Our method is an extension of [91], in which we coherently analyse data from multiple detectors by means of Eq. (4.5). Furthermore, the method in [91] only supports a single-mode ringdown analysis, while our ringdown model allows for the addition of higher order modes. In the next section we will see the performance of the multi-mode analysis on a simulated ringdown-only signal. For now, we restrict ourselves to the fundamental mode  $(\ell, m, n) = (2, 2, 0)$  to reproduce the analysis performed in [92].

The set of variables in our model is  $\vec{\vartheta} = (f_{220}, \tau_{220}, A_{220}, \beta_{220})$ . Typically, the source's sky location and polarisation are also variable arguments. However, performing the parameter estimation analysis on a portion of the signal complicates the issue of dealing with the sky location. We will develop later in Chap. 6 a method to overcome this issue. Here, as a proof of principle, we fix the sky location and polarisation to the maximum posterior values of the full inspiral-merger-ringdown parameter estimation analysis.

Numerical simulations predict that the damped sinusoid description of the ringdown starts being meaningful at a time approximately  $10M_f$  after the coalescence [99], with  $M_f$  the mass of the final black hole. For GW150914 this corresponds to  $t \simeq t_c + 3$  ms, with  $t_c$  the coalescence time of the signal. It was observed in [92] that starting the ringdown at this time, the posterior distribution for the frequency and damping time matched the numerical predictions. Therefore, we fix the start time of the ringdown to  $t = t_c + 3$  ms. We choose uniform prior distributions in the range  $f_{220} \in [200, 300]$

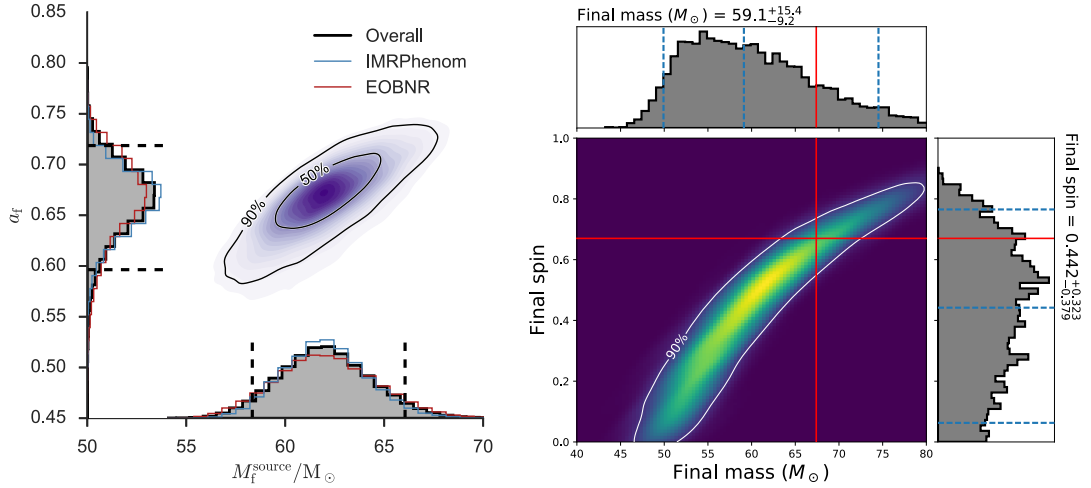


Figure 4.2: Combined posterior distribution for the mass and the spin of a single mode ringdown waveform. The (outer) contours show the 90% credible level. (*Left*) Results published in [77]. These results show the source-frame mass and spin. Values for the detector-frame mass and spin of this event are given in Table 1.1. (*Right*) Results obtained with the method described here, starting the ringdown at a time  $t = 3$  ms after the coalescence. Here, the results show the detector-frame mass and spin. For comparison, the red cross marks the detector-frame parameters quoted in [77].

Hz and  $\tau_{220} \in [0.5, 20]$  ms, as in [91, 92]; and  $A_{220} \in [0, 10^{-20}]$  and  $\beta_{220} \in [0, 2\pi)$  for the amplitude and phase. Figure 4.1 shows the 90% credible interval obtained in our analysis using `kombine`, compared to the results published in [92]. The reference result from [92] is the purple contour labeled **3.0 ms**. As can be seen in the figure, the posterior distribution of  $f_{220}$  and  $\tau_{220}$  in our analysis favours smaller damping times than the results in [92]. Predicted results from the least quasi-normal mode in Numerical Relativity are consistent with both methods.

Full inspiral-merger-ringdown signals use fitting formulae from Numerical Relativity simulations [100–102] that relate the initial parameters of the binary with the parameters of the final black hole. Thus, the final mass and spin of the black hole published in [77] are dependent on the configuration of the binary prior to the merger, exactly as predicted by General Relativity. The frequency and damping time of the ringdown are characteristic of the black hole's mass  $M_f$  and spin  $\chi_f$ . Thus, the mass and spin of the final Kerr black hole can be inferred from the ringdown stage of the coalescence, without prior knowledge about the inspiral. Fitting formulae that relate the ringdown's frequency and damping time with the black hole's mass and spin have been published in [103]. Using these fitting formulae, we can construct a ringdown approximant that takes the mass and spin as input parameters. Because the mass-spin mapping is mode dependent, we also need to specify the quasi-normal mode. Choosing the  $(\ell, m, n) = (2, 2, 0)$  mode, the set of variables in this model is  $\vec{\vartheta} = (M_f, \chi_f, A_{220}, \beta_{220})$ . We fix the sky location and the time to the same values as in the previous analysis, and use the same prior distributions for

the amplitude and phase. For the mass and spin we choose uniform prior distributions in the range  $M_f \in [20, 100) \times M_\odot$  and  $\chi_f \in [-0.9995, 0.9995]$ . Figure 4.2 shows the 90% credible interval obtained in our analysis compared to the results published in [77]. In the figure, the results from [77] are given in terms of the source-frame mass, while our results show the detector-frame results. For comparison, the detector-frame mass and the spin quoted in [77],  $M_f \simeq 67.4M_\odot$  and  $\chi_f \simeq 0.67$ , are marked with a red cross in our results. As can be seen in the figure, the posterior distribution of  $M_f$  and  $\chi_f$  in our analysis is consistent with the values quoted for the detector-frame mass and final spin in [77]. Because we only use a small portion of the signal in our analysis, our posterior distribution is wider than the one obtained with full inspiral-merger-ringdown templates.

#### 4.4 Multi-mode parameter estimation on simulated signals

In general, higher order modes are present in the ringdown signal. However, subdominant modes typically have much lower amplitudes than the fundamental  $(2, 2, 0)$  mode [98, 99, 104]. The amplitude of each mode depends on the initial parameters of the binary, namely on the mass ratio  $q = m_1/m_2$  and the initial spins. Equal-mass, non-spinning binaries have vanishing  $A_{330}$  and  $A_{210}$ , with the loudest subdominant mode being usually the  $(4, 4, 0)$  mode. However, equal-mass binaries are not good candidates to measure quasi-normal modes, because the relative amplitude of the loudest subdominant mode

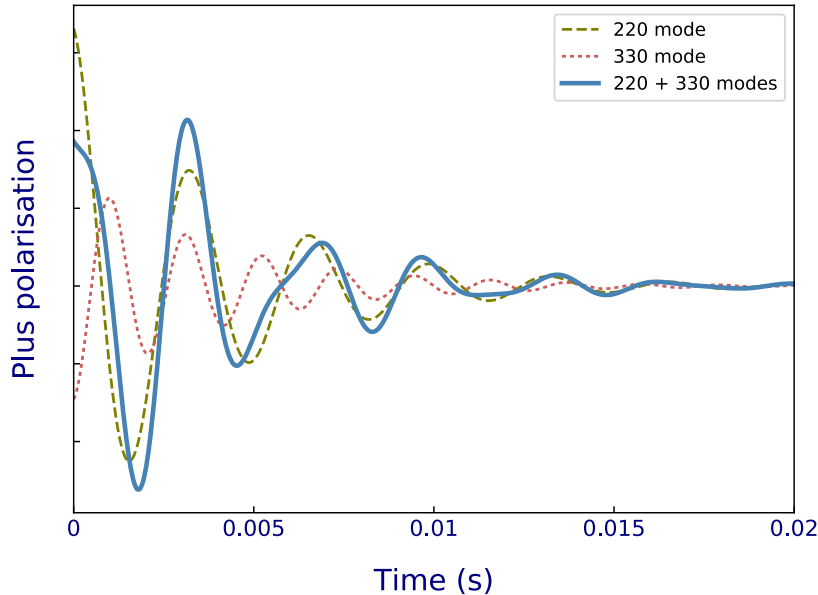


Figure 4.3: Plus polarisation ( $h_+(t)$ ) of a ringdown waveform with two quasi-normal modes for a black hole with mass  $M_f = 62.3M_\odot$  and spin  $\chi_f = 0.79$ . Dashed and dotted lines show the individual  $(2, 2, 0)$  and  $(3, 3, 0)$  modes, with  $A_{330}/A_{220} = 1/3$ . The continuous line is the ringdown resulting from the superposition of both quasi-normal modes.

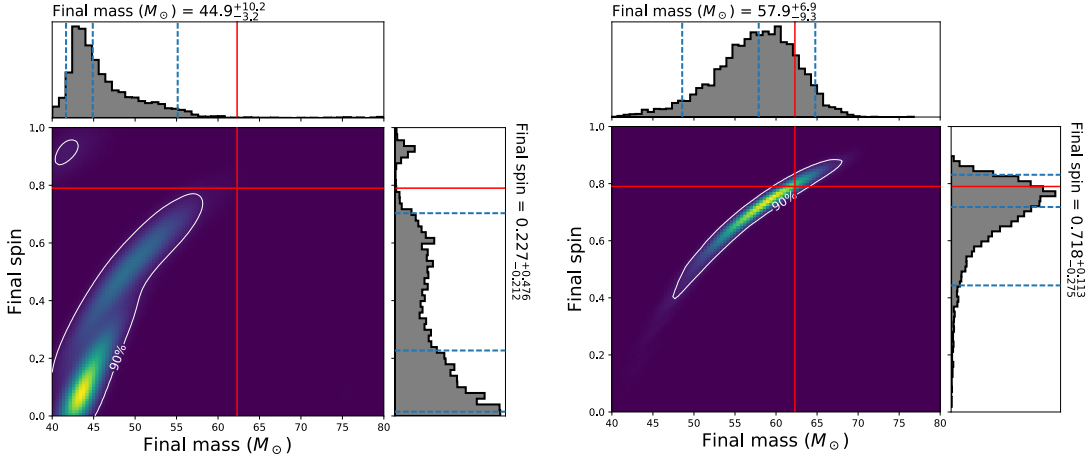


Figure 4.4: Combined posterior distribution for the mass and the spin of a simulated two-mode ringdown waveform. The contours show the 90% credible level. The red cross indicates the injected values. (Left) Results obtained using a single mode ringdown template. (Right) Results obtained using a two-mode ringdown template.

is expected to be  $A_{440}/A_{220} \simeq \mathcal{O}(10^{-2})$  [99]. In binaries with higher mass ratios, the loudest subdominant modes are usually the  $(3, 3, 0)$  or  $(2, 1, 0)$  modes. In this section, we simulate the ringdown signature of a black hole with mass  $M_f = 62.3 M_\odot$  and spin  $\chi_f = 0.79$ . The simulated ringdown waveform is the superposition of two quasi-normal modes: the  $(2, 2, 0)$  and  $(3, 3, 0)$  modes with  $A_{330}/A_{220} = 1/3$  (compact binaries with mass ratios  $q \gtrsim 4$  are expected to achieve such relative amplitudes [99]). Figure 4.3 shows the difference between the individual quasi-normal modes and the ringdown signal resulting from the superposition of both modes.

We inject the two-mode ringdown waveform in simulated Gaussian noise, and perform the parameter estimation using first a single-mode template and then a two-mode template. We choose the power spectral density (PSD) characteristic of the first observing run of Advanced LIGO, as given in [105] for GW150914. To be able to measure the subdominant mode with this PSD, we generate a ringdown waveform about 2.5 times louder in signal-to-noise ratio than that of GW150914. In this case, we use the sampler `emcee`. First, we examine how well one can recover the mass and spin of the black hole using a single-mode template. The prior distributions are the same as in the previous section, but we extend the mass range to  $M_f \in [2, 100) \times M_\odot$  and the amplitude range to  $A_{220} \in [0, 5 \times 10^{-20}]$ . The left panel in Fig. 4.4 shows the resulting mass and spin posterior distributions, with the red cross indicating the injected parameters. As can be seen in the figure, a bias is introduced in the intrinsic parameters of the black hole and the single-mode analysis cannot recover the expected values.

If the subdominant modes are loud enough, a multi-mode ringdown template is required. In the ringdown infrastructure presented in this chapter, the number of modes is set by a list of  $(\ell, m)$  modes and the number of overtones  $n$ . A priori, the algorithm does not know which mode is the louder mode. Consequently, the parameter estimation

algorithm could switch between modes, yielding a bimodal posterior distribution. Therefore, we define our ringdown approximant such that the amplitude of the  $(2, 2, 0)$  mode is given as an absolute amplitude,  $A_{220}$ , and the amplitudes of other  $(\ell, m, n)$  modes are given as relative amplitudes,  $A_{\ell mn}/A_{220}$ . With this configuration, we set uniform prior distributions for the  $(3, 3, 0)$  amplitude in the range  $A_{330} \in [0, 0.9] \times A_{220}$ . The right panel of Fig. 4.4 shows the resulting mass and spin posterior distributions of the two-mode ringdown parameter estimation. As can be seen in the figure, the expected parameters are now within the 90% credible interval. It is therefore important to construct a robust multi-mode parameter estimation infrastructure for future sensitivities, when higher order modes become observable.

## 4.5 Conclusions

In this chapter we developed a new method to perform parameter estimation on the ringdown phase of a gravitational-wave signal. The ringdown model consists of a superposition of quasi-normal damped sinusoids. In principle, the number of modes can be chosen arbitrarily. As a proof of principle, we first tested this new method using single-mode ringdown templates on GW150914. Our results were consistent with results published in [77, 92]. Furthermore, we showed that it is possible to measure the mass and spin of the final Kerr black hole using only the ringdown signature of the gravitational waveform. This measurement can be used to test the area theorem, as we will see in Chap. 6.

With current detector sensitivities, higher modes are still too quiet to be detectable. In fact, even the dominant  $(2, 2, 0)$  mode is still too quiet for most of the binary black hole events. GW150914 is the only gravitational-wave signal with an observable ringdown signature, yet only the fundamental mode is above the noise level of the detectors. To test the performance of the multi-mode analysis, we simulated a two-mode ringdown signal in Gaussian noise. The analysis on this simulated signal was performed first with single-mode templates and then with two-mode templates. We saw that with single-mode templates the expected parameters cannot be recovered, while two-mode templates yield consistent results. Therefore, future sensitivities will require that the ringdown analysis is performed with higher modes. In this chapter, we presented preliminary results on multi-mode parameter estimation. Further work on this area is currently ongoing, and we leave for a future study to analyse if templates with higher order modes perform equally well on signals with lower signal-to-noise ratio, where only the fundamental mode is measurable and single-mode templates are in principle sufficient.

In real signals the existence of measurable subdominant modes is a priori unknown. Ideally, ringdown templates for parameter estimation should include an arbitrary number of quasi-normal modes. The procedure would then consist on evaluating how many modes are consistent with the data. If two or more modes have been identified, it could be possible to establish if the corresponding frequencies and damping times match at least one pair of mass and spin. This measurement would enable to test the no-hair theorem. The Bayesian inference framework also enables the distinction between two

competing models. By means of the Bayes factor one can estimate how much more likely the observed data matches one model over the other [89]. Implementing ringdown models for exotic compact objects, this feature can be used to estimate if the final black hole is consistent with a Kerr black hole rather than another hypothetical object.

As one can see, many interesting tests arise from measuring the ringdown signal. The test of the no-hair theorem requires the measurement of higher order modes [43][106], which might not be observable at least until Advanced LIGO reaches design sensitivity. Model selection between a Kerr black hole and an exotic compact object requires model waveforms which are not currently known or available. Therefore, in the rest of this work we focus on what can potentially be accomplished with current detectors: testing the area theorem. We have developed here a method to extract the mass and spin of the final object using only the ringdown stage of the signal and a single-mode damped sinusoid. We need now an infrastructure to obtain the initial masses and spins from the inspiral only, so that we exclude the highly dynamical merger. However, the distinction between the inspiral and the merger is far from well understood. In the next chapter we will construct a well-defined inspiral termination that we can use to measure the inspiral parameters.

# Chapter 5

## The end of the inspiral in the post-Newtonian approximation

Binary systems are ubiquitous in the universe. While most binary systems are well described by Newtonian physics, some systems orbit closely enough that relativistic effects become important for describing their dynamics. The full solution to the two body problem describing these dynamics has not been solved analytically in General Relativity. If the mass of the secondary body can be neglected then the orbit can be approximated as a test-mass orbit in a one-body solution, such as the Kerr solution, which describes a rotating black hole [26]. In this case there is an innermost equatorial orbit beyond which the test-mass cannot orbit equatorially. This innermost stable circular orbit (ISCO) is often taken as the inner-edge of the accretion disks around black holes [107, 108] to measure the spin of the black hole, for instance. A description of the system by test-mass dynamics, however, is meaningful only when the mass of the companion is much smaller than the mass of the primary object.

If the companion is another object of comparable mass, the spacetime of the system is not well described by the Kerr solution. A number of approximation methods are used in this case, including the post-Newtonian approximation. Post-Newtonian (PN) theory yields an analytical approximation of the motion of compact binaries, under the assumptions of weak gravitational fields inside the sources and of slow internal motion [109]. Despite these limitations, the PN approximation has proven to be an unexpectedly effective description [32]. Observational limits on deviations from the calculated PN coefficients are given in [51].

The radiation of energy in the form of gravitational waves plays an important role in the motion of relativistic compact binaries. The gravitational-wave emission causes the orbit to gradually shrink, bringing the bodies closer together in a long inspiral phase [110]. After the long inspiral, the evolution is typically followed by a plunge, merger, and ringdown. However, these processes can be interrupted if one of the objects (or both) is a neutron star. Depending on its internal composition and orbital parameters, the neutron star can be tidally deformed and even completely disrupted before the plunge phase [111, 112]. This has been proposed as a possible mechanism to

explain short gamma-ray bursts [113], and recently observed on the binary neutron star GW170817 [56].

In the absence of tidal disruption, the orbital energy gradually decreases until it reaches a minimum. Based on physical insight from the extreme mass-ratio limit in the Kerr spacetime, this minimum, when it exists, can be considered as the end of the inspiral. The orbit at which the energy reaches its minimum value is called the minimum energy circular orbit (MECO)<sup>1</sup>. If the PN approximation for the energy is valid, the MECO will be the minimum of the PN energy. As we will see, direct application of the minimum energy condition to the known PN energy leads to a MECO that depends sensitively on the PN order and the intrinsic angular momentum (spin) of the black hole.

In the Schwarzschild and Kerr spacetimes the MECO coincides with the ISCO, as well as in any system defined by an exact Hamiltonian [115, 116]. However, it has been shown that this statement is not necessarily true in the PN approximation [114, 115, 117]. Blanchet and Iyer [117] computed the ISCO for non-spinning objects in the PN formalism studying the stability of circular orbits against linear perturbations of the equations of motion. They observed that the PN corrections increase the frequency of the ISCO with respect to the Schwarzschild solution and thus the ISCO radius is smaller in PN theory than in the Schwarzschild case. Furthermore, this ISCO differs from the MECO. A generalisation of their method for spinning objects has been performed by Favata [118].

Models for the complete evolution of binary black hole systems have recently been developed [59, 60]. These extend PN techniques by including Numerical Relativity results from regions where the PN approximation breaks down. However, the end of the inspiral in compact binaries is still of great theoretical and practical interest for the two-body problem in General Relativity. The dynamics of the coalescence qualitatively change in the transition from the inspiral to the plunge. PN theory breaks down close to the merger due the nature of the approximation. This breakdown is not well-defined, yet a critical issue for gravitational-wave modelling.

The merger represents the violent collision of two compact objects in the fully non-linear regime. The parameters of these objects must be independently measured prior to merger in order to test whether the object that results from such a collision is compatible with what General Relativity predicts. For instance, some tests of General Relativity with gravitational-wave observations distinguish between the inspiral and the last phases of the waveform [92, 119], and tests of Hawking's area theorem [120] shall be restricted to the inspiral phase when determining the initial areas [121, 122]. Therefore, waveforms to describe the inspiral phase require knowledge of a suitable end point. In the past, either the exact Schwarzschild ISCO or the PN MECO have been used as the frequency cutoff for inspiral waveforms (see [90, 123, 124], for instance). However, both approaches have their limitations. The existence of an ISCO in the full two-body problem is uncertain and hard to calculate in the PN framework. The validity of using the test-mass value is also not guaranteed for comparable-mass systems. Conversely, the MECO does not always have a finite value. This limits the PN terms that can be included when using this method.

---

<sup>1</sup>Also innermost circular orbit (ICO) in the literature [114].

In this chapter we study the properties of the MECO in the post-Newtonian theory. We seek to obtain a MECO that exists for any known PN order, any mass ratio and any value of the spins of the objects. In the extreme mass ratio inspiral case, the PN approximation is poorly convergent, but one can use the test-mass dynamics of the exact solution directly [114]. Following the idea of a hybrid approach introduced in [125] we include exact test-limit results into the PN approximation and show that it fulfils our criteria. In [125] this was used only with non-spinning Schwarzschild like systems, but we extend this to spinning systems. In our case, the MECO represents the maximum limit of the validity of the PN approximation. We compare our limit to the point of peak amplitude emission in the spinning effective-one-body model calibrated to Numerical Relativity (SEOBNR [60]). The SEOBNR peak is the expected value of the instantaneous gravitational-wave frequency at the time when the (2,2) mode amplitude peaks in numerical simulations. Typically, the time at which the common apparent horizon forms in numerical simulations of binary black hole mergers is very close to the time at which the amplitude peaks. Therefore, the SEOBNR peak can be viewed as a proxy for the frequency at which the merger occurs [126]. If there is a plunge phase, then the end of the inspiral will occur before this.

We are particularly interested here in binaries with equal masses and low mass ratios, where PN is expected to be better behaved, but no exact solution is known. For comparison, we consider mainly two cases: i) a neutron-star black-hole binary (NSBH) of mass ratio  $q = m_{\text{BH}}/m_{\text{NS}} \simeq 7$ , where the spin of the neutron star is set to zero, and ii) an equal-mass binary black hole (BBH), where both black holes have the same spin. For these binary systems, we analyse in section 5.1 the dependence of the MECO on the spin and on the PN order. In section 5.2, we use the exact Kerr MECO to analyse the test-mass limit. Section 5.3 computes a well-defined MECO which has a finite value for any PN order and any spin. Since our result depends only on the mass ratio and not on the total mass of the binary, it can also be used for systems containing intermediate-mass or supermassive black holes. In section 5.4 we use the signal-to-noise ratio (SNR) as a measure of approximately how much extra inspiral signal is gained or lost when using different choices for the end of the inspiral. Section 5.5 investigates if the integrands used for PN waveform generation are well-posed through the new MECO termination point. This result is important for faithfulness studies of different waveform models. Finally, as an example of the flexibility of our approach, section 5.6 considers tidal effects in NSBH with comparable masses (mass ratio  $q \simeq 2$ ), such as those published in [127, 128], and shows how they can be included straightforwardly.

Throughout this chapter we use geometrical units  $G = c = 1$ . We present most of our results in terms of the PN velocity parameter  $v$ . In the Newtonian limit this corresponds to the sum of the orbital speeds of the two orbiting objects and also in the Schwarzschild limit corresponds to the Schwarzschild coordinate velocity of an orbiting test mass. However, in more general cases,  $v$  should be interpreted as a formal expansion parameter related to the gravitational wave dominant mode frequency by  $v^3 = \pi M f_{\text{GW}}$ . We denote the total mass by  $M = m_1 + m_2$ , the individual masses of the bodies by  $m_i$ , the mass ratio by  $q = m_1/m_2 \geq 1$  and the symmetric mass ratio by  $\eta = m_1 m_2 / (m_1 + m_2)^2 \leq 0.25$ .

For simplicity, we consider the case where the black-hole spin is aligned or anti-aligned with the orbital angular momentum. Precessing systems are expected to broadly follow similar lines in terms of their projected spins, but we leave a detailed analysis to further work. The projection of the dimensionless spin of the black hole onto the orbital angular momentum is denoted by  $\chi_i = \vec{S}_i \cdot \hat{L}/m_i^2$ , where  $\vec{S}_i$  is the intrinsic angular momentum and  $\hat{L}$  is the unit vector along the orbital angular momentum. The projected spin can take values  $-1 \leq \chi_i \leq 1$ , where positive spins indicate alignment with the orbital angular momentum, and negative spins indicate anti-alignment.

The work presented in this chapter was mainly performed by the author and published in [129]. Studies of the post-Newtonian MECO which led to the main result of this work were accomplished together with Andrew Lundgren. Alex Nielsen provided Mathematica notebooks containing some of the PN terms, and useful comments and discussions during the process of writing the paper. Collin Capano helped with the symmetrisation of the hybrid MECO and made the plots in Fig. 5.6.

## 5.1 Behaviour of the MECO at different post-Newtonian orders

The PN energy and flux are given as series expansions in the PN velocity parameter,  $v$ . Terms of order  $v^{2n}$  are called  $n$ PN terms, where even (odd) powers of  $v$  have integer (non-integer)  $n$ . Under the assumption of circular orbits, the PN expressions get considerably simplified (see Appendix C). This is a reasonable approximation for late-time systems dominated by gravitational wave emission, since the decay of the orbital eccentricity happens much faster than the coalescence of isolated circularly orbiting binaries [29]. For non-spinning systems, the PN energy in the centre-of-mass frame for circular orbits is known up to 4PN order and the flux up to 3.5PN [31, 130]. The spin corrections to the energy are known up to the 4PN spin-spin [131, 134] and the 3.5PN spin-orbit [135, 136] terms. Spin-cubed terms appear at the 3.5PN order [136, 137], and spin-quartic terms at 4PN order [134].

For consistency, the PN energy in the test-mass limit ( $m_2 \rightarrow 0$ ,  $m_1$  fixed) should reproduce the Taylor expansion of the orbital energy of a test-mass in the Kerr spacetime up to the PN order considered. In this extreme mass-ratio limit, one can use the exact Kerr solution, where the end of the inspiral is given by the Kerr ISCO. The location of the Kerr ISCO in the equatorial plane depends on the spin of the black hole and, in Boyer-Lindquist coordinates, is given by [41]

$$r = m \left[ 3 + Z_2 \mp \sqrt{(3 - Z_1)(3 + Z_1 + 2Z_2)} \right], \quad (5.1)$$

where  $Z_1 = 1 + (1 - \chi^2)^{1/3} \left[ (1 + \chi)^{1/3} + (1 - \chi)^{1/3} \right]$ ,

$$Z_2 = \sqrt{3\chi^2 + Z_1^2},$$

$m$  is the mass of the Kerr black hole, and  $\chi$  is its spin relative to the orbital angular momentum. For spin zero, the Kerr ISCO reduces to the Schwarzschild ISCO,  $r = 6m$ .

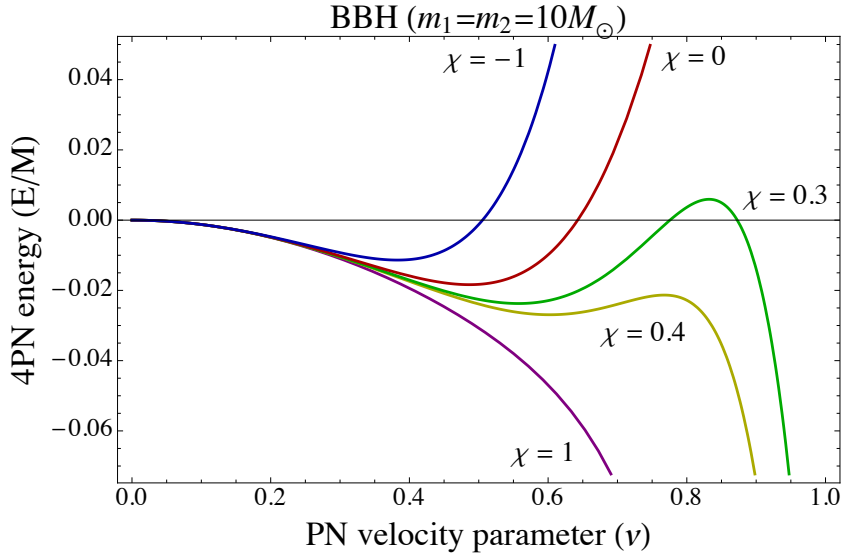


Figure 5.1: Current 4PN energy per unit mass as function of the PN velocity parameter,  $v$ , for an equal-mass BBH. The two black holes are considered to have equal spin,  $\chi_1 = \chi_2 = \chi$ . For some values of positive spins the energy shows a maximum after the minimum, as can be seen with  $\chi \simeq 0.3$  for instance. For higher spins, the energy does not reach a minimum and therefore the MECO does not exist at the 4PN order.

The upper sign in Eq. (5.1) is for prograde orbits (spin of the black hole aligned with the orbital angular momentum), while the lower sign is for retrograde orbits (spin anti-aligned with the orbital angular momentum). For extremal spin ( $\chi = \pm 1$ ), the Kerr ISCO is located at  $r = m$  (aligned case) and  $r = 9m$  (anti-aligned case). If the mass and spin of the smaller body are not totally neglected, but considered small, self-force calculations provide the corrections due to the effect of the second body [138] [140].

As the mass ratio decreases, the system does not follow test-mass dynamics of the exact Kerr solution. The PN approximation can be used in this regime to calculate a PN orbital energy. The MECO is then defined as the minimum of this PN energy, corresponding to the velocities at which  $dE^{\text{PN}}/dv = 0$ . Figure 5.1 shows the energy including terms up to 4PN order for BBH systems with different spins, where in each case both black holes have the same spin value. The orbital energy decreases and reaches a minimum that represents the end of the inspiral (the MECO). What occurs after the minimum is to be discarded physically, since the adiabatic assumption is certainly violated beyond this point. For high spin values, the energy does not show a minimum, and therefore the MECO does not exist. Due to the absence of a minimum of the energy in certain regions of the parameter space, the current MECO cannot be used as a robust definition of the end of the inspiral.

Figure 5.2 shows the PN velocity parameter of the PN MECO when including terms up to three different PN orders: 3PN, 3.5PN and 4PN. The double valued curves for the 3.5PN and the 4PN BBH cases correspond to maxima and minima, as shown for example in the  $\chi = 0.3$  curve of Fig. 5.1. For comparison, the ISCOs (see Appendix B for

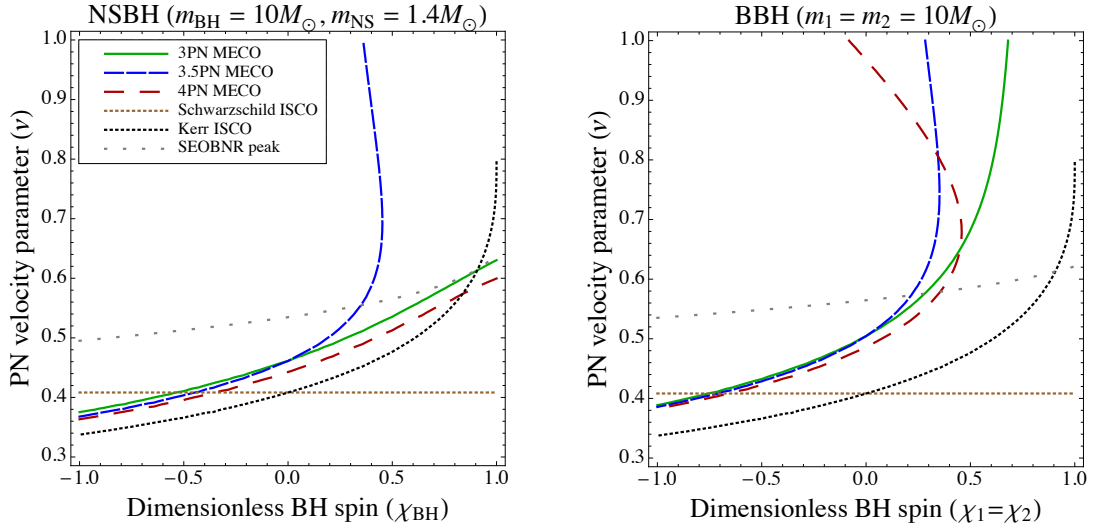


Figure 5.2: Different inspiral-cutoffs for NSBH and BBH as function of the PN velocity parameter,  $v$ . Dotted lines represent the Schwarzschild ISCO (which is independent of the spin value), the Kerr ISCO, and the SEOBNR peak. Continuous and dashed lines represent the extrema of the PN energy (the MECO and possible maxima of the energy) up to different PN orders. The neutron-star spin is considered negligible compared to the black-hole spin and therefore set to zero. The black-hole spins are equal in the BBH case and aligned (positive  $\chi$ ) or anti-aligned (negative  $\chi$ ) with the orbital angular momentum. Except for the even 3PN and 4PN orders in the NSBH case, the MECO does not exist in the region of high aligned spins.

the relations between the ISCO radius and its orbital velocity) and the SEOBNR peak (obtained from the LSC Algorithm Library Suite [141]) are also shown. As can be seen in Fig. 5.2, the MECO depends sensitively on the PN order, and does not exist in certain regions of parameter space for certain PN orders. For high values of the black-hole spins in the BBH case for instance, the MECO does not exist for any of the three PN orders shown. The NSBH shows the same behaviour for the odd 3.5PN order, while the even 3PN and 4PN energies reach a minimum for any value of the black-hole spin.

## 5.2 PN expansions of the test-mass limit

The PN approximation is poorly convergent in the test-mass limit, but is expected to be quite accurate in the comparable-mass regime [114]. Therefore, one would expect the MECO to be well-defined for comparable-mass binaries. However, the previous section has shown that the MECO does not exist for high spins in the equal-mass case. Since this issue does not seem to be mitigated by the addition of higher PN orders, here we analyse the test-mass case, where the PN approximation is already known to fail.

The orbital energy per unit mass of a test-mass around a Kerr black hole can be given as [41, 118]

$$E^{\text{Kerr}} = \left( \frac{1 - 2w + \chi w^{3/2}}{\sqrt{1 - 3w + 2\chi w^{3/2}}} - 1 \right), \quad (5.2)$$

where  $w = \frac{v^2}{(1-\chi v^3)^{2/3}}$ . Here,  $\chi$  is the projected spin of the black hole, and  $v$  is the equivalent PN velocity parameter of the test-mass particle given by  $v^3 = 2\pi M/T$ , where  $T$  is the period of the orbit in Boyer-Lindquist coordinates. For a Kerr black hole, the ISCO coincides with the MECO, which is obtained by solving

$$\frac{dE^{\text{Kerr}}}{dv} = 0. \quad (5.3)$$

This reduces to obtaining the velocity at which

$$\left[ 3\chi^2 v^4 - (1 + 7\chi v^3) (1 - \chi v^3)^{1/3} + 6v^2 (1 - \chi v^3)^{2/3} \right] = 0. \quad (5.4)$$

In the test-mass limit ( $m_2 \rightarrow 0$ ,  $m_1$  fixed), the PN energy (given in Appendix C) equals the Taylor expansion of the Kerr energy up to the highest PN order known. Expanding Eq. (5.2) up to 4PN, we obtain<sup>2</sup>

$$\begin{aligned} E^{\text{Kerr}}(\chi_1) &\simeq \frac{E^{\text{PN}}}{\eta} \Big|_{m_2 \rightarrow 0} \\ &= -\frac{1}{2}v^2 \left[ 1 - \frac{3}{4}v^2 + \frac{8\chi_1}{3}v^3 - \left( \frac{27}{8} + \chi_1^2 \right)v^4 + 8\chi_1 v^5 - \left( \frac{675}{64} + \frac{65\chi_1^2}{18} \right)v^6 \right. \\ &\quad \left. + 27\chi_1 v^7 - \left( \frac{3969}{128} + \frac{469\chi_1^2}{24} \right)v^8 + \mathcal{O}(v^9) \right]. \end{aligned} \quad (5.5)$$

A comparison of the exact Kerr MECO [Eq. (5.4)] to its approximation at different “PN orders” (given by the minimum of Eq. (5.5) up to the chosen order) can be seen in Fig. 5.3. At higher spins, the MECO of the 4PN expansion for the Kerr energy does not resemble the MECO of the exact Kerr energy. Therefore, the MECO of the post-Newtonian energy is unlikely to resemble the MECO of the unknown exact solution, if it exists. Figure 5.3 also shows that even if one knew the post-Newtonian energy up to 14.5PN, the test-mass part would likely only agree with the exact known solution up to spins of  $\chi \simeq 0.5$ , or velocities of  $v \simeq 0.45$ . Another remarkable feature of the expansion of the Kerr energy is the different behaviour between odd and even PN orders. While even PN orders appear to have a minimum for any value of the spin, odd PN orders do not present extrema for  $\chi \gtrsim 0.5$ . This behaviour is very similar to what we have seen for the complete PN energy in the NSBH case (only one spinning object).

### 5.3 Stabilisation of the MECO

Mathematically, it is unknown if the PN series can be derived as a Taylor expansion of a family of exact solutions [109]. However, for consistency, its test-mass limit should always equal the expansion of the exact Kerr solution. This expansion has been shown

---

<sup>2</sup>The dimensionless spin  $\chi$  in Eq. (5.5) and the PN spin parameter  $S$  used in Appendix C are related through  $\chi = S/m^2$ .

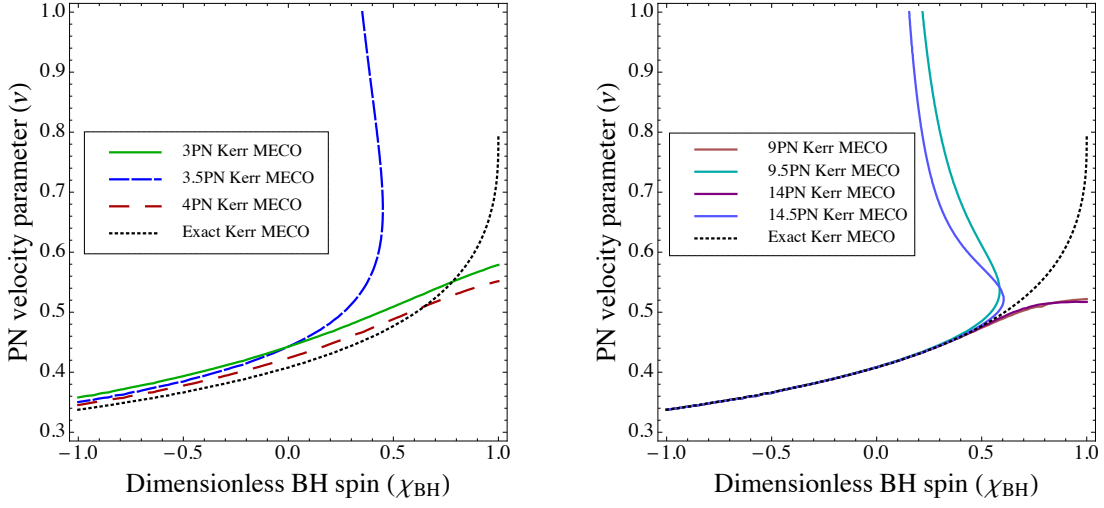


Figure 5.3: MECO for a test mass orbiting a Kerr black hole as function of the PN velocity parameter,  $v$ . The dotted line represents the exact solution. Continuous and dashed lines show different orders of the approximation (5.5), which are called ‘‘PN orders’’ for comparison with the PN approximation. The expanded MECO does not approach the exact MECO at high spins, showing a very unstable behaviour for odd PN orders (the upper branch of odd PN orders corresponds actually to a maximum of the energy). Therefore, any attempt to obtain a well-defined MECO for the PN energy at odd orders will fail with the current method.

to have a very unstable MECO that is often far away from the exact Kerr ISCO. It is necessary to avoid the test-mass truncation in order to obtain a stable MECO which is well-defined for any PN order and any spin value. In this section we extend an idea in [125] of a hybrid energy to the case of spinning objects, to obtain a well-defined MECO condition for all spin values.

Consider a hybrid energy given by replacing the test-mass expansion in the PN energy (up to the PN order known) with the exact Kerr solution:

$$\begin{aligned}
 E^h &= E^{\text{Kerr}} + \frac{E^{n\text{-PN}}}{\eta} - \left( \sum_{x=0}^{x=2n} E^{\text{Kerr}}(v^x) \right) \\
 &= E^{\text{Kerr}} - \frac{1}{2} v^2 \left\{ -\frac{\eta}{12} v^2 + \left( \frac{19}{8} \eta - \frac{\eta^2}{24} \right) v^4 \right. \\
 &\quad + \left[ \left( \frac{34445}{576} - \frac{205\pi^2}{96} \right) \eta - \frac{155}{96} \eta^2 - \frac{35}{5184} \eta^3 \right] v^6 \\
 &\quad - \left[ \left( \frac{123671}{5760} - \frac{9037\pi^2}{1536} - \frac{1792}{15} \ln 2 - \frac{896}{15} \gamma_E \right) \eta \right. \\
 &\quad \left. + \left( \frac{498449}{3456} - \frac{3157\pi^2}{576} \right) \eta^2 - \frac{77}{31104} \eta^4 - \frac{448}{15} \eta \ln v^2 \right] v^8 \\
 &\quad \left. + \left[ E_{SO} - \chi \left( \frac{8}{3} v^3 + 8v^5 + 27v^7 \right) \right] \right\}
 \end{aligned}$$

$$+ \left[ E_{\text{SS}} + \chi^2 v^4 + \frac{65}{18} \chi^2 v^6 + \frac{469}{24} \chi^2 v^8 \right] \}, \quad (5.6)$$

where  $E^{\text{Kerr}}$  is the energy given in Eq. (5.2),  $n$  is the PN order chosen, and  $E_{\text{SO}}$ ,  $E_{\text{SS}} = E_{\text{SS}}^{2\text{PN}} + E_{\text{SS}}^{3\text{PN}} + E_{\text{SS}}^{4\text{PN}}$  are the spinning terms of the PN energy given in Appendix C (recall the relation  $S_i = \chi_i m_i^2$ ). Here we do not include the spin-cubic term because its effect is unnoticeable for our purposes. The spin-quartic term, given in Eq. (C.9), vanishes for the systems we are considering.

When including single-body Kerr terms in a two-body energy, the choice of the spin  $\chi$  that comes from the Kerr energy is not unique. Ideally, one would want a spin that keeps the energy symmetric under exchange  $1 \leftrightarrow 2$ . Motivated by [142], [143], we use the mass-weighted effective spin parameter introduced in [144]

$$\chi_{\text{eff}} = \frac{\chi_1 m_1 + \chi_2 m_2}{m_1 + m_2}. \quad (5.7)$$

This effective spin parameter reduces to a single black hole spin in the test-mass limit, and is typically used in gravitational-wave astronomy [51].

The hybrid energy in Eq. (5.6) has a minimum for any known PN order and for any spin value, as can be seen in Fig. 5.4. There is still a difference between PN orders, although the 3.5PN spin-orbit term seems to push the minimum to lower velocities with respect to the energies up to even PN orders in the region of positive spins. In the absence of higher order spinning terms, one cannot conclude if spin-orbit terms will

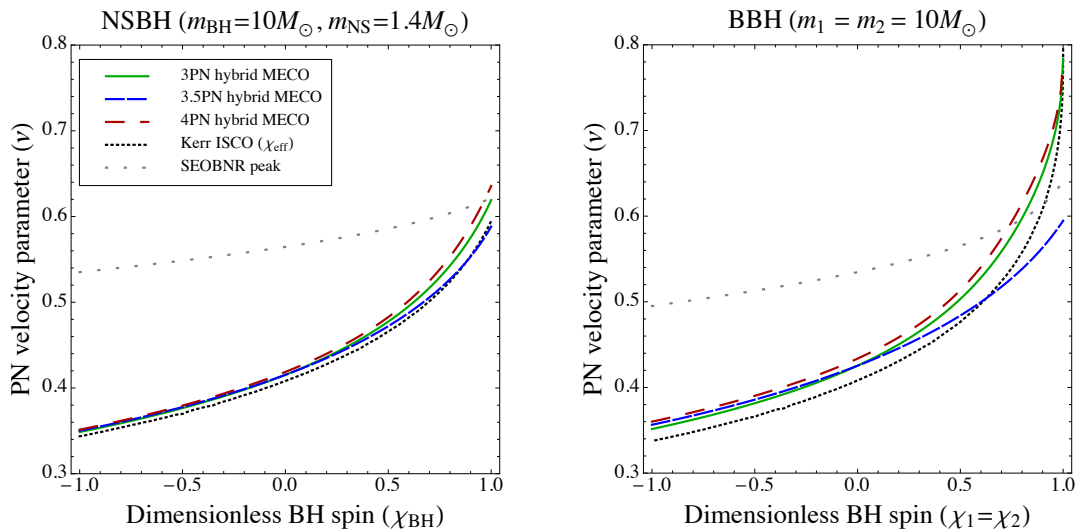


Figure 5.4: MECO of the hybrid energy given in Eq. (5.6) as function of the PN velocity parameter,  $v$ . Dotted lines represent the Kerr ISCO, with  $\chi = \chi_{\text{eff}}$ , and the SEOBNR peak. Continuous and dashed lines represent the minimum of the hybrid energy up to different PN orders. There is still a clear difference between odd and even PN orders at high aligned spins. However, the energy always reaches a minimum, suggesting that the hybrid MECO is a better description of the end of the inspiral than the MECO of the pure PN energy.

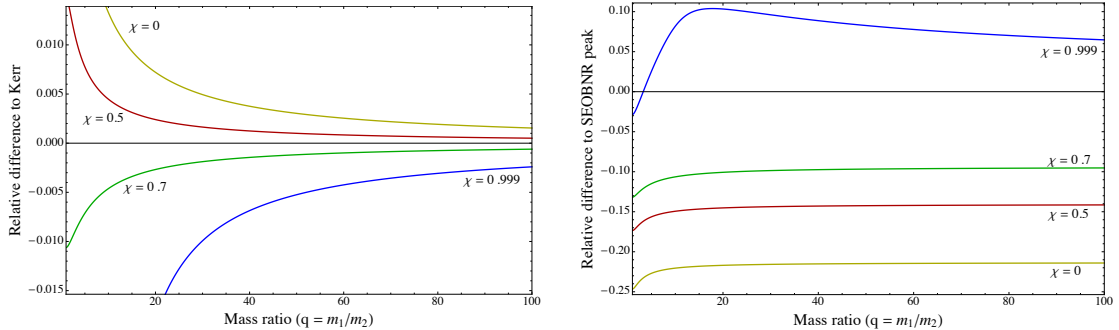


Figure 5.5: Relative difference, for BBH with mass ratios up to  $q = 100$ , between the PN velocity parameter of the hybrid MECO at 3.5PN order and (top) of the exact Kerr MECO,  $(v_{\text{hybrid}} - v_{\text{Kerr}})/v_{\text{Kerr}}$ , and (bottom) of the SEOBNR peak,  $(v_{\text{hybrid}} - v_{\text{SEOBNR}})/v_{\text{SEOBNR}}$ . The two black holes are considered to have equal spin,  $\chi_1 = \chi_2 = \chi$ . Only aligned spins (positive) are shown, because anti-aligned spins behave similarly to the spin zero case.

always have this effect on the hybrid MECO. Nevertheless, due to the stability of this approach at any known PN order and at any spin value, we suggest the use of the hybrid MECO as a PN approximation to the end of the inspiral phase. More specifically, we suggest the use of the 3.5PN hybrid MECO, which is more conservative than the even orders at higher spins, and, for the binary systems considered here, is always below the SEOBNR peak.

The relative difference in the velocity between the exact Kerr MECO and this new hybrid MECO at 3.5PN order is shown in the left panel of Fig. 5.5 as a function of the mass ratio. The deviation from the exact Kerr ISCO depends on the mass ratio: increasing the mass ratio leads to higher similarity with the exact Kerr ISCO. Therefore, the difference tends to zero asymptotically. The right panel of Fig. 5.5 shows the relative difference in the velocity between the SEOBNR peak and the hybrid MECO. For spins  $\chi \gtrsim 0.94$ , the hybrid MECO lies above the SEOBNR peak when the mass ratio is increased. However, we do not consider this a critical defect of our model, since those parameters lie outside the calibration region of the SEOBNR model.

## 5.4 Relative SNR between inspiral templates

We have seen how the hybrid MECO termination condition differs from the Schwarzschild ISCO and other conditions in terms of the PN velocity parameter  $v$ . This velocity parameter is simply related to the orbital frequency and the observed instantaneous frequency of emitted gravitational waves. To evaluate how significant the difference between terminations is in terms of the sensitivity of ground-based gravitational wave detectors, we turn now to the question of how much of the actual inspiral signal is contained between the Schwarzschild ISCO and the hybrid MECO. This is analogous to computing the relative signal-to-noise ratio (relative SNR) between a template waveform that terminates at the hybrid MECO frequency ( $f_{\text{hM}}$ ), and a template waveform that terminates at the Schwarzschild ISCO frequency ( $f_{\text{Schw}}$ ).

The optimal SNR of a waveform  $h(t)$  is given by [145, 146]

$$\rho_{\text{opt}}(h) = \sqrt{\langle h|h \rangle}. \quad (5.8)$$

As in Chap. 2, the noise-weighted inner product  $\langle h_1|h_2 \rangle$  is defined by

$$\langle h_1|h_2 \rangle = 4 \Re \left( \int_0^\infty \frac{\tilde{h}_1^*(f)\tilde{h}_2(f)}{S_n(f)} df \right), \quad (5.9)$$

where  $\tilde{h}_i(f)$  is the Fourier transform of  $h_i(t)$  and  $*$  indicates complex conjugation.  $S_n(f)$  denotes the one-sided power spectral density of the detector's noise. When restricting attention to only the inspiral part of a signal, the upper frequency cutoff of the integral is the end of the inspiral (or the Nyquist frequency if the latter is reached first). The lower limit of the integral can be taken as the detector's effective low-frequency sensitivity limit, below which the detector is dominated by seismic noise. The relative SNR between inspiral waveforms terminating at the hybrid MECO,  $h_{\text{hM}}$ , and waveforms terminating at the Schwarzschild ISCO,  $h_{\text{Schw}}$  is therefore

$$\rho_r = \frac{\rho_{\text{opt}}(h_{\text{hM}})}{\rho_{\text{opt}}(h_{\text{Schw}})} = \sqrt{\frac{\langle h_{\text{hM}}|h_{\text{hM}} \rangle}{\langle h_{\text{Schw}}|h_{\text{Schw}} \rangle}}. \quad (5.10)$$

The Fourier domain waveform in the stationary phase approximation is given by [146]

$$\tilde{h}(f) = \mathcal{A}f^{-7/6}e^{i\Psi(f)}, \quad (5.11)$$

where  $\Psi(f)$  is the phase of the Fourier domain waveform and  $\mathcal{A}$  its amplitude. With this expression, neglecting all the post-Newtonian corrections to the amplitude, the relative SNR between both templates is given by

$$\rho_r = \sqrt{\frac{\int_{f_0}^{f_{\text{hM}}} \frac{f^{-7/3}}{S_n(f)} df}{\int_{f_0}^{f_{\text{Schw}}} \frac{f^{-7/3}}{S_n(f)} df}} \quad (5.12)$$

where  $f_0$  is the detector's low-frequency sensitivity,  $f_{\text{hM}}$  is the frequency of the hybrid MECO, and  $f_{\text{Schw}}$  is the frequency of the Schwarzschild ISCO.

Figure 5.6 shows this relative SNR as a function of the mass ratio  $q$ . The sensitivity curves used represent (i) the early runs of the Advanced LIGO generation (which we call early aLIGO), and (ii) the modelled sensitivity of the zero-detuned, high-power design of the mature Advanced LIGO (which we call ZDHP aLIGO) [147]. The relative SNR is  $\rho_r = 1$  for waveforms with  $f_{\text{hM}} \simeq f_{\text{Schw}}$ . Systems where  $f_{\text{hM}} < f_{\text{Schw}}$  ( $f_{\text{hM}} > f_{\text{Schw}}$ ) have  $\rho_r < 1$  ( $\rho_r > 1$ ).

For the NSBH systems, small mass ratios give a total mass  $M < 10M_\odot$ . At a given velocity, the frequency of the gravitational wave is inversely proportional to the total mass of the system,  $f_{\text{GW}} = v^3/(\pi M)$ . For low mass systems, therefore, the Schwarzschild ISCO and the hybrid MECO have frequencies  $f_{\text{GW}} \gtrsim 400$  Hz. Since the detectors are

most sensitive below 400 Hz, changing the waveform cutoff at such high frequencies does not result in a significant gain or loss in the SNR.

For the BBH systems, however, total masses are higher and the late inspiral frequencies lie in the region where the detectors are most sensitive. This translates into a significant SNR content between the Schwarzschild ISCO and the hybrid MECO frequencies. For sufficiently large mass ratios and positive spin values ( $\chi > 0.5$ ), most of the inspiral signal is contained between the Schwarzschild ISCO and hybrid MECO frequencies. In the case of anti-aligned spins, however, the Schwarzschild ISCO actually extends beyond the hybrid MECO and thus contains spurious inspiral signal that is unlikely to be physical.

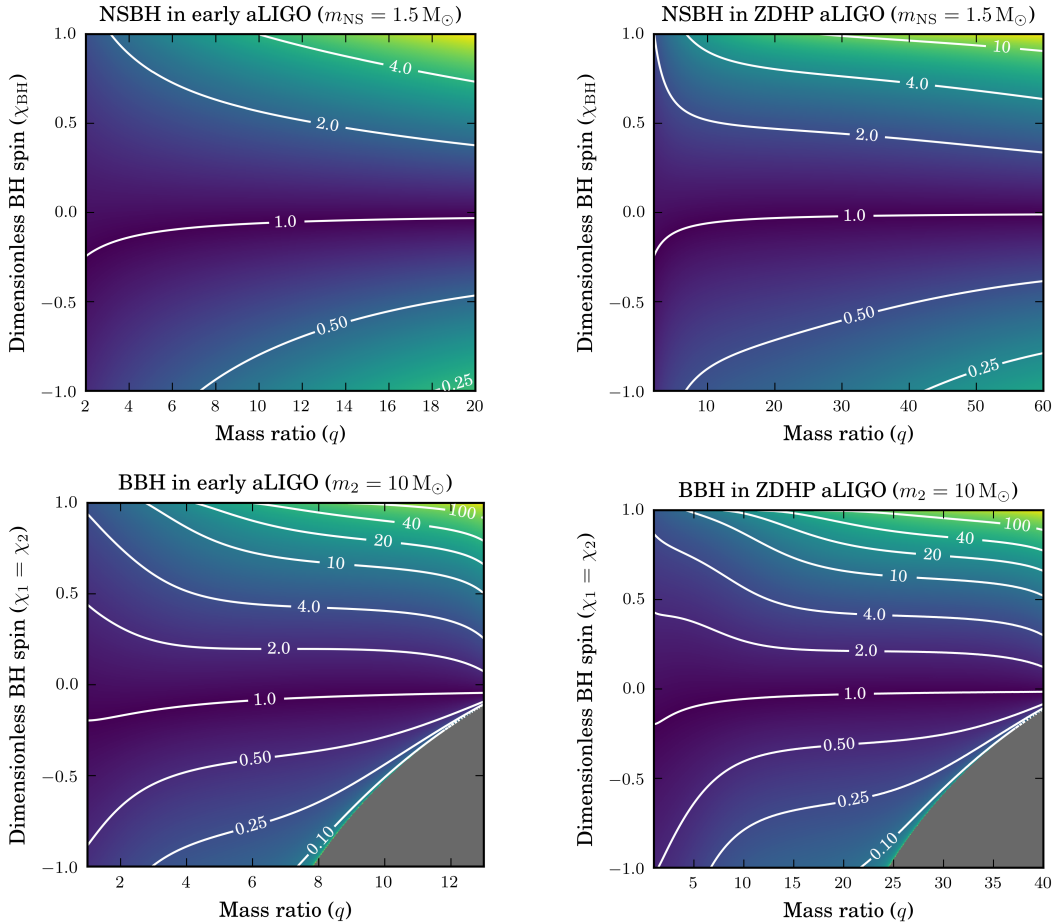


Figure 5.6: Relative SNR between inspiral signals terminating at the hybrid MECO and terminating at the Schwarzschild ISCO as a function of the spin of the black hole(s) and the mass ratio  $q$  of the two objects. The mass of one body is fixed:  $m_{\text{NS}} = 1.5M_{\odot}$  in the NSBH case and  $m_2 = 10M_{\odot}$  in the BBH case. The mass of the other body varies as  $m_1 = qm_2$ . For early aLIGO the low frequency sensitivity limit is chosen as  $f_0 = 30\text{Hz}$ , and for ZDHP aLIGO,  $f_0 = 10\text{Hz}$ . Grey regions correspond to systems where the termination frequency lies below  $f_0$ .

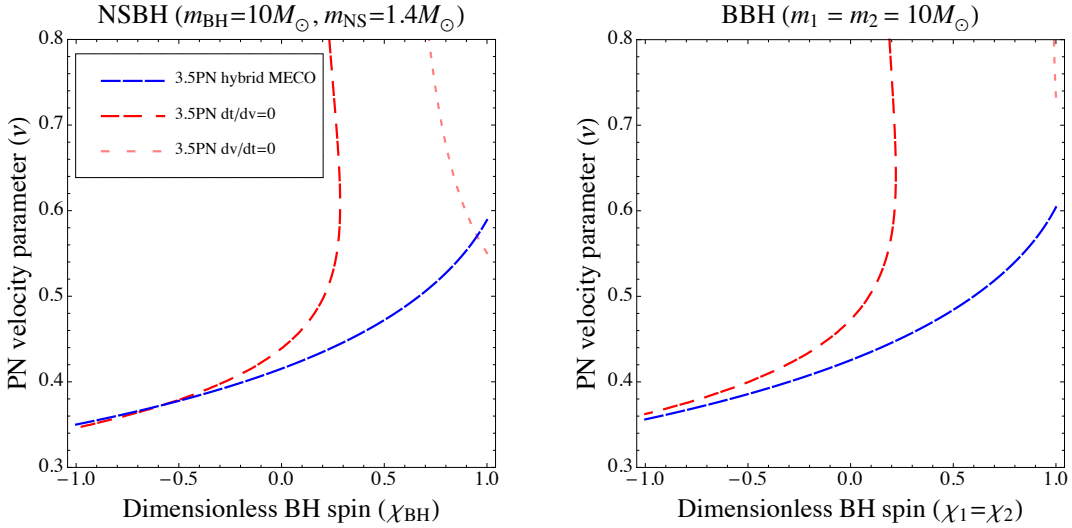


Figure 5.7: Hybrid MECO and the integrands cutoffs at the 3.5PN order. In the NSBH case, TaylorT4 breaks before the hybrid MECO at high aligned spins, and TaylorT2 at high anti-aligned spins. In the BBH case, however, the hybrid MECO is sufficient condition.

## 5.5 Application to post-Newtonian approximants

The PN energy,  $E^{\text{PN}}$ , and energy flux,  $\mathcal{F}^{\text{PN}}$ , can be used to compute the evolution of the gravitational-wave phase [90, 124] in quasi-circular inspirals. From the energy balance equation  $dE/dt = -\mathcal{F}$ , one can obtain an expression for the time evolution of the PN velocity parameter  $v$ :

$$\frac{dv}{dt} = -\frac{\mathcal{F}(v)}{E'(v)}, \quad (5.13)$$

where  $E'(v) = dE/dv$ . The gravitational wave frequency  $f_{\text{GW}}$  is related to the PN velocity parameter by  $v = (\pi M f_{\text{GW}})^{1/3}$ . The gravitational-wave phase is twice the orbital phase  $\phi(t)$ , which is given by

$$\frac{d\phi}{dt} = \frac{v^3}{M}. \quad (5.14)$$

The energy balance equation can be solved in different ways to obtain different PN approximants for the gravitational-wave phase. In this chapter, we focus on the so-called TaylorT4 [148] and TaylorT2 approximants.

The TaylorT4 approximant is obtained by expanding the ratio  $\mathcal{F}(v)/E'(v)$  to the consistent PN order and then integrating Eq. (5.13) numerically. Introducing the resulting  $v(t)$  into Eq. (5.14), the phase of the gravitational wave can be integrated.

The TaylorT2 approximant instead expands the ratio  $E'(v)/\mathcal{F}(v)$  to the consistent PN order:

$$\frac{dt}{dv} = -\frac{E'(v)}{\mathcal{F}(v)}. \quad (5.15)$$

The phase can then be obtained combining (5.14) and (5.15), and integrating

$$\frac{d\phi}{dv} = -\frac{v^3}{M} \frac{E'(v)}{\mathcal{F}(v)}. \quad (5.16)$$

Ideally, the phase is integrated up to the MECO frequency in both approximants. However, as discussed above, there are regions of the compact binary parameter space where the traditional MECO does not exist. One wants to avoid integrating beyond the range of validity of the PN approximation. Therefore, further cutoff conditions are imposed [124]: (i) the rate of increase in frequency must not decrease ( $dv/dt \geq 0$  for TaylorT4), and (ii) analogous to the previous condition,  $dt/dv \geq 0$  for TaylorT2. Consequently, the waveform might terminate before reaching the MECO (when it exists) due to these extra cutoff conditions.

The hybrid MECO proposed in Sec. 5.3 exists in any region of the parameter space. However, the approximant could still terminate before reaching the hybrid MECO if the cutoff conditions (i) and (ii) are met. Figure 5.7 shows the regions of the parameter space where the integrands become zero before reaching the hybrid MECO when including terms up to and including 3.5PN order. In the NSBH case, the  $dv/dt = 0$  condition is needed at spins above 0.9 for the TaylorT4 approximant, and the  $dt/dv = 0$  condition is needed at spins below  $\chi \simeq -0.5$  for the TaylorT2 approximant. Therefore, the use of the extra cutoff conditions will, in some occasions, still be needed.

## 5.6 Including additional physical effects to the hybrid energy

The simplicity of the hybrid energy defined in Eq. (5.6) allows for the easy addition of physical effects not included in the point-mass PN energy or the exact Kerr test-mass limit. For instance, one could consider the effects of internal structure [149] or the effect of self-force corrections [150] to see how the hybrid MECO varies under these effects. As an explicit example, here we show the variation in the end of the inspiral due to the possible tidal deformation of neutron stars.

The dynamics of NSBH binaries are influenced by the tidal deformation of the neutron star when the separation between the two bodies decreases [127, 128, 151, 152]. The magnitude of the deformation depends on the equation of state (EOS) of the neutron star and the masses and spins of the two objects. For comparable masses, the neutron star may completely disrupt before the plunge into the black hole [151]. In this case, some of the disrupted mass may become unbound [151] or form an accretion disk [153]. Such systems are of great astrophysical interest, because they provide an electromagnetic counterpart to gravitational-wave signals (e.g. short gamma-ray bursts [56, 153]).

An analytical model that accounts for the disruption of the neutron star is more difficult to define. Some works have computed leading-order terms that describe tidal deformation [127, 128]. Tidal corrections to the PN energy are a Newtonian effect that scale proportional to the 5PN order. For NSBH, where the neutron star is assumed to

be the only deformable body<sup>3</sup>, these effects are given by [127,128]

$$\begin{aligned} E_{\text{tidal}} &= -\frac{1}{2}\eta v^2 \left[ -\frac{9m_1}{m_2} \tilde{\lambda}_2 v^{10} - \frac{11m_1}{2m_2} \left( 3 + \frac{2m_2}{M} + \frac{3m_2^2}{M^2} \right) \tilde{\lambda}_2 v^{12} + \mathcal{O}(v^{14}) \right], \\ \mathcal{F}_{\text{tidal}} &= \frac{32}{5}\eta^2 v^{10} \left[ \left( \frac{18M}{m_2} - 12 \right) \tilde{\lambda}_2 v^{10} \right. \\ &\quad \left. - \frac{M}{28m_2} \left( 704 + 1803 \frac{m_2}{M} - 4501 \frac{m_2^2}{M^2} + 2170 \frac{m_2^3}{M^3} \right) \tilde{\lambda}_2 v^{12} + \mathcal{O}(v^{14}) \right], \end{aligned} \quad (5.17)$$

where  $\tilde{\lambda}_2 = \lambda_2(m_2/M)^5$ ,  $\lambda_2 = \frac{2}{3}k_2(R/m_2)^5$  is the dimensionless tidal deformability of the neutron star,  $k_2$  is the Love number of the neutron star,  $R$  is its radius, and  $m_2$  is its mass [157,158].

Since energy is absorbed by the tidal effects, the velocity at which the energy reaches its minimum will be smaller when the tidal effects are considered. Figure 5.8 shows the change in the hybrid MECO due to the tidal deformation of the neutron star. This deformation hastens the end of the inspiral phase, especially for highly aligned black-hole spins. This effect depends strongly on the EOS and the mass ratio.

The tidal terms in Eq. (5.17) do not account for complete disruption. If the neutron star disrupts before the end of the inspiral, the dynamics of the system change dramatically. If tidal disruption occurs after the end of the inspiral, or not at all, then

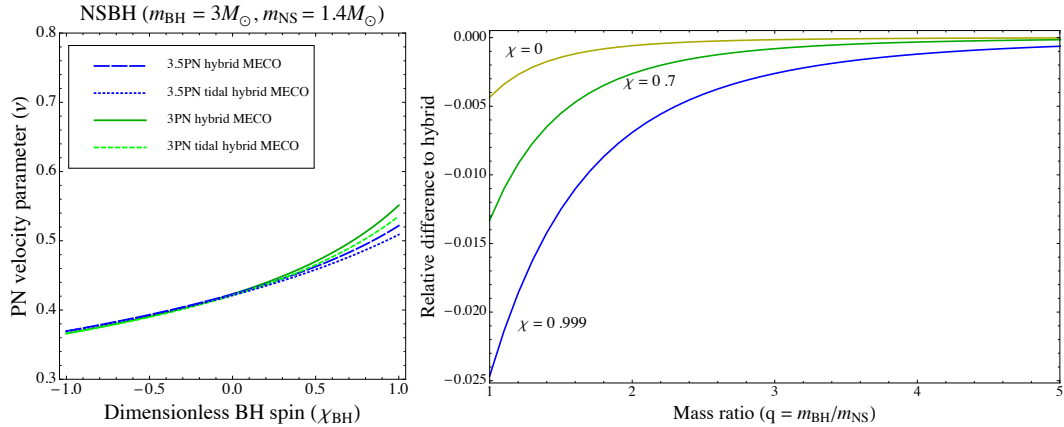


Figure 5.8: Change on the hybrid MECO due to the tidal effects given in Eq. (5.17). The neutron star's equation of state is AP4, which yields a radius  $R = 11.5$  km and a dimensionless tidal deformability  $\lambda_2 = 269.75$  [141]. (Left) Qualitative effect of the tidal terms on the hybrid MECO for a mass ratio  $q \simeq 2$ . This system clearly shows the effect at high spins. However, total disruption of the neutron star might happen before the MECO is reached. (Right) Relative difference between the hybrid MECO at the 3.5PN order with and without tidal terms,  $(v_{\text{tidal}} - v_{\text{hybrid}})/v_{\text{hybrid}}$ , for mass ratios up to  $q = 5$ . The mass of the neutron star is fixed to  $m_{\text{NS}} = 1.4M_{\odot}$  and its spin is set to zero.

<sup>3</sup>The deformability of black holes and the value of their Love numbers is still ongoing work [154,156] although it is expected to be negligible compared to the deformation of neutron stars.

the dynamics are little changed. Numerical simulations of NSBH [159, 160] provide a better understanding of the disruption mechanism. Based on the resulting numerical waveforms, studies of the end of the inspiral due to the disruption of the neutron star have been performed in [112]. It is therefore important to determine whether disruption occurs before the tidal hybrid MECO, so Fig. 5.8 also shows systems that may be tidally disrupted.

## 5.7 Conclusions

We constructed a hybrid MECO by combining the information of post-Newtonian theory with the exact Kerr solution, and showed that it can be used for binary systems with arbitrary component spins. In combination with NR simulations and full inspiral-merger-ringdown waveform models, this simple analytical approximation gives a more complete understanding of the dynamics of compact binaries.

Unlike the pure PN MECO, which does not exist for large component spins, the hybrid MECO is well-defined for any known PN order in the whole parameter space. This feature is very important for studies of the inspiral phase in real gravitational wave signals, where component spins can have a significant effect. Furthermore, the hybrid MECO is well-defined for equal-mass binaries and, by construction, reduces to the Kerr ISCO in the test-mass limit. This is in contrast to the PN ISCO condition in [118], which is well-defined only in the test-mass limit and differs from the Kerr ISCO at high spins. In addition, the method we propose can be easily updated when new post-Newtonian terms become available. Finite-mass corrections can also be introduced in the hybrid energy, as we have shown, for instance, with the tidal effects of neutron stars.

In this new era of gravitational-wave astronomy, real signals from compact binaries become available to further test the theory of General Relativity and properties of black holes. Tests that rely on measurements purely in the inspiral phase, such as measurements of the initial masses and spins, will require a well motivated cutoff condition to identify the end of the inspiral regime. Within the PN approximation scheme, the hybrid MECO proposed in this chapter shows several key advantages over traditional choices such as the Schwarzschild ISCO: the hybrid MECO is spin dependent; it exists for all known PN terms and all values of parameter space; further physical effects are readily included; it reduces to the correct extreme mass limit; and occurs before the expected peak emission of the merger. In the next chapter we will use this hybrid MECO to develop a test of the black hole area increase law with gravitational wave signals.

Furthermore, direct comparisons between the tidal hybrid MECO and the cutoff obtained from total tidal disruption models may provide more information about the end of the inspiral in systems with neutron stars. This will be important for binaries with tidally deformed or disrupted neutron stars. In this chapter we have worked only with component spins aligned or anti-aligned with the orbital angular momentum. However, the behaviour of the MECO could vary significantly for precessing systems. In the future, the hybrid MECO shall be extended to include spin-precessing terms.

# Chapter 6

## Observational tests of the area increase law with gravitational waves

The black hole area increase law [120,161] is one of the most celebrated results in exact non-linear relativity. In mergers of multiple black holes it implies that the total horizon areas should always increase, provided certain assumptions that are expected to hold for astrophysical black holes. This law suggests an analogy between the horizon area of a black hole and its entropy [162–164], and is thus one of the central results of black hole thermodynamics. The observations of gravitational waves from binary black hole coalescence events [18,50–54] open up the possibility of carrying out direct tests of this fundamental law using observational data. In this chapter we shall present a method to perform such a test based on the inspiral and on the ringdown stages of simulated binary black hole coalescences.

Gravitational-wave observations of binary black hole coalescences correspond to the inspiral of two black holes that merge together, forming a single black hole which then settles down to a stationary state by a ringdown process. The areas of the black hole horizons are not directly observable using gravitational-wave data, so here we make use of the Kerr metric to relate the black hole horizon area to its asymptotic mass  $M$  and dimensionless spin  $\chi$ . Widely separated inspiralling black holes are expected to be very well described by the Kerr metric in some neighbourhood of the horizon. Mass and spin values can be inferred for the inspiralling black holes by comparison with inspiral gravitational waveforms. The mass and spin of the final black hole can be inferred by comparison with ringdown waveforms of a single Kerr black hole.

If two initially distant Kerr black holes with areas  $A_1, A_2$  coalesce to form a final Kerr black hole with area  $A_f$ , then it follows from the area increase law that

$$A_1 + A_2 \equiv A_i < A_f. \quad (6.1)$$

Our analysis strategy is similar to the suggestion by Hughes and Menou [121], namely, use the early inspiral regime to measure the parameters of the initial black holes, and independently use the late-time ringdown regime to measure the parameters of the final black hole. The end result of the parameter estimation procedure will be a probability

distribution  $p(\Delta A)$  for the change in the area  $\Delta A := A_f - (A_1 + A_2)$ . This allows us to calculate a probability

$$\int_0^\infty p(\Delta A) d\Delta A \quad (6.2)$$

that a particular event is compatible with the area increase law.

By analysing the observed gravitational wave data for the detected events [18, 50–55], posterior distributions for the parameters of the initial and final black holes in these events have been reported in [51–54, 77]. However, these cannot be used as an independent test of the area increase law because these results use fitting formulae to obtain the final  $M_f, \chi_f$  (and thus  $A_f$ ) as functions of the initial parameters. These fitting formulae [100–102] are results of numerical relativity simulations which assume the validity of vacuum general relativity, and thus implicitly assume *a priori* the validity of the area increase law. A true direct test of the area increase law should independently obtain  $A_i$  and  $A_f$  from the observed data and then use them to verify whether or not Eq. (6.1) holds.

Similarly, tests have been designed to check the consistency between the inspiral and merger-ringdown parts of gravitational wave signals [165, 166]. When performed on gravitational-wave observations these tests have found the signals to be compatible with standard general relativity and the fitting formulae [18, 51–54]. Our proposed test here is different in that we avoid the use of fitting formulae entirely; we separate the signal in the time domain rather than the frequency domain, and crucially we avoid using data from the near merger portion of the signal. A violation of the area theorem is perhaps most likely near the merger of the two black holes where the spacetime is most dynamic. It is this region where numerical relativity simulations are critical to follow the evolution. We wish to avoid this region and infer the areas of the inspiralling black holes only from the early inspiral phase, when the two black holes are clearly separated, and the area of the final black hole only from its simple ringdown behaviour as given by the Kerr metric.

Another result that shows up naturally is an independent estimate of the energy radiated away during the merger in the form of gravitational radiation without using any of the aforementioned numerical relativity fits. Since we obtain the two initial masses and the final mass, it is straightforward to compute the difference and obtain a posterior distribution of the radiated energy. This can be compared with the numerical relativity prediction and thus offers yet another test of general relativity.

The various details involved in this calculation will be described in the following sections. The plan for the rest of the chapter is as follows. Section 6.1 introduces preliminary material and notation. Section 6.2 presents the details of the test. Sections 6.3 and 6.4 present results on simulated signals, and finally Sec. 6.5 has concluding remarks on the future prospects of this test. The work presented in this chapter, published in [122], was performed by the author together with Collin Capano, following discussions with Alex Nitz and other co-authors. Section 6.1 was written by the co-authors Badri Krishnan, Alex Nielsen, and Ofek Fischer-Birnholtz. The following sections were written jointly by the author and Collin Capano.

## 6.1 Preliminaries

### 6.1.1 Testing the assumptions

A test of the black hole area increase theorem is a test of whether the assumptions that go into the theorem's proof are valid. Any violation of area increase would be proof that at least one of the assumptions does not hold. In the test proposed here, we measure the change in area between two asymptotic states, well before the merger and well after the merger, where the relevant black holes can be approximated by Kerr black holes. It is therefore not a test that the total horizon area is increasing at all times during the coalescence. However, the change in area between these asymptotic states can be written as a time integral over the instantaneous rate of area change and hence our test depends on the assumptions used to show that the rate of area change should always be positive. A decrease in the area between asymptotic states would be a demonstration that at least one of these assumptions was violated (although clearly if the overall area change is positive this does not necessarily preclude that the area was decreasing at some point during the merger, or indeed that some of the assumptions were mildly violated but the area still increases).

There exist in the literature several different proofs of the area increase law that can be classified according to which type of horizon they refer to, the main classes being event horizons and quasi-local horizons based on the notion of marginally trapped surfaces/apparent horizons. The proofs of the area increase law make different assumptions in either of the two cases. In the asymptotic states considered here, both when the two black holes are far apart and at late times when the final black hole is in equilibrium, there is no difference between the areas of the event horizon or quasi-local horizons. Thus if the overall area change is measured to be negative then this would be a violation both of proofs using event horizons and of those using quasi-local horizons, and therefore at least one of the common assumptions would most likely be violated (although it is logically possible that different assumptions are violated in the two cases).

Proofs of the area increase law for event horizons (see e.g. [14]) rely on three main ingredients:

- i) The null curvature condition, which says that the Ricci tensor  $R_{\mu\nu}$  must satisfy  $R_{\mu\nu}\xi^\mu\xi^\nu \geq 0$  for any null vector field  $\xi^\mu$ . While the area theorem does not depend on the Einstein equations, in Einstein's general relativity this assumption is equivalent to the requirement that the stress-energy tensor  $T_{ab}$  satisfies the null energy condition  $T_{\mu\nu}\xi^\mu\xi^\nu \geq 0$ .
- ii) Asymptotic flatness and additional global conditions which ensure that the space-time outside the black hole (including the event horizon) must be predictable from suitable data on a Cauchy surface. In particular, these conditions rule out the presence of naked singularities (cosmic censorship).
- iii) The proofs use properties of the intrinsic geometry of event horizons and in particular the geodesic deviation equation for null geodesics on the event horizon.

It can be shown that given the previous conditions, the congruence of null geodesics generating the event horizon cannot have negative expansion anywhere and the area is

always increasing. The most general statement and proof of the area increase law is by Chrusciel et al [167]. This includes the cases when the event horizon is not smooth<sup>1</sup> and also applies to non-zero values of the cosmological constant. As expected, cosmic censorship and the null curvature condition are still required.

Since gravitational wave observations only probe a finite region of spacetime, it would seem unreasonable that we could say anything definite about naked singularities *anywhere* in the universe based on these observations. This is also an artefact of the well known global and teleological features of the event horizon. Thus, should we have observational evidence that the area increase law is violated, we can expect the energy condition to be the main culprit.

This can be seen clearly in alternate formulations of the area increase law. It is possible to formulate the area increase law for black holes in a quasi-local framework, without these global assumptions, relying on marginally trapped surfaces and the associated notions of dynamical and trapping horizons [170, 172]. Using the Einstein equations on the horizon, it is possible to obtain a “physical process” version of the area increase law which relates the increase in area to the fluxes of in-falling matter and radiation [173]. These fluxes are manifestly positive if the dominant energy condition holds.

It is in fact known that energy conditions can be violated in nature by a number of mechanisms [174]. The question of whether sufficient energy condition violation occurs during a binary black hole merge to cause the horizon area to decrease is one of the main motivations for our test.

In our test of the area increase law, we shall assume that the black hole no-hair theorem holds, i.e. that any astrophysical *stationary* black hole is completely described by its mass  $M$  and angular momentum  $J$  and given by the Kerr solution. This applies to the two initial black holes and to the final black hole formed as a result of the coalescence. Thus, any cross-section of the black holes at early and late times has an area  $A$  given by

$$A = 8\pi M^2 \left( 1 + \sqrt{1 - \chi^2} \right). \quad (6.3)$$

Here  $\chi = J/M^2$  is the dimensionless spin, which can take values  $-1 \leq \chi \leq 1$ . It is an important goal to test whether the no-hair theorems are valid and in fact, there is a large body of work on possible tests of the black hole uniqueness theorem from binary black hole observations [43, 99, 175–178]. It would be preferable to drop this assumption and design a joint test of both the area increase law and the uniqueness theorems, but this is beyond the scope of the present paper. It is important for us to clearly identify the parts of the waveform when we cannot assume the no-hair theorem to hold and this will be addressed below in Secs. 6.2.2 and 6.2.3.

As shown by Hawking [120], the constraint derived from the area increase law can be used to bound the amount of energy emitted during the coalescence process. For a coalescence of non-spinning, equal-mass black holes, this bound limits the emitted energy

---

<sup>1</sup>Generically event horizons are not smooth; cusps are formed when null geodesics enter the horizon [168]. Numerical relativitists assume that the horizon is regular except for a finite number of such cusps (see e.g. [169]).

to be no more than about 29% of the initial rest-mass energy of the two black holes (see also [179]). Numerical simulations of black hole collisions show that in reality the amount of energy radiated by gravitational waves is considerably less than this theoretical upper bound [180].

### 6.1.2 Estimating the parameters

As we saw in Chap. 1, the transverse-traceless part of the gravitational perturbation  $h_{\mu\nu}$  can be written in terms of two polarisations:

$$h_+(t) = A_+(t) \cos \Phi(t), \quad (6.4)$$

$$h_\times(t) = A_\times(t) \sin \Phi(t). \quad (6.5)$$

The response of an interferometric detector to this wave depends on the relative orientation between the wave frame and the detector frame and thus is specified by three angles. Recall from Chap. 1 that the strain  $h(t)$  observed by the detector is given by

$$h(t) = F_+(\alpha, \delta, \Psi) h_+(t) + F_\times(\alpha, \delta, \Psi) h_\times(t), \quad (6.6)$$

with the antenna pattern functions  $F_{+,\times}$  defined in Eqs. (1.18) and (1.19). Here, instead of the horizontal coordinate system given by the altitude and azimuth angles  $(\theta, \phi)$ , we use the equatorial coordinate system defined by the declination  $\delta = \pi/2 - \theta$  and the right ascension  $\alpha = \phi - \text{GMST}$  angles, with GMST the Greenwich Mean Sidereal Time of the observation [181].

We estimate the source parameters of a gravitational wave signal using Bayesian inference, which was the method used to estimate the parameters of GW150914 and all subsequent events [77]. The principles of Bayesian inference were summarised in Chap. 4. As a reminder, the posterior distribution  $p(\vec{\vartheta}|s, h)$  of a set of parameters  $\vec{\vartheta}$ , given the data  $s(t)$  and a waveform model  $h(t)$ , is given by the likelihood function  $\mathcal{L}(s|\vec{\vartheta})$  times a prior probability distribution  $p(\vec{\vartheta}|h)$ . The prior represents our knowledge or belief of  $\vec{\vartheta}$  before observing the data. In a network of  $N$  gravitational-wave detectors containing uncorrelated stationary Gaussian noise, the likelihood function is:

$$\mathcal{L}(s|\vec{\vartheta}) = \exp \left[ -\frac{1}{2} \sum_{a=1}^N \langle s_a - h_a(\vec{\vartheta}) | s_a - h_a(\vec{\vartheta}) \rangle \right], \quad (6.7)$$

where  $s_a$  is the data in each detector and  $h_a$  is the model waveform (or template) as it would be observed in each detector. Recall from the previous chapters the noise-weighted inner product:

$$\langle x, y \rangle \equiv 4\Re \left( \int_0^\infty \frac{\tilde{x}_a^*(f) \tilde{y}_a(f)}{S_n^{(a)}(f)} df \right). \quad (6.8)$$

## 6.2 Method

Normally, when analysing the entire signal (and assuming the detector noise truly is stationary and Gaussian), the parameter estimates produced by the method described in Sec. 6.1.2 will be unbiased. In other words, if the source distribution is the same as the prior, then we can expect that a signal’s true parameters will lie within the  $X\%$  credible interval  $X\%$  of the time.

However, the method described in Sec. 6.1.2 will yield biased estimates if a parameter-dependent cut is applied to the template waveforms [182], as we wish to do here. This is because Eq. (6.7) is derived assuming that the template is a model for the entire signal; i.e.,  $\mathcal{L}(s|\vec{\vartheta})$  is maximised for parameters that best match the signal averaged over the entire bandwidth of the detector. Here, however, we wish to find the parameters that best-match the signal only over a limited portion of the signal, while ignoring the rest. Crucially, the onset and duration of the part that we wish to exclude — the merger — is dependent on the signal’s source parameters. Since this additional, parameter-dependent condition is not included in  $p(\vec{\vartheta}|s, h)$ , a naïve application of Eq. (6.7) results in biased measurements, as we will see below.

Further complicating our efforts is our desire to excise a part of the signal in the time domain rather than the frequency domain. As discussed below, this effectively couples the sky location of the signal to the measurement of the initial and final masses and spins.

In the following we describe a method to overcome these challenges. To illustrate and test the method, we simulate a signal using a publicly available waveform produced by the SXS collaboration [183, 184]. We choose a non-spinning, equal-mass binary black hole<sup>2</sup> with total mass  $M = 70M_{\odot}$ .<sup>3</sup> The signal, which is similar to a signal like GW150914, is injected in zero noise at a luminosity distance  $D_L = 500$  Mpc.

We compare results using two different detector sensitivities: the PSD published in the LIGO Open Science Centre [105] for GW150914, which is representative of Advanced LIGO’s first observing run, and the zero-detuned high-power (ZDHP) PSD [185], which is representative of LIGO’s expected sensitivity in the coming years. In this analysis we only consider the two LIGO detectors. However, the method can be trivially expanded to include any number of detectors.

To evaluate Eq. (6.7) over a large parameter space and obtain an estimate for  $p(\vec{\vartheta}|s, h)$ , we use the PyCBC Inference framework. As we mentioned in Chap. 4, this is a python-based pipeline similar to the LALInference pipeline [186] used to infer the parameters of published gravitational waves. PyCBC Inference supports multiple stochastic sampling engines. In this study we use `kombine` [95], which is an MCMC sampler that uses an ensemble of Markov chains (or walkers) to efficiently estimate  $p(\vec{\vartheta}|s, h)$ .

---

<sup>2</sup>Numerical waveform SXS:BBH:0066, Lev5

<sup>3</sup>Since we use waveform templates that do not include sub-dominant modes, we select only the 22 mode of the numerical waveform. This is a sensible approach because higher modes are not expected to be detectable with current sensitivities [99, 104].

### 6.2.1 The effect of sky location

An integral part of our analysis is separating the inspiral part to estimate the initial parameters of the binary and the ringdown part to estimate the parameters of the final black hole. The templates used for the parameter estimation are terminated (or started) at a specific time. This method complicates the issue of dealing with the sky location since the sky location affects the arrival time of the signal in the detectors.

We have found that if the sky location is allowed to vary in the MCMC, the terminated templates will favour sky locations that get them closer to the merger, yielding biased results. One could fix the sky location to a single point if it were known. However, we do not expect to measure the sky location of a binary black hole merger to sufficient precision with the current network of gravitational-wave detectors for this approach to work. Indeed, when doing the ringdown analysis, we have found that choosing different fixed points drawn from within the 50% credible interval of the sky location produced by a full inspiral-merger-ringdown analysis yields statistically significant different estimates of the final mass and spin. Thus picking a single point for the sky location when one is not actually known will result in an underestimate of our uncertainty, and a potential bias of these parameters.

To account for this uncertainty, we fix the sky location to a distribution rather than a single point when doing the inspiral and ringdown analyses. We do this by assigning each walker in our MCMC to a different right ascension and declination. These locations are drawn from a given sky map that quantifies the uncertainty in the event's location. The walker's positions in the sky remain fixed throughout the entirety of the parameter estimation routine. This way, we include all the information obtained from allowing the sky location to vary without forcing the entire parameter estimation analysis to remain on one fixed point.

We use the same sky locations for the inspiral and ringdown analysis. After evolving the MCMC until it is burned in, each walker in the inspiral (ringdown) analysis produces a point estimate of the initial (final) area. Taking the estimates over all of the walkers produces a distribution of areas. When taking the difference in areas, we only compare point estimates between the same sky locations in both runs. Thus, the inspiral and ringdown analyses are independent in all parameters except for the sky location.

To produce a sky map for this study, we first perform the parameter estimation analysis on the full signal, using full inspiral-merger-ringdown IMRPhenomD templates [59, 187]. Figure 6.1 shows the marginalised posterior distribution of the right ascension ( $\alpha$ ) and declination ( $\delta$ ) obtained from this analysis. We only use the sky-location information from this analysis; no information regarding the GW parameters  $\vec{\vartheta}$  are kept. Here, we have restricted our analysis to the two LIGO detectors. However it is trivial to include a third detector, if available, to improve our measurement of the sky location [54, 55].

Since the sky location relies primarily on the time of arrival of the signal at different detectors, it is possible to estimate the sky location using searches that do not use any waveform models from general relativity. For example, a sky map produced using the coherent Wave Burst pipeline [188] was published with GW150914 [105]. The sky map produced by this pipeline may be used when applying our test to real events.

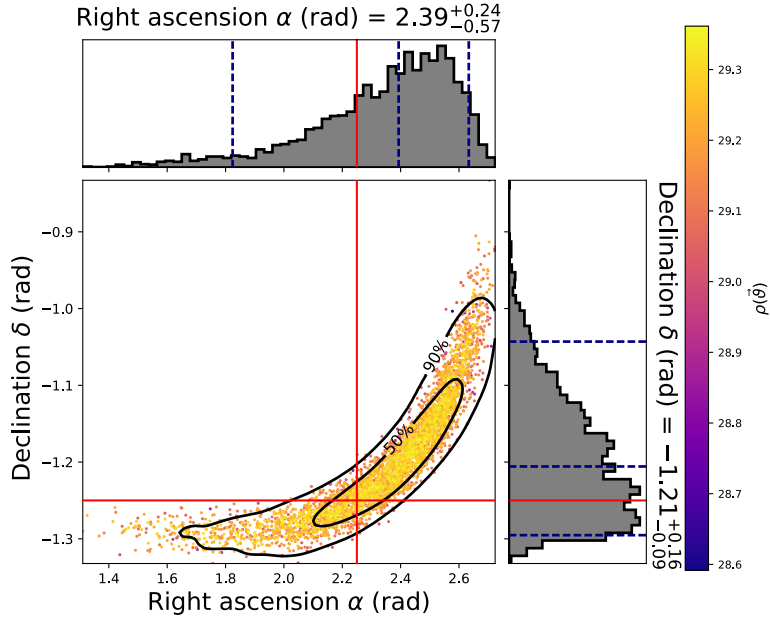


Figure 6.1: Posterior distribution for the sky location obtained from the full simulated signal. The colorbar shows the signal-to-noise ratio (SNR), which is a function of the likelihood, and the red lines indicate the values that were injected. The centre and outer dashed lines in the histograms represent the median value and the 90% credible interval, respectively. These correspond to the values and the errors given on top of the histograms.

### 6.2.2 The inspiral analysis

The initial parameters ought to be measured from the inspiral part of the waveform, with no assumptions or input from the merger or ringdown. Ideally, one would use post-Newtonian waveforms [189]. However, full inspiral-merger-ringdown waveforms such as the IMRPhenomD family [59,187] have better agreement with numerical relativity waveforms at higher inspiral frequencies. We shall use IMRPhenomD waveforms terminated at the end of the inspiral to exclude the highly dynamical merger phase and guarantee that the inspiral analysis is completely independent from the merger and ringdown. For compact binaries with arbitrary masses and spins, the hybrid minimum energy circular orbit (hybrid MECO) [129] is a proxy for the end of the inspiral. The hybrid MECO depends on the mass ratio of the binary and on the spins of the black holes, and is symmetric under exchange of the individual objects' parameters.

Naïvely, one might think that to exclude the merger phase from the analysis, we need only to terminate the templates at the time at which they pass through hybrid MECO. However, while this excludes the merger dynamics in the templates, it does not exclude the merger in the signal. This results in templates with higher spin and mass matching the signal better than the template that has the same mass and spin of the signal, leading to biased results. This is because the hybrid MECO of these templates occurs at a higher frequency. Effectively, these templates are able to see more of the

signal; the additional signal-to-noise ratio (SNR) they gain in doing so is enough to offset any mismatch these templates have with the signal at lower frequencies.

To recover the correct masses and spins it is necessary to exclude the merger dynamics in both the templates and the signal. However, because the intrinsic parameters of the signal are unknown, the time at which the signal passes through hybrid MECO is also unknown. To estimate this time we choose a grid of times  $t_{\text{grid}} < t_{\text{ref}}$ , where  $t_{\text{ref}}$  is a fiducial time chosen arbitrarily in the proximity of the expected coalescence time of the binary. We perform an independent parameter estimation analysis for each grid time. In each analysis, we apply a taper function to the templates in the time domain that goes to zero at a time  $t_{\text{taper}}$ . The taper time is varied across parameter space and between detectors. Specifically, for a given set of parameters  $\vec{\vartheta}$  and a detector D,

$$t_{\text{taper}} = \min \left[ t_{\text{grid}} + \delta t(\alpha, \delta; D), t_{\text{hMECO}}(\vec{\vartheta}) \right], \quad (6.9)$$

where  $t_{\text{hMECO}}$  is the time at which the template goes through hybrid MECO. The  $\delta t(\alpha, \delta; D)$  is an offset applied to account for the arrival time uncertainty in each detector arising from the uncertainty in sky location.

When doing the analysis we found that whitening the template before tapering yielded better results than simply applying the taper to the waveform and then whitening. That is, we replace the full IMR template  $h$  with:

$$h'(t) = w(t; t_{\text{taper}})[h * \widetilde{A^{-1}}](t),$$

where  $\widetilde{A^{-1}}(t)$  is the inverse Fourier transform of  $1/\sqrt{S_n(f)}$ ; the  $*$  indicates convolution. We use half a Kaiser window with a duration of 10 ms and shape parameter  $\beta = 8$  [190] for the taper function  $w(t; t_{\text{taper}})$ . A duration of 10 ms is used because the whitening filter  $\widetilde{A^{-1}}(t)$  effectively goes to zero on this time scale, ensuring that times  $t > t_{\text{taper}}$  are minimally coupled to times  $t < t_{\text{taper}}$  via the convolution. The whitened, tapered template  $h'(t)$  is filtered with the whitened data.

The grid time  $t_{\text{grid}}$  prevents the templates from matching the merger dynamics in the signal. For  $t_{\text{grid}}$  times later than  $t_{\text{hMECO}}$ , results are influenced by the dynamic merger phase and the posterior distributions yield biased results. As  $t_{\text{grid}}$  approaches  $t_{\text{hMECO}}$  of the signal, the posterior settles around the parameters of the signal. For  $t_{\text{grid}}$  times earlier than the signal's  $t_{\text{hMECO}}$ , the posterior remains in the same region of parameter space, though it begins to widen due to the decreasing SNR. Therefore, the transition time between the moving and the growing posterior distributions yields the best point at which to calculate the initial areas.

It is thus clear that to estimate the transition time, we need to study how the posterior distributions change as  $t_{\text{grid}}$  is varied. A general notion of the divergence between two probability distributions  $p_1(x)$  and  $p_2(x)$  is provided by the Kullback-Leibler (KL) divergence (see e.g. [191]), which for discrete distributions is defined as

$$D_{KL}(p_1 || p_2) = \sum_x p_1(x) \log \frac{p_1(x)}{p_2(x)}. \quad (6.10)$$

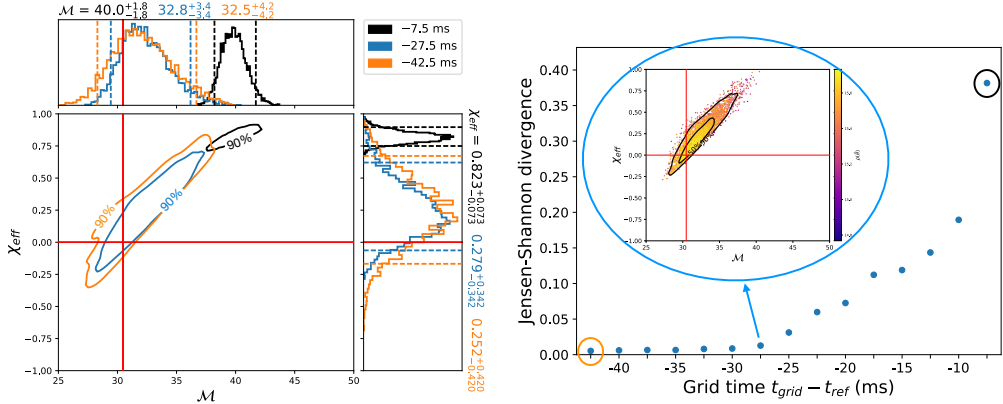


Figure 6.2: (Left) Posterior distribution of the chirp mass and the effective spin obtained from three different runs. The red cross indicates the injected values. (Right) Jensen-Shannon divergence between consecutive grid runs and resulting posterior distribution for the chosen transition time (in this case,  $t_{\text{grid}} - t_{\text{ref}} = -27.5$  ms). The  $x$ -axis indicates the corresponding time  $t_{\text{grid}}$  and the JS divergence is calculated between the posterior distributions at  $t_{\text{grid}}$  and  $t_{\text{grid}} + \Delta t$ , where  $\Delta t = 2.5$  (ms). The coloured circles indicate the times corresponding to the posterior distributions in the left figure.

However  $D_{KL}(p_1||p_2)$  is not symmetric, i.e.  $D_{KL}(p_1||p_2) \neq D_{KL}(p_2||p_1)$ . In particular,  $D_{KL}$  cannot be viewed as a distance between probability distributions.  $D_{KL}$  is an appropriate divergence to use when one of the distributions is privileged for some reason.

In our case, we have no reason to distinguish different values of  $t_{\text{ref}} - t_{\text{grid}}$  and thus we choose to use instead the Jensen-Shannon (JS) divergence. Given two probability distributions  $p_1$  and  $p_2$ , the JS divergence is a symmetric and smooth version of the KL divergence  $D_{KL}(p_1||p_2)$ :

$$D_{JS}(p_1||p_2) = \frac{1}{2}D_{KL}(p_1||q) + \frac{1}{2}D_{KL}(p_2||q), \quad (6.11)$$

where  $q = \frac{1}{2}(p_1 + p_2)$ . It has been shown that  $D_{JS}$  can be turned into a distance measure between probability distributions [192].

Figure 6.2 shows the JS divergence between the posterior distribution of the analysis at  $t_{\text{grid}}$  and the analysis at  $t_{\text{grid}} + \Delta t$ , which we have chosen to be  $\Delta t = 2.5$  ms. Since we are only interested in the masses and spins of the black holes, we compute the JS divergence using the 2D marginalised distribution of chirp mass  $\mathcal{M} = (m_1 m_2)^{3/5}/M^{1/5}$  and effective spin  $\chi_{\text{eff}} = (m_1 \chi_1 + m_2 \chi_2)/M$ . While the posterior distribution is still moving, the JS divergence is changing significantly. The transition time is given by the maximum inspiral (minimum ringdown) grid time where the JS divergence is still roughly constant. From Fig. 6.2, the transition time is clearly seen to be at the time  $t_{\text{grid}} = t_{\text{ref}} - 27.5$  ms. At times closer to the merger, the difference between consecutive JS divergences increases significantly.

In doing the analysis shown in Fig. 6.2, we vary the two component masses  $m_{1,2}$ , two component spins  $\chi_{1,2}$ , luminosity distance  $D_L$ , inclination  $\iota$ , polarisation  $\Psi$ , coalescence

phase  $\phi_c$ , and the template’s coalescence time  $t_c$ . We use uniform priors for all of these parameters. The prior range for the parameters of interest is  $m_i \in [10, 80) M_\odot$  and  $\chi_i \in [-0.9895, 0.9895)$ . This is the same prior that was used in the analysis of GW150914 [77].

### 6.2.3 The ringdown analysis

The late ringdown phase is well described through perturbation theory. Assuming that the final object is a Kerr black hole, the ringdown signal consists of a sum of exponentially damped sinusoids [36]. For the ringdown analysis, we use the waveform template defined in Chap. 4. Throughout this chapter we use only the fundamental mode ( $\ell = m = 2, n = 0$ ). However, the methods presented here can be extended to multi-mode ringdowns once the detectors’ sensitivities allow the detectability of higher order modes.

The ringdown template assumes  $h(t) = 0$  before the start of the damped sinusoid, but it is unknown in the data when the signal waveform starts behaving like a pure damped sinusoid. Same as for the inspiral phase, we choose a grid of times  $t_{\text{grid}} > t_{\text{ref}}$  and perform the ringdown analysis for each time separately, where  $t_{\text{ref}}$  is the same fiducial time used for the inspiral analysis. Times closer to the coalescence of the signal will again show biased results. If  $t_{\text{ref}}$  is after the coalescence time of the signal, we might have to use a few times  $t_{\text{grid}} < t_{\text{ref}}$  to find the transition time. Figure 6.3 shows the resulting JS divergence between the posterior distribution of the analysis at  $t_{\text{grid}}$  and the analysis at  $t_{\text{grid}} + \Delta t$ , which for the ringdown analysis we have chosen to be  $\Delta t = 0.5$  ms. The JS divergence is computed using the 2D marginalised distribution of final mass  $M_f$  and final spin  $\chi_f$ . The transition time in the ringdown analysis happens at the time  $t_{\text{grid}} = t_{\text{ref}} + 0.5$  ms.

We find that it is necessary to zero out the data prior to the grid time in order to accurately recover the final mass and spin using the damped sinusoid. This is different than the inspiral analysis, in which only the templates were modified. As discussed above, the time domain representation of the whitening filter  $\widetilde{A^{-1}}(t)$  has non-zero support on time scales  $\mathcal{O}(\text{ms})$ . This is significant in the ringdown analysis, in which differences of a few milliseconds can have large effects on the estimated parameters. Namely, the convolution of the whitening filter with the signal in Eq. (6.8) couples information from the merger with the post-merger ringdown. Since the damped sinusoid is simply zero prior to its onset, the whitening filter has a different effect on it. Thus, even if the template and the post-merger signal are exactly the same prior to whitening, they are different afterward. This difference particularly biases the recovered damping time, which in turn affects the estimated final mass and spin. Zeroing out the data prior to whitening decouples the whitened signal’s merger and ringdown, and causes the whitening filter to affect the signal and template in the same way, correcting the bias.

The variable parameters for the ringdown analysis are the central frequency  $f_{220}$ , damping time  $\tau_{220}$ , amplitude  $A_{220}$ , phase  $\beta_{220}$ , inclination  $\iota$  and polarisation  $\Psi$  (we drop the 220 label from now onwards). We use uniform priors for all of these parameters. Using the fitting formulae in [103], one can obtain the final black-hole’s mass  $M_f$  and spin

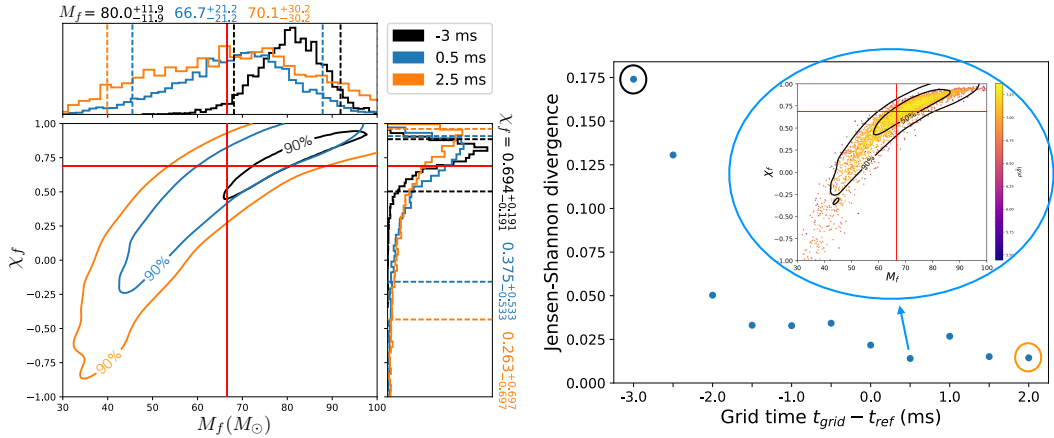


Figure 6.3: (Left) Posterior distribution of the final mass  $M_f$  and the final spin  $\chi_f$  obtained from three different runs. The red cross indicates the injected values. (Right) Jensen-Shannon divergence between consecutive grid runs and resulting posterior distribution for the chosen transition time (in this case,  $t_{\text{grid}} - t_{\text{ref}} = 0.5$  ms). The  $x$ -axis indicates the corresponding time  $t_{\text{grid}}$  and the JS divergence is calculated between the posterior distributions at  $t_{\text{grid}}$  and  $t_{\text{grid}} + \Delta t$ , which in this case is  $\Delta t = 0.5$  ms. The coloured circles indicate the times corresponding to the posterior distributions in the top figure.

$\chi_f$  from the ringdown frequency and damping time. The prior range for the parameters of interest is  $f \in [20, 1024]$  Hz and  $\tau \in [0.1, 100]$  ms, with the further constraint that  $f$  and  $\tau$  have to yield physical masses and spins (i.e.  $M_f > 0$  and  $-1 < \chi_f < 1$ ).

### 6.3 Combined results

A visual representation of the maximum posterior (MAP) waveforms resulting from the separated parameter estimation analyses is shown in Fig. 6.4, with the template waveforms plotted on top of the detectors' whitened strains. The probability distribution for the change in the area is obtained by combining the posterior distributions of the initial and final parameters from the selected inspiral and ringdown results.

The simulated binary black hole signal used in this paper is bound to agree with the area theorem by design. Using the fitting formulae in [187] we can estimate the expected area increase for the signal. Two non-spinning black holes with masses  $m_1 = m_2 = 35M_\odot$  yield a final black hole with mass  $M_f \simeq 66.6M_\odot$  and spin  $\chi_f \simeq 0.69$ , which translates into an expected area increase  $A_f/A_i \simeq 1.56$ .

The left panel in Fig. 6.5 shows the measured area increase, with the expected value indicated by a red line. With current gravitational-wave detectors sensitivities (O1), the measured median value with 90% credible interval is  $A_f/A_i = 1.31^{+0.84}_{-0.70}$ . Furthermore, we obtain a  $\sim 74.6\%$  probability that the simulated signal is consistent with the area theorem.

To ascertain how well we may test the area theorem in the future, we repeat the entire analysis on the same signal using the zero-detuned high-power (ZDHP) PSD from

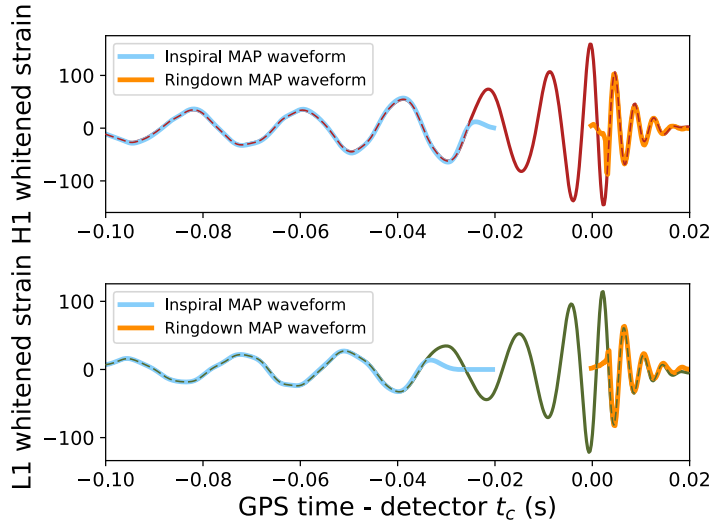


Figure 6.4: Whitened strain in each detector with the maximum posterior (MAP) waveform from the inspiral analysis (blue) and from the ringdown analysis (orange).

Ref. [185], which is the design sensitivity for Advanced LIGO. Figure 6.6 shows the JS divergence plots for the inspiral (left) and ringdown analyses (right). We find that the JS divergence of the inspiral (ringdown) posteriors settles to a constant value at  $t_{\text{ref}} - 27.5$  ms ( $t_{\text{ref}} + 0.5$  ms), which is the same as the O1 results. The selected ringdown grid time corresponds to  $12.6 M_f$  after the peak amplitude of the signal. While here we have chosen the JS divergence as an estimate of the adequate ringdown time, there is no unique definition in the literature of the start of the ringdown [178,193,194].

Results with the ZDHP configuration are shown by the dashed posterior in Fig. 6.5. In this case, the measured median value of the area increase with 90% credible interval is  $A_f/A_i = 1.58^{+0.35}_{-0.33}$ . With this sensitivity we obtain a  $\sim 99.9\%$  probability that the simulated signal is consistent with the area theorem.

The median value of  $A_f/A_i$  underestimates the true value in the O1 results. This is primarily due to a systematic bias arising in the inspiral analysis. Both the mass ratio  $q \equiv m_1/m_2$  ( $m_1 \geq m_2$ ) and total mass are overestimated with this method; this leads to an overestimate of  $A_i$  by  $\sim 10\%$ , in turn leading to an underestimate of  $A_f/A_i$ . Further biasing the median is the fact that the simulated signal used here has  $q = 1$ . Since this is on the boundary of allowed parameter space, the median of the posterior distribution can only ever overestimate  $q$ , again leading to an underestimate of  $A_f/A_i$ . The chirp mass is well measured, therefore an overestimate in the mass ratio leads to an overestimate in the total mass as well. Finally, as seen in Figure 6.5, our prior on  $A_f/A_i$  strongly favours a violation of the area theorem. The prior follows from the uniform prior on the inspiral masses and spins and the uniform prior on the ringdown frequency and damping time. This also shifts the posterior distribution to smaller values of  $A_f/A_i$ , though the effect is small compared to the effect of the systematic bias.

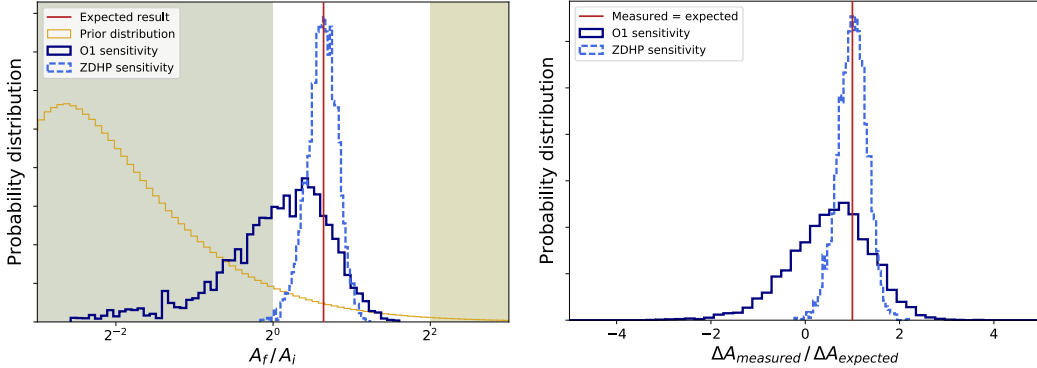


Figure 6.5: (Left) Posterior distribution on the ratio of the final to initial areas,  $A_f/(A_1 + A_2)$ , for two different Advanced LIGO sensitivities, O1 and ZDHP. The shaded region  $A_f/A_i < 1$  indicates violation of the area theorem. The shaded region  $A_f/A_i > 4$  indicates violation of the conservation of energy. The vertical red line is the expected area increase,  $A_f/A_i \simeq 1.56$ . (Right) Distribution of the ratio  $\Delta A_{\text{measured}}/\Delta A_{\text{expected}}$ . The measured area change corresponds to the distribution shown in the left figure. The expected area change is given by the initial parameters obtained in the inspiral analysis and the corresponding expected final parameters from the fitting formulae in [187]. The vertical red line indicates agreement between the measured and the expected values, i.e.  $\Delta A_{\text{measured}}/\Delta A_{\text{expected}} = 1$ .

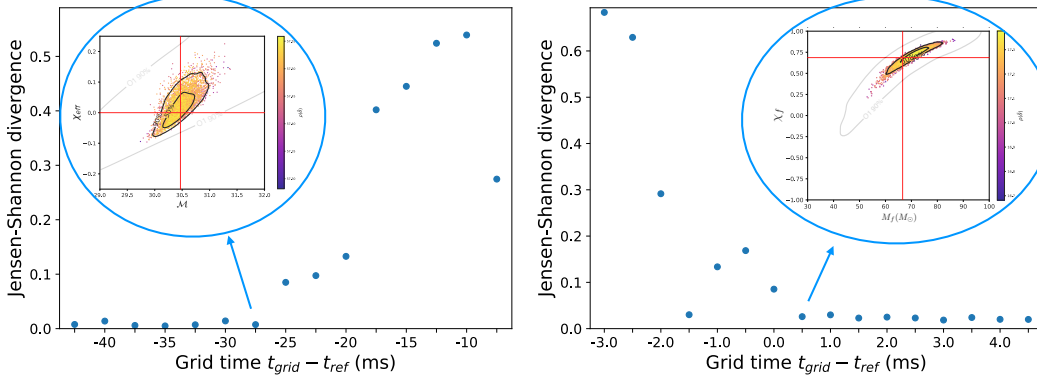


Figure 6.6: Jensen-Shannon divergence between consecutive grid times of the inspiral (left) and ringdown (right) analyses using the ZDHP PSD. Insets show the resulting posterior distribution for the chosen transition times. The light grey posteriors correspond to the results obtained with O1 sensitivity. For the inspiral (ringdown) analysis we find that the JS divergence settles at  $t_{\text{grid}} - t_{\text{ref}} = -27.5$  ms ( $t_{\text{grid}} - t_{\text{ref}} = 0.5$  ms), consistent with the O1 PSD results shown in Fig. 6.2.

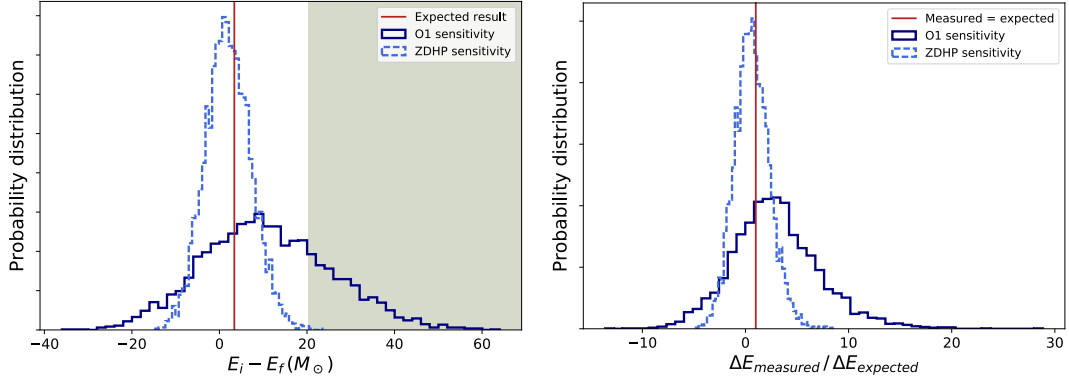


Figure 6.7: (Left) Posterior distribution on the energy radiated during the coalescence. The red line indicates the expected value for the injected parameters,  $E_i - E_f \simeq 3.4M_\odot$ . The shaded region shows the theoretical limit of 29% in the energy emitted. (Right) Distribution of the ratio  $\Delta E_{\text{measured}}/\Delta E_{\text{expected}}$ . The expected radiated energy is given by the initial parameters obtained in the inspiral analysis and the corresponding expected final parameters from the fitting formulae in [187]. The vertical red line indicates agreement between the measured and the expected values, i.e.  $\Delta E_{\text{measured}}/\Delta E_{\text{expected}} = 1$ .

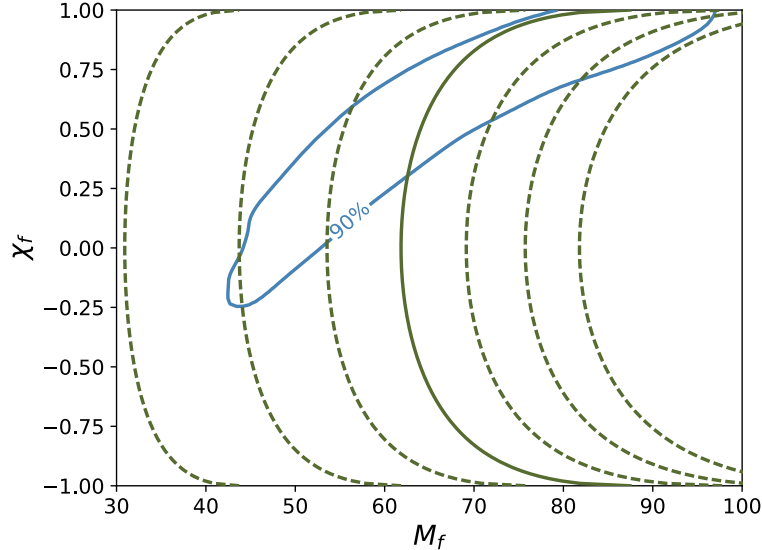


Figure 6.8: Lines of constant area as function of the final mass and spin. The solid line shows the expected value, while dashed lines indicate areas  $\pm 25\%$ ,  $\pm 50\%$ ,  $\pm 75\%$ . For comparison, the 90% credible interval from the ringdown analysis with O1 sensitivity is shown.

Overall, the systematic bias in the area increase is less than the statistical error. Furthermore, as the bias is toward violations of the area theorem, it is a conservative error when evaluating the credible interval to which the signal is consistent with the area theorem.

Given the measured initial parameters from the inspiral analysis, one can obtain the expected area change for each point in the initial distribution using the fitting formulae in [187]. A direct comparison of the expected change with the measured change indicates the level of agreement of the final object with the fitting formulae, and therefore with general relativity. If the final object agrees with general relativity, the ratio between the measured and the expected values should be 1. The right panel in Fig. 6.5 shows this ratio for the area change,  $\Delta A = A_f - A_i$ .

The independent measurements of the initial and final mass performed in this work also allow for estimating the energy radiated away by the system. The left panel in Fig. 6.7 shows the posterior distribution in the energy radiated away,  $\Delta E = E_i - E_f$ , for both current and future Advanced LIGO sensitivities. The shaded region indicates the 29% bound derived from the area increase law. Similar as with the area change, one can compare the measured energy radiated,  $\Delta E_{\text{measured}}$ , with the result one would obtain making use of the fitting formulae in [187],  $\Delta E_{\text{expected}}$ . The right panel in Fig. 6.7 shows the ratio between these two energies.

As can be seen by comparison of Fig. 6.5 and Fig. 6.7, the measurement of the area increase is more accurate than the measurement of the energy radiated. This can be understood from the lines of constant area shown in Fig. 6.8. The area follows the ringdown posteriors better than the mass at positive spins, which are expected for two initially non-spinning black holes. Furthermore, we can expect the measurement of the area to be even sharper for highly aligned spinning black holes.

## 6.4 Simulating violations of the area theorem

In this section we explore if we would be able to measure a violation of the area increase law with the method described above. We do not explore here how this violation could happen, but only if we would be able to measure a violation. For this purpose we compare our inspiral measurements with lower-mass ringdown signals. The spin of the final object is only dependent on the mass ratio and the spins of the initial objects. Changing the total mass of the binary will yield different final mass but the same final spin. Therefore, we find that for our system, a violation of the area theorem would require  $M_f < 53.3M_\odot$ . We use two ringdowns with masses  $M_f \simeq 52.3M_\odot$  and  $M_f \simeq 47.6M_\odot$ , and perform the ringdown analysis only with the ZDHP sensitivity.

Figure 6.9 shows the result of combining these new ringdowns with the original inspiral results. The dashed posterior distribution with  $\Delta M = M_f - M_t \simeq 3.4M_\odot$  is the result shown in the previous section. The continuous line with  $\Delta_M \simeq 17.7M_\odot$  is the system that yields a small violation of the area theorem. We find a  $\sim 55.2\%$  probability that this system is in violation of the area theorem. The dotted line shows the system with even lower mass, for which we obtain  $\sim 91.1\%$  probability that the system is in

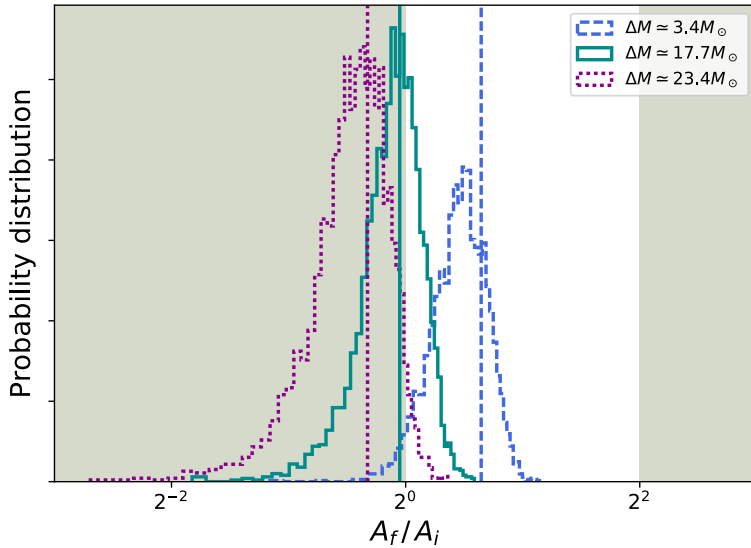


Figure 6.9: Posterior distribution on the ratio of the final to initial areas,  $A_f/(A_1 + A_2)$ , with ZDHP sensitivity. The shaded region  $A_f/A_i < 1$  indicates violation of the area theorem. The shaded region  $A_f/A_i > 4$  indicates violation of the conservation of energy. The dashed posterior distribution is the result shown in the previous section. The solid posterior distribution is a signal that slightly violates the area theorem, and the dotted posterior distribution is a signal that clearly violates the area theorem.

violation of the area theorem.

## 6.5 Conclusions

We developed a method to test the area theorem on gravitational-wave signals from binary black hole coalescences. This method completely ignores information from the highly dynamical merger phase, thus ensuring that the initial and final parameters are measured independently from each other, and without assuming general relativity during the merger process.

With current gravitational-wave detectors sensitivities and zero noise, we obtained  $\sim 74.6\%$  probability that a numerical waveform similar to GW150914 is consistent with the area theorem. This probability increases to  $\sim 99.9\%$  with design sensitivity (ZDHP) for Advanced LIGO.

The next obvious step is to perform this analysis on a real gravitational-wave signal. From the binary black holes known to date there is only one with loud enough ringdown to perform this test: GW150914. Application of the method presented in this chapter to this astrophysical signal is currently ongoing. One of the major issues is the choice of the start time for the ringdown. Our method of using the JS divergence will be a useful starting point for this analysis but might need to be refined for real data. In

simulations with Gaussian noise, we have found that the qualitative behaviour of the JS divergence is the same as in Fig. 6.3, however the data has larger variations. This will be investigated in future work on real detector data.

The confidences obtained are mainly bound by the ringdown analysis, which yields wider posterior distributions than the inspiral analysis. Higher modes could start becoming important before the end of the second generation of gravitational-wave detectors. The addition of sub-dominant modes to the ringdown analysis will not only allow for tests of the Kerr nature of the final black holes, but could result in better constraints on the final mass and spin. Therefore, detectable higher modes could improve the confidence level on testing the area theorem.

As we have seen, the sky location is also an important limiting factor in our analysis. In this paper we have shown results on a two-detector network. However, the Virgo detector joined the second generation of gravitational-wave detectors in August of 2017, and showed an important contribution on sky localisation of gravitational-wave sources. Future events could therefore show different confidence levels as reported in this work if more than two detectors are being used.

The techniques we present may also be extended to make a joint measurement of the violation of the area theorem for a population of binary black hole mergers. As an increasing number of mergers are detected, we expect that this may provide significant improvements to the overall uncertainties.

# Chapter 7

## Conclusions

The theory of General Relativity, published in 1915, predicted the emission of gravitational radiation. However, Albert Einstein also calculated that the amplitude of gravitational waves must have a practically vanishing value in all conceivable cases. It was hard to imagine that those infinitesimal fluctuations would ever be detected on Earth. One hundred years later, advancements in human technology, especially that of precision laser interferometry, enabled measurements of the effect of gravitational waves. On the 14th of September 2015, the Advanced LIGO detectors observed gravitational waves for the first time. The signal was emitted by a pair of black holes merging to form a single black hole. This detection was the first direct proof of the existence of black hole binaries. In this work, we have covered several different aspects related to gravitational-wave astronomy with compact binaries.

Search pipelines are algorithms designed to identify gravitational-wave signals in detector data. Low-latency searches provide a quick alert for candidate events in order to send rapid notices to other astronomical observers, while offline searches are crucial to accurately estimate the significance of the candidate and confidently establish its astrophysical origin. In this work, we explained how to search for compact binary coalescences, focusing explicitly on the PyCBC search pipeline, and showed the procedure that has been followed for the offline searches during the first two observing runs of Advanced LIGO. A specific type of noise transient, called blip glitch, cannot be vetoed from the search by normal procedures and degrades the sensitivity of the searches to short gravitational-wave transients. Search pipelines are continuously improving and developing methods to down-rank these glitches. However, it is best to address the problem by mitigating the cause in the detector hardware.

In the past, the main impediment to study blip glitches was the absence of information on the occurrences of such glitches. Here, we developed a method to find blip glitches in the data using PyCBC tools. With this method, we found thousands of blip glitches during the first two observing runs of Advanced LIGO. These lists of occurrences provide the information necessary to investigate the origin of blip noise transients. We successfully identified a few subsets of blip glitches: blips originating at the pre-stabilised

laser; blips associated with errors in the computational infrastructure; and a subset of blips related to periods of low relative humidity. To date, a large number of blip glitches remain of unknown origin. Additional investigations are underway.

Now that detectors have reached sufficient sensitivity and analysis techniques have matured to find gravitational waves, one can investigate the nature of the source and use the gravitational-wave signature to test General Relativity. In this work, we focused on the development of a test of the black hole area increase law. The first necessary ingredient involves independent measurements of the intrinsic parameters of the remnant black hole. Using PyCBC Inference, we developed a method to infer the final mass and spin from the ringdown signature of the waveform. This method was tested on the gravitational-wave signal GW150914, obtaining results consistent with those published previously. Furthermore, this method supports parameter estimation on ringdown signals with measurable subdominant modes. Using a simulated ringdown signal with a second detectable mode, we showed that one cannot recover the true parameters using ringdown templates which include only the fundamental mode. We also performed parameter estimation on this simulated signal using ringdown templates that incorporate the second subdominant mode, and showed that the expected parameters lay within the resulting posterior distribution. In the future, when detector sensitivities allow for detectable subdominant modes, this method could be used to test the ‘no-hair’ theorem.

On the other hand, measurements of the initial parameters of the compact binary can be performed using the inspiral signature of the signal. The transition from the inspiral to the merger can be defined by the minimum energy circular orbit (MECO) of the post-Newtonian energy. However, the MECO of the post-Newtonian energy does not exist when bodies have large spins, and no analytical solution to the end of the inspiral is known. We constructed a hybrid MECO by combining information of post-Newtonian theory with the exact Kerr solution. This method can be used for any known order of the post-Newtonian series and enables the MECO condition to be used to define the end of the inspiral phase for highly spinning, comparable mass systems. Additional physical effects are readily introduced in the hybrid energy, such as tidal deformations of neutron stars.

The test of the area theorem developed here is based on independent measurements of the masses and the spins. The merger phase, with its highly dynamical nature, is completely excluded from the analysis. On the inspiral part, gravitational-wave templates are terminated at the hybrid MECO to measure the initial masses and spins. On the ringdown part, the final mass and spin are inferred without requiring the fitting formulae normally used in inspiral-merger-ringdown analyses. To distinguish the appropriate end-of-inspiral and start-of-ringdown times, we used the Jensen-Shannon divergence. Using a simulated signal, we combined results from both signatures and showed that, with current detector sensitivities, it is possible to establish if a signal is consistent with the area theorem at about the 74.6% confidence level. Advanced LIGO running at design sensitivity may establish this consistency up to 99.9%. Application of this method to a real gravitational-wave signal, GW150914, is currently ongoing work. The ringdown signal-to-noise ratio of other binary black hole signals is insufficient to perform this test.

---

## APPENDICES

---



## Detector Characterisation tools

- *Omicron* [195]: algorithm used to identify excess power in gravitational-wave data. Omicron correlates single detector data with a generic sine Gaussian time-frequency projection. Triggers are times when the signal-to-noise ratio (as defined in Eq. (2.4)) is above a certain threshold. This algorithm is used to find triggers not only in the gravitational-wave channel, but especially in the auxiliary channels.
- *Hierarchical Veto (HVeto)* [196]: algorithm designed to find correlations between noise transients in auxiliary channels and in the main calibrated  $s(t)$  channel. HVeto uses auxiliary channels with negligible sensitivity to gravitational waves. The algorithm searches for temporal coincidences between Omicron triggers from the gravitational-wave channel and from the chosen auxiliary channels. The hierarchical removal works as follows: if a correlation with an auxiliary channel is found with high significance, corresponding triggers in  $s(t)$  are discarded. The algorithm searches then for further correlations in the remaining triggers. This method ensures finding the minimal set of veto conditions necessary.
- *Q-scan*: a time-frequency representation of the data. The transformation of a data time-series to the frequency domain is done by means of the Q transform [197,198]. This way of visualising the data is very useful to identify classes of noise transients. Furthermore, loud gravitational-wave signals show up as beautiful chirps in the Q-scan representation (see for instance [55]).
- *LIGO Data Viewer Web (LigoDV-Web)* [199]: web page to provide fast and easy access to LIGO data from anywhere (with LIGO or Virgo credentials). Data can be displayed as time series or spectrograms, for instance. All the time-frequency Q-scans shown in this work were generated using LigoDV-Web.
- *PyCBC Live*: low-latency search pipeline based on the PyCBC algorithm. This search was developed between the first (O1) and second (O2) observing runs of Advanced LIGO. PyCBC Live not only finds gravitational-wave signals from compact binary coalescences, but also noise transients in the data which are most

detrimental to the search. Therefore, this low-latency search was used during O2 to identify noise transients for detector characterisation purposes. Classifying the triggers based on the duration of the triggering template helped separate different types of glitches.

- *DetChar summary pages*: online pages showing the status of the detectors, designed to identify issues in the data or in the detectors themselves. These pages display data-segment times, triggers from Omicron and from PyCBC Live, results from HVeto, environmental factors such as ground motion or wind speed, status of individual parts of the detectors such as the pre-stabilised laser (PSL) or the output-mode cleaner (OMC), etc. The summary pages are internal to the LIGO, Virgo, and GEO Collaborations. A reduced, public viewable version of these pages can be found in [200].

# Appendix B

## Relations between parameters

The Kerr ISCO location given in Eq. (5.1) is coordinate dependent. The orbital radius  $r$  can be expressed in terms of the PN velocity parameter  $v$ , thus obtaining a gauge-invariant ISCO independent of the total mass of the system:

$$\frac{v^2}{(1 - \chi v^3)^{2/3}} = \frac{M}{r}. \quad (\text{B.1})$$

At zero spin, this relation reduces to  $v = \sqrt{M/r}$ , which gives a velocity of  $v = 1/\sqrt{6} \simeq 0.41$  for the Schwarzschild ISCO ( $r = 6M$ ). For extreme spins ( $\chi = \pm 1$ ), the Kerr ISCO corresponds to velocities of  $v \simeq 0.79$  (aligned case) and  $v \simeq 0.34$  (anti-aligned case). Furthermore, one can obtain the gravitational-wave frequency through the relation  $v = (\pi M f_{\text{GW}})^{1/3}$ . For instance, a binary black hole with  $M = 20M_\odot$  has a gravitational-wave frequency  $f_{\text{GW}} \simeq 220$  Hz at the Schwarzschild ISCO velocity  $v = 1/\sqrt{6}$ .

The phase of the gravitational wave can be used to compute the number of cycles between different terminations. The number of gravitational-wave cycles  $\mathcal{N}$  between the velocities  $v_1$  and  $v_2$  can be given by

$$\mathcal{N} = \frac{\Phi^{\text{GW}}(v_2) - \Phi^{\text{GW}}(v_1)}{2\pi}, \quad (\text{B.2})$$

where  $\Phi^{\text{GW}}(v)$  is the gravitational-wave phase (twice the orbital phase). The post-Newtonian gravitational-wave phase as function of the frequency can be obtained from Eq. (3.11) in [145] (or the orbital phase as function of the velocity from Eqs. (318) and (3.8a) in [31] and [90], respectively). At the leading order, the gravitational-wave phase is independent of the spin and is given by

$$\Phi^{\text{GW}}(v) = -\frac{1}{16v^5\eta}. \quad (\text{B.3})$$

Between the minimum (anti-aligned) and the maximum (aligned) velocity values of the Kerr ISCO, the number of gravitational-wave cycles for an equal-mass binary ( $\eta = 0.25$ ) is  $\mathcal{N} \simeq 8.6$ , and  $\mathcal{N} \simeq 43.1$  for a binary with  $\eta = 0.05$ . Let's consider the case of an

---

## APPENDIX B. Relations between parameters

---

equal-mass BBH with total mass  $M = 20M_{\odot}$ . In the bandwidth of a gravitational-wave detector with lower frequency cutoff at  $f_0 = 30$  Hz, the gravitational wave of this binary will be visible from  $v_1 \simeq 0.21$ . If the two black holes are maximally spinning,  $\chi_1 = \chi_2 = 1$ , at the Kerr ISCO velocity  $v_2 \simeq 0.79$  the gravitational wave will have  $\mathcal{N} \simeq 97.3$  cycles. If one were to use the anti-aligned Kerr ISCO velocity  $v \simeq 0.34$  for this binary, the 8.6 cycles between the Kerr ISCO velocities mean that one would miss 8.8% of the inspiral phase. If the binary has a larger total mass, it enters the detector's bandwidth later in the evolution. For  $M = 70M_{\odot}$ , for instance, one would miss 37.3% of the inspiral phase.

# Appendix C

## Post-Newtonian approximation

The derivation of the different terms of the post-Newtonian energy and energy flux in the centre-of-mass frame can be found in the literature [31, 130–137]. This Appendix is a collection, in one place, of all the terms used in this paper. Since the orbits of compact binaries are expected to circularise by the time they become visible with current gravitational-wave detectors, we restrict ourselves to the expressions for circular orbits. The different terms in the energy per unit total mass and the energy flux are:

$$E^{\text{PN}} = -\frac{1}{2}\eta v^2 [E_{\text{NS}} + E_{\text{SO}} + E_{\text{SS}} + E_{S^3} + E_{S^4}] , \quad (\text{C.1})$$

$$\mathcal{F}^{\text{PN}} = \frac{32}{5}\eta^2 v^{10} [\mathcal{F}_{\text{NS}} + \mathcal{F}_{\text{SO}} + \mathcal{F}_{\text{SS}} + \mathcal{F}_{S^3}] , \quad (\text{C.2})$$

where NS are the non-spinning terms, SO the spin-orbit terms, SS the spin-spin terms,  $S^3$  the spin-cubed terms, and  $S^4$  the spin-quartic terms. The individual masses of the bodies are denoted  $m_1$  and  $m_2$ ,  $M = m_1 + m_2$  is the total mass of the binary, the  $v$  parameter is given by the sum of the speeds in the rest-mass frame  $v = v_1 + v_2$ , and  $\eta = m_1 m_2 / M^2$  is the symmetric mass ratio.

The non-spinning energy terms are known up to 4PN [31, 90]

$$\begin{aligned} E_{\text{NS}} = & 1 - \left( \frac{3}{4} + \frac{\eta}{12} \right) v^2 - \left( \frac{27}{8} - \frac{19}{8}\eta + \frac{\eta^2}{24} \right) v^4 \\ & - \left[ \frac{675}{64} - \left( \frac{34445}{576} - \frac{205\pi^2}{96} \right) \eta + \frac{155}{96}\eta^2 + \frac{35}{5184}\eta^3 \right] v^6 \\ & - \left[ \frac{3969}{128} + \left( \frac{123671}{5760} - \frac{9037\pi^2}{1536} - \frac{1792}{15} \ln 2 - \frac{896}{15}\gamma_E \right) \eta \right. \\ & \left. + \left( \frac{498449}{3456} - \frac{3157\pi^2}{576} \right) \eta^2 - \frac{301}{1728}\eta^3 - \frac{77}{31104}\eta^4 - \frac{448}{15}\eta \ln v^2 \right] v^8 + \mathcal{O}(v^{10}) , \end{aligned} \quad (\text{C.3})$$

where  $\gamma_E$  is the Euler constant.

---

## APPENDIX C. Post-Newtonian approximation

---

For the spin-orbit terms, we define the variables

$$\mathbf{S} = \mathbf{S}_1 + \mathbf{S}_2, \quad \Sigma = M \left( \frac{\mathbf{S}_2}{m_2} - \frac{\mathbf{S}_1}{m_1} \right),$$

$$S_L = \frac{\mathbf{S} \cdot \mathbf{L}}{M^2}, \quad \Sigma_L = \frac{\Sigma \cdot \mathbf{L}}{M^2},$$

where  $\mathbf{S}_1$  and  $\mathbf{S}_2$  are the individual vector spins of the objects, and  $\mathbf{L}$  is the unit vector pointing in the direction of the orbital angular momentum. We will also use  $S_{1L} = \mathbf{S}_1 \cdot \mathbf{L}$  and  $S_{2L} = \mathbf{S}_2 \cdot \mathbf{L}$ .

The spin-orbit terms are known up to 3.5PN [135, 136]

$$E_{SO} = \left( \frac{14}{3} S_L + 2\delta\Sigma_L \right) v^3 + \left[ \left( 11 - \frac{61}{9}\eta \right) S_L + \left( 3 - \frac{10}{3}\eta \right) \delta\Sigma_L \right] v^5$$

$$+ \left[ \left( \frac{135}{4} - \frac{367}{4}\eta + \frac{29}{12}\eta^2 \right) S_L + \left( \frac{27}{4} - 39\eta + \frac{5}{4}\eta^2 \right) \delta\Sigma_L \right] v^7 + \mathcal{O}(v^8), \quad (\text{C.4})$$

where  $\delta = (m_1 - m_2)/M$ .

For the following spinning terms, we restrict ourselves to the expressions for spin-aligned binaries, and introduce the quantity  $q_i = m_i/M$ .

The 2PN spin-spin term is given by [131, 133]

$$E_{SS}^{2\text{PN}} = -\frac{1}{M^2} \left( \frac{2S_1S_2}{m_1m_2} + \frac{S_1^2\kappa_1}{m_1^2} + \frac{S_2^2\kappa_2}{m_2^2} \right) v^4, \quad (\text{C.5})$$

where the constants  $\kappa_i$  are the quadrupole terms that represent the distortion of the bodies due to their spins [201]. For black holes,  $\kappa_i = 1$ . For neutron stars,  $\kappa_i \simeq 4 - 8$  depending on the equation of state.

The 3PN spin-spin term is given by [132, 133]

$$E_{SS}^{3\text{PN}} = -\frac{1}{M^2} \left\{ \frac{5}{9} \frac{S_1S_2}{m_1m_2} (3 + \eta) - \frac{S_1^2}{m_1^2} \left[ \frac{5}{9} (9 - 3\eta - 5q_1^2) - \frac{5\kappa_1}{6} (3 + 3\eta + 4q_1^2) \right] \right.$$

$$\left. - \frac{S_2^2}{m_2^2} \left[ \frac{5}{9} (9 - 3\eta - 5q_2^2) - \frac{5\kappa_2}{6} (3 + 3\eta + 4q_2^2) \right] \right\} v^6. \quad (\text{C.6})$$

The 4PN spin-spin term is given by [134]

$$E_{SS}^{4\text{PN}} = -\frac{7}{18M^2} \left[ \frac{S_1S_2}{12m_1m_2} (135 - 429\eta - 53\eta^2) \right.$$

$$+ \frac{S_1^2}{7M^2} \left( \frac{1}{3} (360 - 749\eta) + \kappa_1 (279 - 79\eta) \right)$$

$$- \frac{S_1^2}{m_1^2} \left( 27 + 6\eta + 31\eta^2 - \frac{3\kappa_1}{4} (27 + 11\eta - 13\eta^2) \right)$$

$$\left. + \frac{S_2^2}{7M^2} \left( \frac{1}{3} (360 - 749\eta) + \kappa_2 (279 - 79\eta) \right) \right]$$

$$-\frac{S_2^2}{m_2^2} \left( 27 + 6\eta + 31\eta^2 - \frac{3\kappa_2}{4}(27 + 11\eta - 13\eta^2) \right) \Big] v^8. \quad (\text{C.7})$$

The spin-cubed term is given by [136, 137]

$$E_{S^3} = -\frac{2}{M^3} \left\{ \frac{S_1^3}{m_1^3} [(3 - q_1)\kappa_1 - 2\lambda_1] + \frac{S_2^3}{m_2^3} [(3 - q_2)\kappa_2 - 2\lambda_2] + \frac{S_1^2 S_2}{m_1^2 m_2} [6 - 2q_1 - (4 - q_1)\kappa_1] + \frac{S_1 S_2^2}{m_1 m_2^2} [6 - 2q_2 - (4 - q_2)\kappa_2] \right\} v^7, \quad (\text{C.8})$$

where the constants  $\lambda_i$  are the octupole terms that characterise the deformation of the bodies due to their spins [137]. For black holes,  $\lambda_i = \kappa_i = 1$ . For neutron stars, the value of  $\lambda_i$  is yet unknown.

The spin-quartic term is given by [134]

$$E_{S^4} = -\frac{7}{M^4} \left\{ \frac{1}{4} \frac{S_1^4}{m_1^4} (C_1 - \kappa_1^2) + \frac{S_1^3 S_2}{m_1^3 m_2} (\lambda_1 - \kappa_1) + \frac{S_1^2 S_2^2}{m_1^2 m_2^2} (\kappa_1 \kappa_2 - 1) + \frac{S_1 S_2^3}{m_1 m_2^3} (\lambda_2 - \kappa_2) + \frac{1}{4} \frac{S_2^4}{m_2^4} (C_2 - \kappa_2^2) \right\} v^8, \quad (\text{C.9})$$

where the constants  $C_i$  are the hexadecapole terms that characterise the deformation of the bodies due to their spins [134]. Note that this spin-quartic term vanishes for binary black hole systems ( $\kappa_i = \lambda_i = C_i = 1$ ) and for the neutron-star black-hole binaries we consider in this paper ( $S_2 = S_{NS} = 0$ ).

The non-spinning energy flux terms are known up to 3.5PN [31, 90]

$$\begin{aligned} \mathcal{F}_{\text{NS}} = & 1 - \left( \frac{1247}{336} + \frac{35}{12}\eta \right) v^2 + 4\pi v^3 - \left( \frac{44711}{9072} - \frac{9721}{504}\eta - \frac{65}{18}\eta^2 \right) v^4 \\ & - \left( \frac{8191}{672} + \frac{538}{24}\eta \right) \pi v^5 \\ & + \left[ \frac{6643739519}{69854400} + \frac{16\pi^2}{3} - \frac{1712}{105}\gamma_E - \left( \frac{134543}{7776} - \frac{41\pi^2}{48} \right) \eta - \frac{94403}{3024}\eta^2 \right. \\ & \quad \left. - \frac{775}{324}\eta^3 - \frac{856}{105} \ln [16v^2] \right] v^6 \\ & - \left( \frac{16285}{504} - \frac{214745}{1728}\eta - \frac{193385}{3024}\eta^2 \right) \pi v^7 + \mathcal{O}(v^8), \end{aligned} \quad (\text{C.10})$$

where  $\gamma_E$  is the Euler constant.

The spin-orbit terms are known up to 3.5PN [135]

$$\begin{aligned} \mathcal{F}_{\text{SO}} = & - \left( 4S_L + \frac{5}{4}\delta\Sigma_L \right) v^3 + \left[ \left( -\frac{9}{2} + \frac{272}{9}\eta \right) S_L + \left( -\frac{13}{16} + \frac{43}{4}\eta \right) \delta\Sigma_L \right] v^5 \\ & - \left( 16\pi S_L + \frac{31\pi}{6}\delta\Sigma_L \right) v^6 + \left[ \left( \frac{476645}{6804} + \frac{6172}{189}\eta - \frac{2810}{27}\eta^2 \right) S_L \right. \end{aligned} \quad (\text{C.11})$$

$$+ \left( \frac{9535}{336} + \frac{1849}{126} \eta - \frac{1501}{36} \eta^2 \right) \delta \Sigma_L \right] v^7 + \mathcal{O}(v^8),$$

where  $\delta = (m_1 - m_2)/M$ .

The 2PN spin-spin term is given by [131, 132]

$$\begin{aligned} \mathcal{F}_{SS}^{2\text{PN}} = & \left[ S_L^2 (2\kappa_+ + 4) + S_L \Sigma_L (2\delta\kappa_+ + 4\delta - 2\kappa_-) \right. \\ & \left. + \Sigma_L^2 \left( \left( -\delta\kappa_- + \kappa_+ + \frac{1}{16} \right) + \eta (-2\kappa_+ - 4) \right) \right] v^4, \end{aligned} \quad (\text{C.12})$$

where  $\kappa_+ = \kappa_1 + \kappa_2$  and  $\kappa_- = \kappa_1 - \kappa_2$ .

The 3PN spin-spin term is given by [132]

$$\begin{aligned} \mathcal{F}_{SS}^{3\text{PN}} = & \left\{ S_L^2 \left[ \left( \frac{41\delta\kappa_-}{16} - \frac{271\kappa_+}{112} - \frac{5239}{504} \right) - \eta \left( \frac{43\kappa_+}{4} + \frac{43}{2} \right) \right] \right. \\ & + S_L \Sigma_L \left[ - \left( \frac{279\delta\kappa_+}{56} + \frac{817\delta}{56} - \frac{279\kappa_-}{56} \right) - \eta \left( \frac{43\delta\kappa_+}{4} + \frac{43\delta}{2} + \frac{\kappa_-}{2} \right) \right] \\ & + \Sigma_L^2 \left[ \left( \frac{279\delta\kappa_-}{112} - \frac{279\kappa_+}{112} - \frac{25}{8} \right) \right. \\ & \left. \left. + \eta \left( \frac{45\delta\kappa_-}{16} + \frac{243\kappa_+}{112} + \frac{344}{21} \right) + \eta^2 \left( \frac{43\kappa_+}{4} + \frac{43}{2} \right) \right] \right\} v^6. \end{aligned} \quad (\text{C.13})$$

The spin-cubed term is given by [137]

$$\begin{aligned} \mathcal{F}_{S^3} = & \left\{ -S_L^3 \left( \frac{16\kappa_+}{3} + 4\lambda_+ - \frac{40}{3} \right) - S_L^2 \Sigma_L \left( \frac{35\delta\kappa_+}{6} + 6\delta\lambda_+ - \frac{73\delta}{3} + \frac{3\kappa_-}{4} - 6\lambda_- \right) \right. \\ & - S_L \Sigma_L^2 \left[ \frac{35\delta\kappa_-}{12} - 6\delta\lambda_- - \frac{35\kappa_+}{12} + 6\lambda_+ - \frac{32}{3} - \eta \left( \frac{22\kappa_+}{3} + 12\lambda_+ - \frac{172}{3} \right) \right] \\ & + \Sigma_L^3 \left[ \frac{67\delta\kappa_+}{24} - 2\delta\lambda_+ - \frac{\delta}{8} - \frac{67\kappa_-}{24} + 2\lambda_- \right. \\ & \left. \left. + \eta \left( \frac{\delta\kappa_+}{2} + 2\delta\lambda_+ - 11\delta + \frac{61\kappa_-}{12} - 6\lambda_- \right) \right] \right\} v^7, \end{aligned} \quad (\text{C.14})$$

where  $\lambda_+ = \lambda_1 + \lambda_2$  and  $\lambda_- = \lambda_1 - \lambda_2$ .

## Bibliography

- [1] S. Chandrasekhar, “The highly collapsed configurations of a stellar mass,” *Monthly Notices R. Astron. Soc.*, vol. 91, pp. 456–466, 1931.
- [2] S. Chandrasekhar, “The highly collapsed configurations of a stellar mass (second paper),” *Monthly Notices R. Astron. Soc.*, vol. 95, pp. 207–225, 1935.
- [3] W. Herschel, “VI. Catalogue of double stars,” *Phil. Trans. R. Soc. Lon.*, vol. 75, pp. 40–126, 1785.
- [4] S. J. Kleinman, S. O. Kepler, D. Koester, I. Pelisoli, V. Peçanha, A. Nitta, J. E. S. Costa, J. Krzesinski, P. Dufour, F.-R. Lachapelle, P. Bergeron, C.-W. Yip, H. C. Harris, D. J. Eisenstein, L. Althaus, and A. Córscico, “SDSS DR7 white dwarf catalog,” *Astrophys. J. Supplement Series*, vol. 204, p. 5, 2013.
- [5] N. Glendenning, *Compact Stars: Nuclear Physics, Particle Physics and General Relativity*. Astronomy and Astrophysics Library, Springer New York, 2012.
- [6] R. C. Tolman, “Static solutions of einstein’s field equations for spheres of fluid,” *Phys. Rev.*, vol. 55, pp. 364–373, 1939.
- [7] J. R. Oppenheimer and G. M. Volkoff, “On massive neutron cores,” *Phys. Rev.*, vol. 55, pp. 374–381, 1939.
- [8] I. S. Shklovsky, “On the nature of the source of X-Ray emission of Sco XR-1,” *Astrophys. J.*, vol. 148, p. L1, 1967.
- [9] A. Hewish, J. Bell, J. D. H. Pilkington, P. F. Scott, and R. A. Collins, “Observation of a rapidly rotating pulsating radio source,” *Nature*, vol. 217, p. 709, 1968.
- [10] R. N. Manchester, G. B. Hobbs, A. Teoh, and M. Hobbs, “The Australia Telescope National Facility pulsar catalogue,” *Astron. J.*, vol. 129, p. 1993, 2005.
- [11] The Australia Telescope National Facility, “ATNF pulsar catalogue.” <http://www.atnf.csiro.au/research/pulsar/psrcat/>

## BIBLIOGRAPHY

---

- [12] R. Penrose, “Gravitational collapse and space-time singularities,” *Phys. Rev. Lett.*, vol. 14, pp. 57–59, 1965.
- [13] K. Schwarzschild, “Über das gravitationsfeld einer kugel aus inkompressibler flüssigkeit nach der einsteinschen theorie,” in *Sitzungsberichte der Königlich Preussischen Akademie der Wissenschaften zu Berlin, Phys.-Math. Klasse, 424-434* (1916), 1916.
- [14] S. W. Hawking and G. F. R. Ellis, *The large scale structure of space-time*. Cambridge University Press, 1973.
- [15] J. M. Weisberg, J. H. Taylor, and L. A. Fowler, “Gravitational waves from an orbiting pulsar,” *Scientific American*, vol. 245, p. 74, 1981.
- [16] J. M. Weisberg and J. H. Taylor, “Relativistic binary pulsar B1913+16: thirty years of observations and analysis,” *ASP Conf. Ser.*, vol. 328, p. 25, 2004.
- [17] N. Wex, “Testing the motion of strongly self-gravitating bodies with radio pulsars,” *Fund. Theor. Phys.*, vol. 179, p. 651, 2015.
- [18] The LIGO Scientific Collaboration and the Virgo Collaboration, “Observation of gravitational waves from a binary black hole merger,” *Phys. Rev. Lett.*, vol. 116, no. 6, p. 061102, 2016.
- [19] B. Schutz, *Gravity from the ground up*. Cambridge University Press, 2003.
- [20] B. Schutz, *A first course in General Relativity*. Cambridge University Press, 2009.
- [21] C. W. Misner, K. S. Thorne, and J. A. Wheeler, *Gravitation*. W. H. Freeman and company, 1970.
- [22] R. M. Wald, *General Relativity*. The University of Chicago Press, 1984.
- [23] S. Carroll, *Spacetime and geometry*. Addison Wesley, 2004.
- [24] K. S. Thorne, “300 years of gravitation,” in *Gravitational radiation* (S. Hawking and W. Israel, eds.), Cambridge University Press, 1987.
- [25] M. Maggiore, *Gravitational waves. Volume I: theory and experiments*. Oxford University Press, 2008.
- [26] R. P. Kerr, “Gravitational field of a spinning mass as an example of algebraically special metrics,” *Phys. Rev. Lett.*, vol. 11, pp. 237–238, 1963.
- [27] A. L. Piro, B. Giacomazzo, and R. Perna, “The fate of neutron star binary mergers,” *Astroph. J. Lett.*, vol. 844, no. 2, p. L19, 2017.
- [28] L. Baiotti and L. Rezzolla, “Binary neutron star mergers: a review of Einstein’s richest laboratory,” *Rep. Progr. Phys.*, vol. 80, no. 9, p. 096901, 2017.

---

## BIBLIOGRAPHY

- [29] P. C. Peters, “Gravitational radiation and the motion of two point masses,” *Phys. Rev. B*, vol. 136, no. 4, p. B1224, 1964.
- [30] L. S. Finn and D. F. Chernoff, “Observing binary inspiral in gravitational radiation: One interferometer,” *Phys. Rev. D*, vol. 47, pp. 2198–2219, 1993.
- [31] L. Blanchet, “Gravitational radiation from Post-Newtonian sources and inspiralling compact binaries,” *Living Rev. Relativity*, vol. 17, no. 2, 2014.
- [32] C. M. Will, “On the unreasonable effectiveness of the post-Newtonian approximation in gravitational physics,” *Proc. Nat. Acad. Sci.*, vol. 108, no. 15, p. 5938, 2011.
- [33] F. Pretorius, “Evolution of binary black hole spacetimes,” *Phys. Rev. Lett.*, vol. 95, p. 121101, 2005.
- [34] M. Campanelli, C. O. Lousto, P. Marronetti, and Y. Zlochower, “Accurate evolutions of orbiting black-hole binaries without excision,” *Phys. Rev. Lett.*, vol. 96, p. 111101, 2006.
- [35] J. G. Baker, J. Centrella, D.-I. Choi, M. Koppitz, and J. van Meter, “Gravitational wave extraction from an inspiraling configuration of merging black holes,” *Phys. Rev. Lett.*, vol. 96, p. 111102, 2006.
- [36] E. Berti, V. Cardoso, and A. O. Starinets, “Quasinormal modes of black holes and black branes,” *Class. Quant. Grav.*, vol. 26, no. 16, p. 163001, 2009.
- [37] S. A. Teukolsky, “Rotating black holes: Separable wave equations for gravitational and electromagnetic perturbations,” *Phys. Rev. Lett.*, vol. 29, pp. 1114–1118, 1972.
- [38] S. A. Teukolsky, “Perturbations of a rotating black hole. I. Fundamental equations for gravitational electromagnetic and neutrino field perturbations,” *Astrophys. J.*, vol. 185, pp. 635–647, 1973.
- [39] W. H. Press and S. A. Teukolsky, “Perturbations of a rotating black hole. II. Dynamical stability of the Kerr metric,” *Astrophys. J.*, vol. 185, pp. 649–674, 1973.
- [40] S. A. Teukolsky and W. Press, “Perturbations of a rotating black hole. III. Interaction of the hole with gravitational and electromagnetic radiation,” *Astrophys. J.*, vol. 193, pp. 443–461, 1974.
- [41] J. M. Bardeen, W. H. Press, and S. A. Teukolsky, “Rotating black holes: locally nonrotating frames, energy extraction, and scalar synchrotron radiation,” *Astrophys. J.*, vol. 178, p. 347, 1972.
- [42] S. Chandrasekhar, “The mathematical theory of black holes,” in *Oxford, UK: Clarendon (1985) 646 p.*, 1985.

## BIBLIOGRAPHY

---

- [43] O. Dreyer, B. J. Kelly, B. Krishnan, L. S. Finn, D. Garrison, and R. Lopez-Aleman, “Black hole spectroscopy: Testing general relativity through gravitational wave observations,” *Class. Quant. Grav.*, vol. 21, pp. 787–804, 2004.
- [44] A. Abramovici, W. E. Althouse, R. W. P. Drever, Y. Gürsel, S. Kawamura, F. J. Raab, D. Shoemaker, L. Sievers, R. E. Spero, K. S. Thorne, R. E. Vogt, R. Weiss, S. E. Whitcomb, and M. E. Zucker, “LIGO: The Laser Interferometer Gravitational-Wave Observatory,” *Science*, vol. 256, no. 5055, pp. 325–333, 1992.
- [45] P. Jaranowski and A. Królc, *Analysis of gravitational-wave data*. Cambridge University Press, 2009.
- [46] T. A. Apostolatos, C. Cutler, G. J. Sussman, and K. S. Thorne, “Spin induced orbital precession and its modulation of the gravitational waveforms from merging binaries,” *Phys. Rev. D*, vol. 49, pp. 6274–6297, 1994.
- [47] The LIGO Scientific Collaboration and the Virgo Collaboration, “Prospects for observing and localizing gravitational-wave transients with Advanced LIGO and Advanced Virgo,” *Living Rev. Relativity*, vol. 19, no. 1, p. 1, 2016.
- [48] The LIGO Scientific Collaboration, “Advanced LIGO,” *Class. Quant. Grav.*, vol. 32, no. 7, p. 074001, 2015.
- [49] M. Pitkin, S. Reid, S. Rowan, and J. Hough, “Gravitational wave detection by interferometry (ground and space),” *Living Rev. Relativity*, vol. 14, no. 1, p. 5, 2011.
- [50] The LIGO Scientific Collaboration and the Virgo Collaboration, “GW151226: Observation of gravitational waves from a 22-solar-mass binary black hole coalescence,” *Phys. Rev. Lett.*, vol. 116, no. 24, p. 241103, 2016.
- [51] The LIGO Scientific Collaboration and the Virgo Collaboration, “Binary black hole mergers in the first Advanced LIGO observing run,” *Phys. Rev. X*, vol. 6, p. 041015, 2016.
- [52] The LIGO Scientific Collaboration and the Virgo Collaboration, “GW170104: Observation of a 50-solar-mass binary black hole coalescence at redshift 0.2,” *Phys. Rev. Lett.*, vol. 118, p. 221101, 2017.
- [53] The LIGO Scientific Collaboration and The Virgo Collaboration, “GW170608: Observation of a 19-solar-mass binary black hole coalescence,” *Astroph. J. Lett.*, vol. 851, no. 2, p. L35, 2017.
- [54] The LIGO Scientific Collaboration and The Virgo Collaboration, “GW170814: A three-detector observation of gravitational waves from a binary black hole coalescence,” *Phys. Rev. Lett.*, vol. 119, no. 14, p. 141101, 2017.

---

## BIBLIOGRAPHY

- [55] The LIGO Scientific Collaboration and The Virgo Collaboration, “GW170817: Observation of gravitational waves from a binary neutron star inspiral,” *Phys. Rev. Lett.*, vol. 119, no. 16, p. 161101, 2017.
- [56] B. P. Abbott et al., “Multi-messenger observations of a binary neutron star merger,” *Astrophys. J. Lett.*, vol. 848, no. 2, p. L12, 2017.
- [57] K. Riles, “Recent searches for continuous gravitational waves,” *Mod. Phys. Lett. A*, vol. 32, p. 1730035, 2017.
- [58] LIGO Scientific Collaboration and Virgo Collaboration, “Observing gravitational-wave transient GW150914 with minimal assumptions,” *Phys. Rev. D*, vol. 93, p. 122004, 2016.
- [59] S. Khan, S. Husa, M. Hannam, F. Ohme, M. Pürrer, X. Jiménez Forteza, and A. Bohé, “Frequency-domain gravitational waves from nonprecessing black-hole binaries. II. A phenomenological model for the advanced detector era,” *Phys. Rev. D*, vol. 93, no. 4, p. 044007, 2016.
- [60] A. Bohé, L. Shao, A. Taracchini, A. Buonanno, S. Babak, I. W. Harry, I. Hinder, S. Ossokine, M. Pürrer, V. Raymond, T. Chu, H. Fong, P. Kumar, H. P. Pfeiffer, M. Boyle, D. A. Hemberger, L. E. Kidder, G. Lovelace, M. A. Scheel, and B. Szilágyi, “Improved effective-one-body model of spinning, nonprecessing binary black holes for the era of gravitational-wave astrophysics with advanced detectors,” *Phys. Rev. D*, vol. 95, p. 044028, 2017.
- [61] T. Dal Canton *et al.*, “Implementing a search for aligned-spin neutron star-black hole systems with advanced ground based gravitational wave detectors,” *Phys. Rev. D*, vol. 90, no. 8, p. 082004, 2014.
- [62] S. A. Usman, A. H. Nitz, I. W. Harry, C. M. Biwer, D. A. Brown, M. Cabero, C. D. Capano, T. Dal Canton, T. Dent, B. Krishnan, A. Lenon, A. Lundgren, A. B. Nielsen, L. P. Pekowsky, H. P. Pfeiffer, P. R. Saulson, M. West, and J. L. Willis, “The PyCBC search for gravitational waves from compact binary coalescence,” *Class. Quant. Grav.*, vol. 33, no. 21, p. 215004, 2016.
- [63] A. H. Nitz, I. W. Harry, C. M. Biwer, D. Brown, J. Willis, T. Dal Canton, *et al.*, “PyCBC github repository.” <https://github.com/ligo-cbc/pycbc/>
- [64] B. Allen, W. G. Anderson, P. R. Brady, D. A. Brown, and J. D. E. Creighton, “FINDCHIRP: An Algorithm for detection of gravitational waves from inspiraling compact binaries,” *Phys. Rev. D*, vol. 85, p. 122006, 2012.
- [65] B. S. Sathyaprakash and B. F. Schutz, “Physics, astrophysics and cosmology with gravitational waves,” *Living Rev. Relativity*, vol. 12, no. 1, 2009.
- [66] L. A. Wainstein and V. D. Zubakov, *Extraction of Signals from Noise*. Prentice-Hall, Englewood Cliffs, NJ, 1962.

## BIBLIOGRAPHY

---

- [67] The LIGO Scientific Collaboration and The Virgo Collaboration, “GW150914: First results from the search for binary black hole coalescence with Advanced LIGO,” *Phys. Rev. D*, vol. 93, p. 122003, 2016.
- [68] T. Dal Canton and I. W. Harry, “Designing a template bank to observe compact binary coalescences in Advanced LIGO’s second observing run,” *arXiv:1705.01845*, 2017.
- [69] The LIGO Scientific Collaboration and The Virgo Collaboration, “Characterization of transient noise in Advanced LIGO relevant to gravitational wave signal GW150914,” *Class. Quant. Grav.*, vol. 33, no. 13, p. 134001, 2016.
- [70] The LIGO Scientific Collaboration and The Virgo Collaboration, “Effects of data quality vetoes on a search for compact binary coalescences in Advanced LIGO’s first observing run,” *Class. Quant. Grav.*, vol. 35, no. 6, p. 065010, 2018.
- [71] B. Allen, “ $\chi^2$  time-frequency discriminator for gravitational wave detection,” *Phys. Rev. D*, vol. 71, p. 062001, 2005.
- [72] A. H. Nitz, “Distinguishing short duration noise transients in ligo data to improve the pycbc search for gravitational waves from high mass binary black hole mergers,” *Class. Quant. Grav.*, vol. 35, no. 3, p. 035016, 2018.
- [73] A. H. Nitz, T. Dent, T. D. Canton, S. Fairhurst, and D. A. Brown, “Detecting binary compact-object mergers with gravitational waves: Understanding and improving the sensitivity of the pycbc search,” *Astrophys. J.*, vol. 849, no. 2, p. 118, 2017.
- [74] [https://www.atlas.aei.uni-hannover.de/~miriam.cabero/LSC/01/final\\_analysis3\\_c00\\_v1.2.4/](https://www.atlas.aei.uni-hannover.de/~miriam.cabero/LSC/01/final_analysis3_c00_v1.2.4/).
- [75] The LIGO Scientific Collaboration and The Virgo Collaboration, “GW150914: The Advanced LIGO detectors in the era of first discoveries,” *Phys. Rev. Lett.*, vol. 116, p. 131103, 2016.
- [76] A. J. Mullavey, B. J. J. Slagmolen, J. Miller, M. Evans, P. Fritschel, D. Sigg, S. J. Waldman, D. A. Shaddock, and D. E. McClelland, “Arm-length stabilisation for interferometric gravitational-wave detectors using frequency-doubled auxiliary lasers,” *Opt. Express*, vol. 20, no. 1, p. 81, 2012.
- [77] B. P. Abbott *et al.*, “Properties of the Binary Black Hole Merger GW150914,” *Phys. Rev. Lett.*, vol. 116, no. 24, p. 241102, 2016.
- [78] C. L. Mueller, M. A. Arain, G. Ciani, R. T. DeRosa, A. Effler, D. Feldbaum, V. V. Frolov, P. Fulda, J. Gleason, M. Heintze, K. Kawabe, E. J. King, K. Kokeyama, W. Z. Korth, R. M. Martin, A. Mullavey, J. Peold, V. Quetschke, D. H. Reitze, D. B. Tanner, C. Vorvick, L. F. Williams, and G. Mueller, “The Advanced LIGO input optics,” *Rev. Scientific Instruments*, vol. 87, no. 1, p. 014502, 2016.

---

## BIBLIOGRAPHY

- [79] T. T. Fricke, N. D. Smith-Lefebvre, R. Abbott, R. Adhikari, K. L. Dooley, M. Evans, P. Fritschel, V. V. Frolov, K. Kawabe, J. S. Kissel, B. J. J. Slagmolen, and S. J. Waldman, “DC readout experiment in Enhanced LIGO,” *Class. Quant. Grav.*, vol. 29, no. 6, p. 065005, 2012.
- [80] The LIGO Scientific Collaboration, “Calibration of the Advanced LIGO detectors for the discovery of the binary black-hole merger GW150914,” *Phys. Rev. D*, vol. 95, p. 062003, 2017.
- [81] A. Effler, R. M. S. Schofield, V. V. Frolov, G. González, K. Kawabe, J. R. Smith, J. Birch, and R. McCarthy, “Environmental influences on the LIGO gravitational wave detectors during the 6th science run,” *Class. Quant. Grav.*, vol. 32, no. 3, p. 035017, 2015.
- [82] M. Zevin, S. Coughlin, S. Bahaadini, E. Besler, N. Rohani, S. Allen, M. Cabero, K. Crowston, A. K. Katsaggelos, S. L. Larson, T. K. Lee, C. Lintott, T. B. Littenberg, A. Lundgren, C. Østerlund, J. R. Smith, L. Trouille, and V. Kalogera, “Gravity Spy: integrating Advanced LIGO detector characterization, machine learning, and citizen science,” *Class. Quant. Grav.*, vol. 34, no. 6, p. 064003, 2017.
- [83] V. Roma. <https://alog.ligo-wa.caltech.edu/aLOG/index.php?callRep=22980>, 2015.
- [84] P. Schale, R. Schofield, and J. Palamos. <https://alog.ligo-wa.caltech.edu/aLOG/index.php?callRep=28534>, 2016.
- [85] H. Kim, P. King, C. Krämer, P. Kwee, J. Pöld, R. Savage, P. Wessels, and B. Willke, “PSL final design.” LIGO internal technical report T0900649, 2010.
- [86] P. Kwee, C. Bogan, K. Danzmann, M. Frede, H. Kim, P. King, J. Pöld, O. Puncken, R. L. Savage, F. Seifert, P. Wessels, L. Winkelmann, and B. Willke, “Stabilized high-power laser system for the gravitational wave detector Advanced LIGO,” *Opt. Express*, vol. 20, no. 10, pp. 10617–10634, 2012.
- [87] D. Barker. Private communication.
- [88] R. Bork, “Real-time Code Generator (RCG) Runtime Diagnostics (RCG V2.7).” LIGO internal technical report T1100625, 2013.
- [89] J. Veitch, V. Raymond, B. Farr, W. Farr, P. Graff, S. Vitale, B. Aylott, K. Blackburn, N. Christensen, M. Coughlin, W. Del Pozzo, F. Feroz, J. Gair, C.-J. Haster, V. Kalogera, T. Littenberg, I. Mandel, R. O’Shaughnessy, M. Pitkin, C. Rodriguez, C. Röver, T. Sidery, R. Smith, M. Van Der Sluys, A. Vecchio, W. Vousden, and L. Wade, “Parameter estimation for compact binaries with ground-based gravitational-wave observations using the LALInference software library,” *Phys. Rev. D*, vol. 91, p. 042003, 2015.

## BIBLIOGRAPHY

---

- [90] A. Buonanno, B. R. Iyer, E. Ochsner, Y. Pan, and B. S. Sathyaprakash, “Comparison of post-Newtonian templates for compact binary inspiral signals in gravitational-wave detectors,” *Phys. Rev. D*, vol. 80, p. 084043, 2009.
- [91] R. Prix, “Bayesian QNM search on GW150914.” LIGO internal technical report T1500618, 2016.
- [92] The LIGO Scientific Collaboration and The Virgo Collaboration, “Tests of General Relativity with GW150914,” *Phys. Rev. Lett.*, vol. 116, p. 221101, 2016.
- [93] The LIGO Scientific Collaboration and The Virgo Collaboration, “Parameter estimation for compact binary coalescence signals with the first generation gravitational-wave detector network,” *Phys. Rev. D*, vol. 88, p. 062001, 2013.
- [94] L. S. Finn, “Binary inspiral, gravitational radiation, and cosmology,” *Phys. Rev. D*, vol. 53, pp. 2878–2894, 1996.
- [95] B. Farr and W. Farr, “`kombine` github repository.” <https://github.com/bfarr/kombine>.
- [96] D. Foreman-Mackey, D. W. Hogg, D. Lang, and J. Goodman, “`emcee`: The mcmc hammer,” *PASP*, vol. 125, pp. 306–312, 2013.
- [97] E. Berti, V. Cardoso, and M. Casals, “Eigenvalues and eigenfunctions of spin-weighted spheroidal harmonics in four and higher dimensions,” *Phys. Rev. D*, vol. 73, p. 024013, 2006.
- [98] E. Berti, J. Cardoso, V. Cardoso, and M. Cavaglià, “Matched filtering and parameter estimation of ringdown waveforms,” *Phys. Rev. D*, vol. 76, p. 104044, 2007.
- [99] I. Kamaretsos, M. Hannam, S. Husa, and B. S. Sathyaprakash, “Black-hole hair loss: Learning about binary progenitors from ringdown signals,” *Phys. Rev. D*, vol. 85, p. 024018, 2012.
- [100] J. Healy, C. O. Lousto, and Y. Zlochower, “Remnant mass, spin, and recoil from spin aligned black-hole binaries,” *Phys. Rev. D*, vol. 90, no. 10, p. 104004, 2014.
- [101] F. Hofmann, E. Barausse, and L. Rezzolla, “The final spin from binary black holes in quasi-circular orbits,” *Astrophys. J. Lett.*, vol. 825, no. 2, p. L19, 2016.
- [102] X. Jiménez-Forteza, D. Keitel, S. Husa, M. Hannam, S. Khan, and M. Pürrer, “Hierarchical data-driven approach to fitting numerical relativity data for nonprecessing binary black holes with an application to final spin and radiated energy,” *Phys. Rev. D*, vol. 95, no. 6, p. 064024, 2017.
- [103] E. Berti, V. Cardoso, and C. M. Will, “Gravitational-wave spectroscopy of massive black holes with the space interferometer LISA,” *Phys. Rev. D*, vol. 73, p. 064030, 2006.

---

## BIBLIOGRAPHY

- [104] L. London, D. Shoemaker, and J. Healy, “Modeling ringdown: Beyond the fundamental quasinormal modes,” *Phys. Rev. D*, vol. 90, p. 124032, 2014.
- [105] M. Vallisneri, J. Kanner, R. Williams, A. Weinstein, and B. Stephens, “The LIGO Open Science Center,” *J. Phys.: Conf. Series*, vol. 610, no. 1, p. 012021, 2015.
- [106] S. Bhagwat, D. A. Brown, and S. W. Ballmer, “Spectroscopic analysis of stellar mass black-hole mergers in our local universe with ground-based gravitational wave detectors,” *Phys. Rev. D*, vol. 94, no. 8, p. 084024, 2016. [Erratum: *Phys. Rev.D*95,no.6,069906(2017)].
- [107] I. D. Novikov and K. S. Thorne, “Astrophysics of black holes,” in *Black holes (Les astres occlus)* (C. DeWitt and B. S. DeWitt, eds.), Gordon and Breach Science publishers, 1973.
- [108] J. E. McClintock, R. Narayan, S. W. Davis, L. Gou, A. Kulkarni, J. A. Orosz, R. F. Penna, R. A. Remillard, and J. F. Steiner, “Measuring the spins of accreting black holes,” *Class. Quant. Grav.*, vol. 28, p. 114009, 2011.
- [109] L. Blanchet, “Post-Newtonian theory and the two-body problem,” in *Mass and motion in General Relativity* (L. Blanchet, A. Spallicci, and B. Whiting, eds.), vol. 162 of *Fundamental Theories of Physics*, Springer, 2011.
- [110] P. C. Peters and J. Mathews, “Gravitational radiation from point masses in a keplerian orbit,” *Phys. Rev. D*, vol. 131, no. 1, p. 435, 1963.
- [111] F. Pannarale, L. Rezzolla, F. Ohme, and J. S. Read, “Will black hole-neutron star binary inspirals tell us about the neutron star equation of state?,” *Phys. Rev. D*, vol. 84, p. 104017, 2011.
- [112] F. Pannarale, E. Berti, K. Kyutoku, B. D. Lackey, and M. Shibata, “Gravitational-wave cutoff frequencies of tidally disruptive neutron star-black hole binary mergers,” *Phys. Rev. D*, vol. 92, p. 081504, 2015.
- [113] D. Eichler, M. Livio, T. Piran, and D. N. Schramm, “Nucleosynthesis, neutrino bursts and Gamma-rays from coalescing neutron stars,” *Nature*, vol. 340, pp. 126–128, 1989.
- [114] L. Blanchet, “Innermost circular orbit of binary black holes at the third post-Newtonian approximation,” *Phys. Rev. D*, vol. 65, p. 124009, 2002.
- [115] A. Buonanno, Y. Chen, and M. Vallisneri, “Detection template families for gravitational waves from the final stages of binary–black-hole inspirals: nonspinning case,” *Phys. Rev. D*, vol. 67, p. 024016, 2003.
- [116] E. Barausse, A. Buonanno, and A. Le Tiec, “Complete nonspinnning effective-one-body metric at linear order in the mass ratio,” *Phys. Rev. D*, vol. 85, p. 064010, 2012.

## BIBLIOGRAPHY

---

- [117] L. Blanchet and B. R. Iyer, “Third post-Newtonian dynamics of compact binaries: equations of motion in the center-of-mass frame,” *Class. Quant. Grav.*, vol. 20, no. 4, p. 755, 2003.
- [118] M. Favata, “Conservative corrections to the innermost stable circular orbit (ISCO) of a Kerr black hole: A new gauge-invariant post-Newtonian ISCO condition, and the ISCO shift due to test-particle spin and the gravitational self-force,” *Phys. Rev. D*, vol. 83, no. 2, p. 024028, 2011.
- [119] A. Ghosh, A. Ghosh, N. K. Johnson-McDaniel, C. K. Mishra, P. Ajith, W. Del Pozzo, D. A. Nichols, Y. Chen, A. B. Nielsen, C. P. L. Berry, and L. London, “Testing general relativity using golden black-hole binaries,” *Phys. Rev. D*, vol. 94, p. 021101, 2016.
- [120] S. W. Hawking, “Gravitational radiation from colliding black holes,” *Phys. Rev. Lett.*, vol. 26, pp. 1344–1346, 1971.
- [121] S. A. Hughes and K. Menou, “Golden binaries for LISA: Robust probes of strong-field gravity,” *Astrophys. J.*, vol. 623, pp. 689–699, 2005.
- [122] M. Cabero, C. D. Capano, O. Fischer-Birnholtz, B. Krishnan, A. B. Nielsen, A. H. Nitz, and C. M. Biwer, “Observational tests of the black hole area increase law,” *Phys. Rev. D (submitted)*, *arXiv:1711.09073*, 2017.
- [123] T. Dal Canton, A. H. Nitz, A. P. Lundgren, A. B. Nielsen, D. A. Brown, T. Dent, I. W. Harry, B. Krishnan, A. J. Miller, K. Wette, K. Wiesner, and J. L. Willis, “Implementing a search for aligned-spin neutron star-black hole systems with advanced ground based gravitational wave detectors,” *Phys. Rev. D*, vol. 90, p. 082004, 2014.
- [124] A. H. Nitz, A. Lundgren, D. A. Brown, E. Ochsner, D. Keppel, and I. W. Harry, “Accuracy of gravitational waveform models for observing neutron-star–black-hole binaries in advanced ligo,” *Phys. Rev. D*, vol. 88, p. 124039, 2013.
- [125] L. E. Kidder, C. M. Will, and A. G. Wiseman, “Coalescing binary systems of compact objects to (post) $^{5/2}$ -Newtonian order. III. Transition from inspiral to plunge,” *Phys. Rev. D*, vol. 47, no. 8, p. 3281, 1993.
- [126] A. Taracchini. Private communication.
- [127] J. Vines, É. É. Flanagan, and T. Hinderer, “Post-1-Newtonian tidal effects in the gravitational waveform from binary inspirals,” *Phys. Rev. D*, vol. 83, no. 8, p. 084051, 2011.
- [128] L. Wade, J. D. E. Creighton, E. Ochsner, B. D. Lackey, B. F. Farr, T. B. Littenberg, and V. Raymond, “Systematic and statistical errors in a bayesian approach to the estimation of the neutron-star equation of state using advanced gravitational wave detectors,” *Phys. Rev. D*, vol. 89, no. 10, p. 103012, 2014.

---

## BIBLIOGRAPHY

- [129] M. Cabero, A. B. Nielsen, A. P. Lundgren, and C. D. Capano, “Minimum energy and the end of the inspiral in the post-Newtonian approximation,” *Phys. Rev. D*, vol. 95, no. 6, p. 064016, 2017.
- [130] D. Bini and T. Damour, “Analytical determination of the two-body gravitational interaction potential at the fourth post-Newtonian approximation,” *Phys. Rev. D*, vol. 87, p. 121501, 2013.
- [131] B. Mikóczi, M. Vasúth, and L. Á. Gergely, “Self-interaction spin effects in inspiralling compact binaries,” *Phys. Rev. D*, vol. 71, no. 12, p. 124043, 2005.
- [132] A. Bohé, G. Faye, S. Marsat, and E. K. Porter, “Quadratic-in-spin effects in the orbital dynamics and gravitational-wave energy flux of compact binaries at the 3PN order,” *Class. Quant. Grav.*, vol. 32, p. 195010, 2015.
- [133] M. Levi and J. Steinhoff, “Equivalence of ADM Hamiltonian and Effective Field Theory approaches at next-to-next-to-leading order spin1-spin2 coupling of binary inspirals,” *J. Cosmol. and Astropart. Phys.*, vol. 1412, no. 12, p. 003, 2014.
- [134] M. Levi and J. Steinhoff, “Complete conservative dynamics for inspiralling compact binaries with spins at fourth post-Newtonian order,” *arXiv:1607.04252*, 2016.
- [135] A. Bohé, S. Marsat, and L. Blanchet, “Next-to-next-to-leading order spin-orbit effects in the gravitational wave flux and orbital phasing of compact binaries,” *Class. Quant. Grav.*, vol. 30, no. 13, p. 135009, 2013.
- [136] M. Levi and J. Steinhoff, “Next-to-next-to-leading order gravitational spin-orbit coupling via the effective field theory for spinning objects in the post-Newtonian scheme,” *J. Cosmol. and Astropart. Phys.*, vol. 1601, no. 01, p. 011, 2016.
- [137] S. Marsat, “Cubic-order spin effects in the dynamics and gravitational wave energy flux of compact object binaries,” *Class. Quant. Grav.*, vol. 32, p. 085008, 2015.
- [138] E. Poisson, A. Pound, and I. Vega, “The motion of point particles in curved spacetime,” *Living Rev. Relativity*, vol. 14, no. 7, 2011.
- [139] L. Barack and N. Sago, “Gravitational self-force correction to the Innermost Stable Circular Orbit of a Schwarzschild black hole,” *Phys. Rev. Lett.*, vol. 102, p. 191101, 2009.
- [140] S. Isoyama, L. Barack, S. R. Dolan, A. Le Tiec, H. Nakano, A. G. Shah, T. Tanaka, and N. Warburton, “Gravitational self-force correction to the Innermost Stable Circular equatorial Orbit of a Kerr black hole,” *Phys. Rev. Lett.*, vol. 113, p. 161101, 2014.
- [141] “LSC Algorithm Library Suite.” <https://wiki.ligo.org/DASWG/LALSuite>.

## BIBLIOGRAPHY

---

- [142] P. Ajith, M. Hannam, S. Husa, Y. Chen, B. Brügmann, N. Dorband, D. Müller, F. Ohme, D. Pollney, C. Reisswig, L. Santamaría, and J. Seiler, “Inspiral-merger-ringdown waveforms for black-hole binaries with nonprecessing spins,” *Phys. Rev. Lett.*, vol. 106, p. 241101, 2011.
- [143] L. Santamaría, F. Ohme, P. Ajith, B. Brügmann, N. Dorband, M. Hannam, S. Husa, P. Mösta, D. Pollney, C. Reisswig, E. L. Robinson, J. Seiler, and B. Krishnan, “Matching post-Newtonian and numerical relativity waveforms: systematic errors and a new phenomenological model for nonprecessing black hole binaries,” *Phys. Rev. D*, vol. 82, p. 064016, 2010.
- [144] T. Damour, “Coalescence of two spinning black holes: an effective one-body approach,” *Phys. Rev. D*, vol. 64, p. 124013, 2001.
- [145] C. Cutler and É. É. Flanagan, “Gravitational waves from merging compact binaries: How accurately can one extract the binary’s parameters from the inspiral waveform?,” *Phys. Rev. D*, vol. 49, no. 6, p. 2658, 1994.
- [146] E. Poisson and C. M. Will, “Gravitational waves from inspiraling compact binaries: Parameter estimation using second-post-Newtonian waveforms,” *Phys. Rev. D*, vol. 52, no. 2, p. 848, 1995.
- [147] L. Barsotti and P. Fritschel, “Early aLIGO configurations: example scenarios toward design sensitivity.” LIGO public technical report T1200307, 2012.
- [148] A. Buonanno, Y. Chen, and M. Vallisneri, “Detecting gravitational waves from precessing binaries of spinning compact objects: adiabatic limit,” *Phys. Rev. D*, vol. 67, p. 104025, 2003.
- [149] J. Steinhoff and D. Puetzfeld, “Influence of internal structure on the motion of test bodies in extreme mass ratio situations,” *Phys. Rev. D*, vol. 86, p. 044033, 2012.
- [150] A. Le Tiec, E. Barausse, and A. Buonanno, “Gravitational self-force correction to the binding energy of compact binary systems,” *Phys. Rev. Lett.*, vol. 108, p. 131103, 2012.
- [151] J. M. Lattimer and D. N. Schramm, “The tidal disruption of neutron stars by black holes in close binaries,” *Astrophys. J.*, vol. 210, p. 549, 1976.
- [152] M. Vallisneri, “Prospects for gravitational-wave observations of neutron-star tidal disruption in neutron-star–black-hole binaries,” *Phys. Rev. Lett.*, vol. 84, no. 16, p. 3519, 2000.
- [153] E. Nakar, “Short-hard Gamma-ray bursts,” *Physics Reports*, vol. 442, p. 166, 2007.
- [154] T. Damour and O. M. Lecian, “Gravitational polarizability of black holes,” *Phys. Rev. D*, vol. 80, p. 044017, 2009.

---

## BIBLIOGRAPHY

- [155] M. Cabero and B. Krishnan, “Tidal deformations of spinning black holes in Bowen-York initial data,” *Class. Quant. Grav.*, vol. 32, p. 045009, 2015.
- [156] E. Poisson, “Tidal deformation of a slowly rotating black hole,” *Phys. Rev. D*, vol. 91, p. 044004, 2015.
- [157] T. Hinderer, “Tidal love numbers of neutron stars,” *Astrophys. J.*, vol. 677, p. 1216, 2008.
- [158] T. Damour and A. Nagar, “Relativistic tidal properties of neutron stars,” *Phys. Rev. D*, vol. 80, no. 8, p. 084035, 2009.
- [159] M. Shibata, K. Kyutoku, T. Yamamoto, and K. Taniguchi, “Gravitational waves from black hole-neutron star binaries: classification of waveforms,” *Phys. Rev. D*, vol. 79, p. 044030, 2009.
- [160] K. Kyutoku, H. Okawa, M. Shibata, and K. Taniguchi, “Gravitational waves from spinning black hole-neutron star binaries: dependence on black hole spins and on neutron star equations of state,” *Phys. Rev. D*, vol. 84, no. 6, p. 064018, 2011.
- [161] S. W. Hawking, “Black holes in general relativity,” *Commun. Math. Phys.*, vol. 25, no. 2, pp. 152–166, 1972.
- [162] J. D. Bekenstein, “Black holes and the second law,” *Lett. Nuovo Cim. (1971–1985)*, vol. 4, no. 15, p. 737, 1972.
- [163] J. M. Bardeen, B. Carter, and S. W. Hawking, “The Four laws of black hole mechanics,” *Commun. Math. Phys.*, vol. 31, pp. 161–170, 1973.
- [164] J. D. Bekenstein, “Black holes and entropy,” *Phys. Rev. D*, vol. 7, pp. 2333–2346, 1973.
- [165] A. Ghosh, A. Ghosh, N. K. Johnson-McDaniel, C. K. Mishra, P. Ajith, W. Del Pozzo, D. A. Nichols, Y. Chen, A. B. Nielsen, C. P. L. Berry, and L. London, “Testing general relativity using golden black-hole binaries,” *Phys. Rev. D*, vol. 94, no. 2, p. 021101, 2016.
- [166] A. Ghosh, N. K. Johnson-McDaniel, A. Ghosh, C. K. Mishra, P. Ajith, W. Del Pozzo, C. P. Berry, A. B. Nielsen, and L. London, “Testing general relativity using gravitational wave signals from the inspiral, merger and ringdown of binary black holes,” *Class. Quant. Grav.*, vol. 35, no. 1, p. 014002, 2017.
- [167] P. T. Chrusciel, E. Delay, G. J. Galloway, and R. Howard, “The Area theorem,” *Annales Henri Poincare*, vol. 2, pp. 109–178, 2001.
- [168] P. T. Chrusciel and G. J. Galloway, ““Nowhere” differentiable horizons,” *Commun. Math. Phys.*, vol. 193, pp. 449–470, 1998.

## BIBLIOGRAPHY

---

- [169] J. Thornburg, “Event and apparent horizon finders for 3+1 numerical relativity,” *Living Rev. Rel.*, vol. 10, p. 3, 2007.
- [170] A. Ashtekar and B. Krishnan, “Isolated and dynamical horizons and their applications,” *Living Rev. Rel.*, vol. 7, p. 10, 2004.
- [171] I. Booth, “Black hole boundaries,” *Can. J. Phys.*, vol. 83, pp. 1073–1099, 2005.
- [172] E. Gourgoulhon and J. L. Jaramillo, “New theoretical approaches to black holes,” *New Astron. Rev.*, vol. 51, pp. 791–798, 2008.
- [173] A. Ashtekar and B. Krishnan, “Dynamical horizons and their properties,” *Phys. Rev. D*, vol. 68, p. 104030, 2003.
- [174] C. Barceló and M. Visser, “Twilight for the energy conditions?,” *Int. J. Mod. Phys.*, vol. D11, pp. 1553–1560, 2002.
- [175] E. Berti, V. Cardoso, and A. O. Starinets, “Quasinormal modes of black holes and black branes,” *Class. Quant. Grav.*, vol. 26, p. 163001, 2009.
- [176] S. Gossan, J. Veitch, and B. S. Sathyaprakash, “Bayesian model selection for testing the no-hair theorem with black hole ringdowns,” *Phys. Rev. D*, vol. 85, p. 124056, 2012.
- [177] N. Yunes, K. Yagi, and F. Pretorius, “Theoretical physics implications of the binary black-hole mergers GW150914 and GW151226,” *Phys. Rev. D*, vol. 94, no. 8, p. 084002, 2016.
- [178] V. Baibhav, E. Berti, V. Cardoso, and G. Khanna, “Black hole spectroscopy: Systematic errors and ringdown energy estimates,” *Phys. Rev. D*, vol. 97, p. 044048, 2018.
- [179] L. Smarr, A. Cadez, B. S. DeWitt, and K. Eppley, “Collision of Two Black Holes: Theoretical Framework,” *Phys. Rev. D*, vol. 14, pp. 2443–2452, 1976.
- [180] J. Healy, I. Ruchlin, C. O. Lousto, and Y. Zlochower, “High Energy Collisions of Black Holes Numerically Revisited,” *Phys. Rev. D*, vol. 94, no. 10, p. 104020, 2016.
- [181] W. Anderson, P. Brady, D. Chin, J. Creighton, K. Riles, and J. Whelan, “Beam pattern response functions and times of arrival for earthbound interferometer.” <https://dcc.ligo.org/public/0012/T010110/001/T010110.pdf>, 2009.
- [182] I. Mandel, C. P. L. Berry, F. Ohme, S. Fairhurst, and W. M. Farr, “Parameter estimation on compact binary coalescences with abruptly terminating gravitational waveforms,” *Class. Quant. Grav.*, vol. 31, p. 155005, 2014.
- [183] “SXS gravitational waveform database.” <http://www.black-holes.org/waveforms>.

---

## BIBLIOGRAPHY

- [184] A. H. Mroue, M. Scheel, B. Szilagyi, H. Pfeiffer, M. Boyle, D. Hemberger, L. Kidder, G. Lovelace, S. Ossokine, N. Taylor, A. Zenginoglu, L. Buchman, T. Chu, E. Foley, M. Giesler, R. Owen, and S. Teukolsky, “Catalog of 174 Binary Black Hole Simulations for Gravitational Wave Astronomy,” *Phys. Rev. Lett.*, vol. 111, no. 24, p. 241104, 2013.
- [185] D. Shoemaker, “Advanced LIGO anticipated sensitivity curves.” LIGO internal technical report T0900288, 2009.
- [186] J. Veitch, V. Raymond, B. Farr, W. Farr, P. Graff, S. Vitale, B. Aylott, K. Blackburn, N. Christensen, M. Coughlin, W. DelPozzo, F. Feroz, J. Gair, C. Haster, V. Kalogera, T. Littenberg, I. Mandel, R. OShaughnessy, M. Pitkin, C. Rodriguez, C. Rover, T. Sidery, R. Smith, M. VanDerSluys, A. Vecchio, W. Vousden, and L. Wade, “Parameter estimation for compact binaries with ground-based gravitational-wave observations using the LALInference software library,” *Phys. Rev. D*, vol. 91, no. 4, p. 042003, 2015.
- [187] S. Husa, S. Khan, M. Hannam, M. Pürrer, F. Ohme, X. Jiménez-Forteza, and A. Bohé, “Frequency-domain gravitational waves from nonprecessing black-hole binaries. I. New numerical waveforms and anatomy of the signal,” *Phys. Rev. D*, vol. 93, p. 044006, 2016.
- [188] S. Klimenko, G. Vedovato, M. Drago, F. Salemi, V. Tiwari, G. Prodi, C. Lazzaro, K. Ackley, S. Tiwari, C. DaSilva, and G. Mitselmakher, “Method for detection and reconstruction of gravitational wave transients with networks of advanced detectors,” *Phys. Rev. D*, vol. 93, no. 4, p. 042004, 2016.
- [189] A. Buonanno, B. R. Iyer, E. Ochsner, Y. Pan, and B. S. Sathyaprakash, “Comparison of post-Newtonian templates for compact binary inspiral signals in gravitational-wave detectors,” *Phys. Rev. D*, vol. 80, p. 084043, 2009.
- [190] F. F. Kuo and J. F. Kaiser, *System analysis by digital computer*. Wiley, 1966.
- [191] J. A. Thomas and T. M. Cover, *Elements of Information Theory*. Wiley-Interscience, 1991.
- [192] D. M. Endres and J. E. Schindelin, “A new metric for probability distributions,” *IEEE Transactions on Information Theory*, vol. 49, no. 7, pp. 1858–1860, 2003.
- [193] E. Thrane, P. D. Lasky, and Y. Levin, “Challenges testing the no-hair theorem with gravitational waves,” *Phys. Rev. D*, vol. 96, no. 10, p. 102004, 2017.
- [194] S. Bhagwat, M. Okounkova, S. W. Ballmer, D. A. Brown, M. Giesler, M. A. Scheel, and S. A. Teukolsky, “On choosing the start time of binary black hole ringdown,” *arXiv:1711.00926*, 2017.
- [195] F. Robinet, “Omicron: An algorithm to detect and characterize transient noise in gravitational-wave detectors.” <https://tds.ego-gw.it/ql/?c=10651>, 2015.

## BIBLIOGRAPHY

---

- [196] J. R. Smith, T. Abbott, E. Hirose, N. Leroy, D. MacLeod, J. McIver, P. Saulson, and P. Shawhan, “A hierarchical method for vetoing noise transients in gravitational-wave detectors,” *Class. Quant. Grav.*, vol. 28, no. 23, p. 235005, 2011.
- [197] S. Chatterji, L. Blackburn, G. Martin, and E. Katsavounidis, “Multiresolution techniques for the detection of gravitational-wave bursts,” *Class. Quant. Grav.*, vol. 21, no. 20, p. S1809, 2004.
- [198] S. K. Chatterji, *The search for gravitational wave bursts in data from the second LIGO science run*. PhD thesis, Massachusetts Institute of Technology, 2005.
- [199] J. S. Areeda, J. R. Smith, A. P. Lundgren, E. Maros, D. M. Macleod, and J. Zweizig, “LigoDV-web: Providing easy, secure and universal access to a large distributed scientific data store for the LIGO Scientific Collaboration,” *Astron. Comput.*, vol. 18, pp. 27–34, 2017.
- [200] The LIGO Scientific Collaboration and The Virgo Collaboration. [https://losc.ligo.org/detector\\_status/](https://losc.ligo.org/detector_status/).
- [201] E. Poisson, “Gravitational waves from inspiraling compact binaries: the quadrupole-moment term,” *Phys. Rev. D*, vol. 57, no. 8, p. 5287, 1998.



# Acknowledgements

The pleasure of travelling comes not only from living new experiences and visiting new places, but also from the new interesting people one gets to meet on the journey. I feel now like I have been following a long path during the last years, and I have conversed with many persons on the side of the road. To a greater or lesser extent, all of them contributed to my development as a scientist, and each word written in this thesis contains a part of them.

First of all I would like to thank Prof. Dr. Bruce Allen for giving me the opportunity to join this excellent research group at the Max Planck Institute, and most especially my advisor Dr. Badri Krishnan for his career advice and for helping me push my research forward. And not to forget my referees Prof. Dr. Bernd Brügmann, Prof. Dr. Duncan Brown, and Assoc. Prof. Dr. Joshua Smith: thank you for reviewing my work, I hope you enjoyed the reading.

Many people granted me part of their time to read through chapters of my thesis, and I owe to them the final result presented here. I am thankful to Evan Goetz and Alex Nielsen for the introduction; to Tito Dal Canton, Tom Dent, Evan Goetz, Alex Nitz, and Josh Willis for the chapter about the PyCBC searches; to Evan Goetz, Andrew Lundgren and Laura Nuttal for the chapter about blip glitches; and to Collin Capano, Badri Krishnan, and Frank Ohme for the chapter about the parameter estimation of the ringdown signature. I would also like to thank the co-authors of the scientific papers that turned into the last two chapters: Collin Capano, Ofek Fischer-Birnholtz, Badri Krishnan, Andrew Lundgren, Alex Nielsen, and Alex Nitz. And another special thanks to Frank Ohme for reviewing the German translation of my abstract.

I would like to thank the members of the CBC group here at the Albert Einstein Institute, for scientific debates and discussions that let me progress further; the members of the PyCBC group, for their guidance on the usage of PyCBC and for all what I have learned from them; the members of the Detector Characterisation group, for interesting discussions and for showing me how to use GWpy, HVeto, etc.; and the team at the LIGO Hanford site, for welcoming me on my visits and helping me hunt blip glitches. Carsten Aulbert, Henning Fehrmann, and Alex Post also deserve my gratitude for their help and guidance with the Atlas cluster: most of this work would not have been possible without their infinite support.

Finally, I am thankful to my parents and sister for encouraging me to go to University and supporting me through the good and bad times. To my friends, who shared experiences with me over the last years and made Hannover a little less grey. And especially to Evan, for always listening to my concerns and for always being there when I needed.



## CURRICULUM VITAE

# Miriam Anabel Cabero Müller

### PERSONAL DATA

---

DATE OF BIRTH: 4 March 1988

CITIZENSHIP: Spanish and German

### EDUCATION

---

2018 Doctor of Science – Dr. rer. nat. –

**Gottfried Wilhelm Leibniz University of Hannover & Max Planck Institute for Gravitational Physics**, Germany

Thesis: “Gravitational-wave astronomy with compact binary coalescences: from blip glitches to the black hole area increase law”

Thesis advisory committee: Dr. Badri Krishnan, Prof. Dr. Bruce Allen and Prof. Dr. Bernd Brügmann

2014 Master of Science

**Gottfried Wilhelm Leibniz University of Hannover**, Germany

Thesis: “Tidal deformation of spinning black holes”

Advisors: Dr. Badri Krishnan and Prof. Domenico Giulini

2012 Degree (Licenciatura) in Physics

**University of Salamanca**, Spain

Erasmus program at the Gottfried Wilhelm Leibniz University of Hannover, academic year 2011-12

### RESEARCH EXPERIENCE

---

MARCH 2018 - PRESENT Postdoctoral scholar, MAX PLANCK INSTITUTE FOR GRAVITATIONAL PHYSICS, Hannover, Germany

- Tests of the black hole area increase law and no-hair theorem with gravitational waves

SEPT. 2014 - FEB 2018 Doctor's Thesis Research, MAX PLANCK INSTITUTE FOR GRAVITATIONAL PHYSICS, Hannover, Germany  
Supervised by Dr. Badri Krishnan

- Data analysis for the second generation of gravitational-wave observatories to find astrophysical events
- Develop methods to analyse the ringdown of the remnant black hole as it settles down to its final equilibrium state
- Test aspects of black holes in General Relativity from analysing different phases of black hole coalescences

- Detector characterisation to improve the sensitivity of compact binary coalescence searches
- Grading homework assignments of Master students for Gravitational Wave Physics and supervising seminars

APR. 2013 - MAY 2014    Master's Thesis Research, MAX PLANCK INSTITUTE FOR GRAVITATIONAL PHYSICS, Hannover, Germany  
Supervised by Dr. Badri Krishnan

- Calculation of conformal factors and location of apparent horizons using the Bowen-York initial data
- Computation of the source multipoles for different systems of spinning black holes
- Determining the tidal coefficients for a spinning black hole with a binary companion.

APR. 2012 - JAN. 2014    Student Research assistant, INSTITUTE OF QUANTUM OPTICS, Hannover, Germany  
Research group of Prof. Dr. Christian Ospelkaus

- Characterization of a Schwarzschild objective and a camera system for imaging of single trapped atomic ions
- Redesign of mechanical components using the Autodesk Inventor 3D CAD program
- Assistance in interferometric alignment and bonding of optical components
- Design of imaging systems using the Radiant Zemax program
- Grading homework assignments of undergraduate students for Atomic and Molecular Physics.

---

## CONFERENCES AND SEMINARS

### Invited talks

5 - 9 JUN. 2017	<b>Generation GW: Diving into Gravitational Waves</b> , “Compact binary coalescences (CBC) with Advanced LIGO,” University of the Virgin Islands, St. Thomas (USA)
10 - 12 Nov. 2016	<b>Bundesweite WE-Heraeus-Lehrerfortbildung zur Astronomie</b> , “Gravitationswellen und astronomische Forschung,” Haus der Astronomie Heidelberg (Germany)

### Contributed talks and posters

30 MAY - 2 JUN. 2017	<b>Gravitational Wave Physics and Astronomy Workshop</b> , Annecy (France), talk “Testing the area theorem with gravitational-wave signals”
----------------------	---

10 - 15 JUL. 2016	<b>21st International Conference on General Relativity and Gravitation</b> , Columbia University (United States), talk “Prospects for observing multiple ringdown modes in a binary black hole merger”
15 - 18 JUN. 2016	<b>Gravitational Wave Physics and Astronomy Workshop</b> , Massachusetts Institute of Technology (United States)
23 - 26 MAY 2016	<b>The first observation of a binary black hole merger: Status and future prospects</b> , Max Planck Institute for Gravitational Physics, Hannover (Germany)
30 Nov. - 2 DEC. 2015	<b>A century of General Relativity</b> , Max Planck Institute for Gravitational Physics, Berlin (Germany)
28 - 29 Nov. 2015	<b>Einstein's Legacy</b> , University of London (United Kingdom)
22 - 26 JUN. 2015	<b>11th Edoardo Amaldi conference on Gravitational Waves</b> , Gwangju (South Korea), talk “The end of the inspiral in the post-Newtonian approximation”
17 - 20 JUN. 2015	<b>Gravitational Wave Physics and Astronomy Workshop</b> , Osaka City University (Japan), poster “Where does the inspiral end?”

## AWARDS AND HONORS

---

2017	<b>Princess of Asturias Award for Technical and Scientific Research</b> , awarded to Rainer Weiss, Kip S. Thorne, Barry C. Barish, and the LIGO Scientific Collaboration
2017	<b>Bruno Rossi Prize</b> , awarded to Professor Gabriela Gonzalez and the LIGO Scientific Collaboration
2017	<b>Royal Astronomical Society</b> , Group Achievement Award in Astronomy, awarded to the LIGO team
2016	<b>Certificate of Recognition</b> , LSC poster prize for the poster “Black hole ringdown parameter estimation,” LIGO Scientific Collaboration
2016	<b>Gruber Cosmology Prize</b> , awarded to Ronald W. P. Drever, Kip S. Thorne, Rainer Weiss, and the LIGO Discovery Team
2016	<b>Special Breakthrough Prize in Fundamental Physics</b> , awarded to Ronald W. P. Drever, Kip S. Thorne, Rainer Weiss and the LIGO Scientific Collaboration
2011-12	<b>Erasmus (European Region Action Scheme for the Mobility of University Students) Fellowship</b>
2011-12	<b>Fellowship for University studies</b> , Spanish Ministry of Education and Science
2010-11	<b>Fellowship for University studies</b> , Spanish Ministry of Education and Science
2006-07	<b>Fellowship for University studies</b> , Spanish Ministry of Education and Science

## PUBLIC OUTREACH

---

APRIL 2018	<b>Zukunftstag im Albert Einstein Institut Hannover</b> , Building spectrometers and speed informing with school children
APRIL 2018	<b>Celebration of science, Richland (WA)</b> , Booth about LIGO Hanford and gravitational-wave astronomy
MAY 2017	<b>Familiennachmittag im Historischen Museum Hannover</b> , Exhibition about gravitational-waves research
APRIL 2017	<b>Zukunftstag im Albert Einstein Institut Hannover</b> , Building spectrometers and speed informing with school children

SUMMER 2016 **Bulletin of the Spanish Astronomical Society (SEA)**, article  
about the first detection of gravitational waves (in Spanish), issue 34

# SELECTED PUBLICATIONS

## **Observational tests of the black hole area increase law**

M. Cabero, C. D. Capano, O. Birnholtz, B. Krishnan, A. B. Nielsen, A. H. Nitz and C. M. Biwer  
Phys. Rev. D (*submitted*), arXiv:1711.09073, (2017)

## **The end of the inspiral in the post-Newtonian approximation**

M. Cabero, A. B. Nielsen, A. P. Lundgren and C. D. Capano  
Phys. Rev. D 95, 064016, (2017)

## **Tidal deformations of spinning black holes in Bowen-York initial data**

M. Cabero, B. Krishnan  
Class. Quant. Grav. 32, 045009, (2015)

## **Low significance of evidence for black hole echoes in gravitational wave data**

J. Westerweck et al.  
Phys. Rev. D (*accepted*), arXiv:1712.09966, (2017)

## **Gravity Spy: integrating advanced LIGO detector characterization, machine learning, and citizen science**

M. Zevin et al.  
Class. Quant. Gravity 34, 064003, (2017)

## **Comments on: "Echoes from the abyss: Evidence for Planck-scale structure at black hole horizons"**

G. Ashton et al.  
arXiv:1612.05625, (2016)

## **The PyCBC search for gravitational waves from compact binary coalescence**

S. Usman et al.  
Class. Quant. Gravity 33, 215004, (2016)

## **GW170817: Observation of gravitational waves from a binary neutron star inspiral**

The LIGO Scientific Collaboration and the Virgo Collaboration  
Phys. Rev. Lett. 119, 161101, (2017)

## **GW170814: A Three-Detector Observation of Gravitational Waves from a Binary Black Hole Coalescence**

The LIGO Scientific Collaboration and the Virgo Collaboration  
Phys. Rev. Lett. 119, 141101, (2017)

## **Binary black hole mergers in the first Advanced LIGO observing run**

The LIGO Scientific Collaboration and the Virgo Collaboration  
Phys. Rev. X 6, 041015, (2016)

## **GW150914: First results from the search for binary black hole coalescence with Advanced LIGO**

The LIGO Scientific Collaboration and the Virgo Collaboration  
Phys. Rev. D 93, 122003, (2016)

## **Observation of gravitational waves from a binary black hole merger**

The LIGO Scientific Collaboration and the Virgo Collaboration  
Phys. Rev. Lett. 116, 061102, (2016)